SYNTHESIS AND CHARACTERIZATION OF TANTALUM AND DIAMOND-LIKE CARBON THIN FILMS ON CoCrMo ALLOY SHEETS

A Thesis Submitted to the College of

Graduate and Postdoctoral Studies

In Partial Fulfillment of the Requirements

For the Degree of Doctor of Philosophy

In the Department of Mechanical Engineering

University of Saskatchewan

Saskatoon

By

SHEIDA SHIRI

PERMISSION TO USE

In presenting this thesis in partial fulfillment of the requirements for a Postgraduate degree from the University of Saskatchewan, I agree that the Libraries of this University may make it freely available for inspection. I further agree that permission for copying of this thesis in any manner, in whole or in part, for scholarly purposes may be granted by Professor Qiaoqin Yang and Professor Akindele Odeshi who supervised my thesis work or, in their absence, by the Head of the Department or the Dean of the College in which my thesis work was done. It is understood that any copying or publication or use of this thesis or parts thereof for financial gain shall not be allowed without my written permission. It is also understood that due recognition shall be given to me and to the University of Saskatchewan in any scholarly use which may be made of any material in my thesis.

Requests for permission to copy or to make other uses of materials in this thesis/dissertation in whole or part should be addressed to:

Head of the Department of Mechanical Engineering

University of Saskatchewan

57 Campus Drive

Saskatoon, Saskatchewan S7N 5A9

Canada

OR

Dean

College of Graduate and Postdoctoral Studies

University of Saskatchewan

116 Thorvaldson Building, 110 Science Place

Saskatoon, Saskatchewan S7N 5C9

Canada

ABSTRACT

In the present research study, Tantalum (Ta) and Diamond-like Carbon (DLC) thin films were deposited on a biomedical Cobalt-Chromium-Molybdenum alloy (CoCrMo alloy) and investigated to improve the surface functionality of this alloy as femoral heads for artificial hip joints.

Ta thin films were deposited on the CoCrMo alloy sheets by magnetron sputtering and the effect of deposition parameters on the formation of different phases of Ta was studied using X-ray Diffraction (XRD), Scanning Electron Microscopy (SEM), X-ray Photoelectron Spectroscopy (XPS), and X-ray Absorption Spectroscopy (XAS). By choosing appropriate processing conditions, adherent α- and β-Ta thin films were developed on the CoCrMo alloy sheets and their adhesion, mechanical, and surface properties were characterized using Rockwell C indentation, nanoindentation, optical profilometry, and a contact angle goniometer. The tribological and corrosion behavior of the Ta coated and uncoated CoCrMo alloy sheets were studied using a ball-on-disk tribo tester and a potentiostat. The results demonstrate that adherent Ta thin films (α-Ta or β-Ta) can be applied to improve corrosion and wear behavior of the CoCrMo alloy, and possibly the performance of the alloy in orthopedic implant applications. Specifically, fcc Ta thin film formation, its structure and stability were investigated and its XRD pattern was obtained and reported for the first time.

DLC thin films were deposited on the CoCrMo alloy sheets using Ta interlayers by ion beam deposition and characterized using Raman spectroscopy, XPS, and SEM. Severe delamination of DLC coatings was observed on the samples. The results show that the delamination is not just related to the energy level of ion bombardment, which induces intrinsic stress into the film during DLC deposition, but also related to the interfacial layer formation between Ta and DLC films. Furthermore, a simple nondestructive method was evaluated for DLC stress measurement. For this purpose, DLC thin films on Si wafers with different shapes and sizes were synthesized and the internal stress of the thin films were measured with the aid of Zygo optical profiler using the Stoney equation. The results show that this simple method is appropriate and reliable for DLC stress determination.

ACKNOWLEDGMENTS

DEDICATION

To my beloved parents

SHAHIN and SHAHLA

And my dear sister

SHABNAM

TABLE OF CONTENTS

LIST OF TABLES

LIST OF FIGURES

LIST OF ABBREVIATIONS

a-C	amorphous carbon
a-C: H	hydrogenated amorphous carbon
Al	Aluminum
Ar	Argon
bcc	body-centered cubic
BSE	Backscattered Electrons
CETR	Center for Tribology
CFI	Canada Foundation for Innovation
CH_4	Methane
CLS	Canadian Light Source
Co	Cobalt
CoC	Ceramic on Ceramic
CoCrMo alloy	Cobalt-Chromium-Molybdenum alloy
COF	Coefficient of Friction
CoM	Ceramic on Metal
CoP	Ceramic on Polyethylene
Cr	Chromium
CSI	Coherence Scanning Interferometry
CVD	Chemical Vapor Deposition
DC	Direct Current
DLC	Diamond-like Carbon
EHI	End Hall Ion
fcc	face-centered cubic
GLC	Graphite-like Carbon
GOS	Government of Saskatchewan
hcp	hexagonal close-packed
HXMA	Hard X-ray MicroAnalysis
IBD	Ion Beam Deposition
MoC	Metal on Ceramic

MoM	Metal on Metal
MoP	Metal on Polyethylene
Nb	Niobium
NSERC	Natural Sciences and Engineering Research Council of Canada
pbs	Phosphate-Buffered Saline
PVD	Physical Vapor Deposition
RF	Radio Frequency
SD	Standard Deviation
SE	Secondary Electrons
SEM	Scanning Electron Microscopy
SSSC	Saskatchewan Structural Sciences Centre
Ta	Tantalum
ta-C	tetrahedral amorphous carbon
ta-C: H	hydrogenated tetrahedral amorphous carbon
TEM	Transmission Electron Microscopy
TEY	Total Electron Yield
TFY	Total Fluorescence Yield
Ti	Titanium
TiN	Titanium Nitride
U of S	University of Saskatchewan
UHMWPE	Ultrahigh Molecular Weight Polyethylene
UMT	Universal Material Tester
VESPERS	Very Sensitive Elemental and Structural Probe Employing Radiation from a Synchrotron
WED	Western Economic Diversification Canada
XANES	X-ray Absorption Near Edge Structure
XAS	X-ray Absorption Spectroscopy
XPS	X-ray Photoelectron spectroscopy
XRD	X-ray Diffraction

CHAPTER 1
INTRODUCTION

1.1 Research motivation

Annually, millions of hip joint replacement surgeries are performed worldwide [1]. A hip prosthesis consists of four components that replicate the hip joint: an acetabular cup, a liner, a femoral head, and a stem. Typically, a femoral head is made of a CoCrMo alloy and a liner is made of an Ultrahigh Molecular Weight Polyethylene (UHMWPE) [2]. The femoral head articulates against the liner and these bearing surfaces suffer from friction, wear, and corrosion during the movement of the human body. The wear of the polymer liner and the corrosion of the CoCrMo alloy are the main failure mechanisms in artificial hip joints, which limit their durability and lifetime [2]. Therefore, it is necessary to improve the functionality of these bearing surfaces. A promising approach is to engineer the CoCrMo alloy with a biocompatible inert hard coating. The purpose of this research is to develop Ta and DLC thin films on the CoCrMo alloy sheets to improve its surface functionality for orthopedic implant applications.

Recently, Ta has been attracting increasing attention for biomedical applications due to its good mechanical properties, good corrosion resistance, and high biocompatibility [2]. Ta thin films exist in different crystal structures with different properties, and the formation of the different phases is highly dependent on deposition parameters. In addition, information on some phases of Ta is very limited and their properties could not be measured yet. Controlling the synthesis of Ta thin films with desired structure would be an advantage. Moreover, achieving high quality Ta coatings with high adhesion on CoCrMo alloy would overcome one of the barriers of using Ta thin films for biomedical applications.

DLC possess high hardness, low friction coefficient, high wear resistance, high corrosion resistance, and excellent biocompatibility, making it ideal for orthopedic implant applications [2].

However, DLC coatings usually have high level of internal stress because of high energy ion bombardment during the deposition process, which induces early coating delamination or spallation. Therefore, it is very important to measure and control the internal stress of DLC coatings. In addition, DLC coatings usually have weak adhesion to metallic substrates. Although various approaches have been explored to improve the adhesion of DLC coatings, very limited data has been reported in using biocompatible Ta thin films as an interlayer for enhancing adhesion of DLC coatings on the biomedical CoCrMo alloy.

1.2 Research objectives

The overall purpose of this PhD research project is to synthesize adherent Ta thin films with controlled crystal structures on CoCrMo alloy sheets for improved wear and corrosion resistance and to evaluate the feasibility of using Ta for enhancing adhesion of DLC thin films on the CoCrMo alloy sheets. The specific objectives of research are:

- Synthesize single phased α- and β-Ta thin films on CoCrMo alloy sheets with high adhesion for wear and corrosion protection;
- Fabricate stable face-centered cubic (fcc) Ta thin films with high purity for structure and property evaluation;
- Evaluate the feasibility of using Ta interlayers to enhance the adhesion of DLC thin films on CoCrMo alloy sheets;
- Evaluate the appropriateness and reliability of using optical profiler for stress measurement of DLC.

1.3 Research contributions

- Highly adherent Ta coatings have been deposited on CoCrMo alloy sheets with improved wear and corrosion resistance.
- Stable fcc Ta thin films with high purity have been obtained for the first time.

1.4 Thesis organization

This thesis consists of nine chapters. The thesis organization is listed as follows:

Chapter 1 provides a brief introduction of the research project including motivation, objectives, and thesis organization.

Chapter 2 provides a comprehensive literature review on artificial hip joints, application of CoCrMo alloys in artificial hip joints, and improvement of the functionality of CoCrMo alloys in artificial hip joints using surface treatments such as coating. Afterwards, two main types of coatings, Ta and DLC, their properties, their deposition techniques, and their applications in orthopedic researches are reviewed.

Chapter 3 introduces materials, equipment, and characterization techniques used in this research. Magnetron sputtering and ion beam systems used for Ta and DLC thin films deposition will be described in detail. In addition, characterization techniques applied in this research will be explained.

Chapters 4, 5, and 6 focuses on Ta thin films. Chapter 4 presents the growth and characterization of Ta thin films on CoCrMo alloy sheets for orthopedic implant applications. In this study, the effect of deposition parameters on the formation of α- and β-Ta thin films, and the development of adherent Ta thin films (α- and β-Ta) on the CoCrMo alloy are explained. Chapter 5 reports the surface properties, tribological and corrosion behavior of the Ta coated CoCrMo alloy sheets. Chapter 6 gives the structure, formation mechanism, and stability of fcc Ta thin films.

Chapter 7 and 8 focuses on DLC thin films. Chapter 7 describes the adhesion of DLC coatings on CoCrMo alloy sheets using Ta interlayer. Chapter 8 reports a simple non-destructive method for measurement of stress in DLC coatings using an optical profiler.

Finally, conclusions and suggestions for future work are summarized in Chapter 9.

CHAPTER 2
LITERATURE REVIEW

This chapter provides a comprehensive review of previous research findings on artificial hip joints, application of CoCrMo alloys in artificial hip joints, and improvement of the functionality of CoCrMo alloys in artificial hip joints using surface treatments such as coating. Afterwards, two main types of coatings, Ta and DLC, their properties, their deposition techniques, and their applications in orthopedic researches are reviewed.

2.1 Overview of artificial hip joints

Osteoarthritis is the most common disease that is associated with the erosion of joints cartilage. Osteoarthritis causes pain and disability, and its final remedy is joint replacement. The number of hip replacement surgeries is increasing exponentially. The latest information reported by Canadian Joint Replacement Registry Annual Report in 2014-2015 indicated an increase of 20.0% hip replacement surgeries in Canada over 5 years, while 8.5% of these replacement surgeries were revision surgeries [1].

An artificial hip joint consists of four parts (Figure 2.1) [3]:
- Acetabular cup or shell that is fixed to the hip socket;
- Liner that fits between the acetabular cup and the femoral head;
- Femoral head that articulates with the liner;
- Stem that is inserted into the thigh bone.

The bearings are the two parts of the artificial hip (liner and femoral head) that glide together throughout motion. Wear, friction, corrosion, and biocompatibility of the bearings are the main factors limiting the durability and lifetime of artificial hip joints [2]. Lack of durability of artificial hip joints has unacceptable effects such as pain and disability on patients, and finally results in the need for a revision surgery that is more complex compared to the primary surgery.

Revision surgery reduces the quality of patients' life besides requiring longer recovery time and higher cost. Therefore, it is very important to extend the durability and lifetime of implants. Choosing the proper material combinations to improve the durability and lifetime of the bearing surfaces in artificial hip joints has remained a focus of research interests.
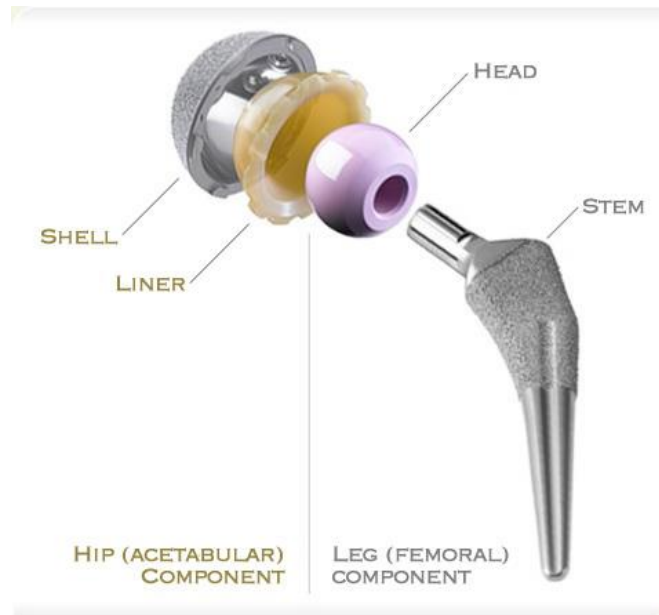
Figure 2.1. Artificial hip joint components [3]

2.1.1 Artificial hip joint materials

All parts of the artificial hip joints can be engineered using different materials. The femoral head and liner, based on material combinations, can be Ceramic on Ceramic (CoC), Ceramic on Polyethylene (CoP), Ceramic on Metal (CoM), Metal on Metal (MoM), Metal on Ceramic (MoC), and Metal on Polyethylene (MoP) [4].

Most artificial hip joints comprise of a metallic femoral head that articulates against a polyethylene liner [2]. The metallic component is usually made from CoCrMo alloys, because of the excellent mechanical properties (strength and toughness), wear resistance, corrosion resistance, and biocompatibility of these alloys, whereas the polymer component is mainly made from UHMWPE [2]. CoCrMo alloys were introduced by Elwood Haynes in 1900, who reported that Mo element addition improved the mechanical properties of the alloys substantially [5]. CoCrMo alloy with the ASTM standard of F1537 is the one usually used to make orthopedic implants [5, 6]. Sir John Charnley introduced UHMWPE for orthopedic implants in 1960 [4, 7, 8].

Despite the significant properties of these material combinations, human body system (patient's level of activities, body weight, and quality and quantity of body fluid) decreases the functionality of these kinds of artificial hip joints. For example, the friction of these bearing surfaces in the body fluid increases the corrosion rate of the CoCrMo alloy, releases toxic Cobalt (Co) and Chromium (Cr) ions, which can cause some health issues. Moreover, the metal and polymer wear debris produced due to the sliding between the two bearing surfaces increases the friction and wear of the bearings, ultimately limiting the lifetime of the implants [2, 9].

2.1.2 Improving the functionality of the artificial hip joints using surface treatments

Various surface treatments have been used to improve the durability and lifetime of bearing surfaces. Surface texturing has been introduced as an attractive approach for this purpose. This method is inspired by the microtexture existing on natural articular cartilages. Surface texturing can reduce the contact area between the two bearing surfaces. Moreover, this method can alter the interfacial flow and film thickness of lubricating fluids locally, change the bearing pressure distribution, serve as channels to supply lubricant to the surfaces, and thus affect the tribological behavior of the surfaces. An appropriate texture design could lower friction coefficient and wear between the bearing surfaces [4, 10, 11]. However, corrosion and biocompatibility issues of the bearing surfaces cannot be overcome by this method.

Another promising approach is to engineer the bearing surfaces by depositing thin films with excellent biocompatibility and superior mechanical properties. Deposition of thin films on the implants would combine the properties of the bulk substrate materials with the excellent degradation resistance of the surface films. Thus the performance of the implants would be greatly improved. However, the major issue of the thin films is their weak adhesion to the substrates owing to the internal stresses induced into the thin films during deposition and the differences in physical properties between the thin film and the substrate, which limits their applications. Dipankar *et al*. [2] reviewed the advantages and disadvantages of four main types of thin films that have been mostly investigated for orthopedic applications. This review is summarized in Table 2.1.

2.2 Overview of metallic tantalum in biomedical applications

Ta has been discovered by Anders Ekeberg in 1802 [12] and has drawn increasing attention in recent years for orthopedic implant applications due to its high hardness, low ion release rate, high corrosion resistance, low toxicity, high biocompatibility, and high wettability [2].

2.2.1 Ta phases

Metallic Ta generally exists in body-centered cubic (bcc) crystal structure (α-Ta) over a wide range of pressure and temperature as an equilibrium phase. However, it can also exist in three other allotropic forms, tetragonal (β-Ta), face-centered cubic (fcc), and hexagonal close-packed (hcp) forms. β-Ta is a metastable phase, which usually exists in Ta thin films mixed with α-Ta [13-15]. Table 2.2 shows the physical properties of bulk α-Ta, and sputtered α- and β-Ta [16-21]. α-Ta films exhibit good ductility and relatively low hardness (7-12 GPa), whereas β-Ta films are brittle and hard (Hardness = 12-20 GPa) [17, 22-26]. However, there is limited information about fcc Ta [27-32] and hcp Ta [32, 33], since fcc and hcp Ta have only been observed as fine grains dispersed in other Ta phases.

Table 2.1. Advantages and disadvantages of thin film materials [2]

Thin film	Advantages	Disadvantages
Ta	Low ion release High corrosion resistance Low toxicity High biocompatibility High wettability	Hard to obtain desirable crystal structure on biomedical alloys with sufficient adhesion
DLC	Hard Low friction High wear resistance Corrosion resistance Chemical inertness Biocompatible	Brittle High internal stress up to 10 GPa or more
Graphite-like Carbon (GLC)	Moderate hardness Wear resistance Lower friction than DLC High load-bearing capacity Low internal stress	Hardness is lower than DLC

	Titanium Nitride (TiN)	Hard Wear resistance Corrosion resistance	Enhance wear by abrasion of the opposing surface

Table 2.2. Physical properties of Ta [16-20]

	Bulk α-Ta	Sputtered α-Ta	Sputtered β-Ta
Structure	bcc-Im3m a=b=c=3.30 Å	bcc-Im3m a=b=c=3.31-3.33 Å	Tetragonal-p42/mnm a=b=5.31 Å c=10.19 Å
Density (g/cm^3):			
- Theoretical	16.7	16.3-16.6	16.9
- Observed	16.6	15.6	15.9
Resistivity (μΩ.cm)	13	24-50	180-220
Thermal stability		$T_{melting\ point}$ at 2996 °C	$T_{\beta\ to\ \alpha\ transformation}$ at 750–775 °C

2.2.2 Ta thin films and deposition techniques

The high cost and the difficulty in making dense Ta implants limit its applications [34, 35]. Therefore, applying Ta thin films is considered a promising way to take the advantages of this valuable material. Various techniques have been used for the production of Ta thin films:

- Electrochemical deposition from molten salts
- Chemical Vapor Deposition (CVD)
- Physical Vapor Deposition (PVD)

Electrochemical deposition from molten salts is based on the reduction of metal ions from an electrolytic solution on the substrate at high temperature. High temperature working condition limits this method for deposition of Ta thin films on low temperature resistance alloys [36].

CVD technique is based on the chemical reactions of gaseous reactants on or near the heated substrate surface to assist the atomic deposition of solid films on the substrate. In this method, a set of chemical reactions has to be defined to the deposition of Ta thin films. Moreover, the structure of the films is highly dependent on the deposition parameters and the defined chemical reactions [37, 38].

In PVD technique the film materials are evaporated by different mechanisms under high vacuum, the vapor phase is transported to the substrate, depositing a thin film. Based on the production method of the vapor phase, PVD technique can been classified as vacuum evaporation and sputter deposition. In vacuum evaporation, film materials are heated to be vaporized under high vacuum and the vaporized atoms are transported through vacuum and deposited on the substrate. Very high heating temperature (above 3350 °C) is required for Ta to be vaporized, therefore, this technique is not applicable for Ta film formation.

Ta thin film deposition in most of the previous research studies have been carried out using sputtering. In the sputtering methods, sputtering gas ions are accelerated toward the target (film material) using an electrical field, bombard the target with high energy, transfer their momentum to the target material, and finally cause the material to be sputtered. The sputtered materials are transported and deposited onto the substrate [39]. As sputtering does not require melting and evaporation of the target materials, most of the materials can be deposited by this technique regardless of their melting temperature. It is one of the most effective ways for deposition of high purity metal and alloy films [39].

2.2.3 Parameters that affect Ta thin films formation in sputtering methods

Ta thin films can be deposited using sputtering. The deposition parameters and the substrate material have considerable effects on the phase formation (α, β, or a mixture of α and β) of Ta films. Films containing a mixture of α- and β-Ta can be easily deposited, but it is hard to obtain single phased α- and β-Ta thin films or to accurately control the crystal structure of Ta thin films in order to meet the demand of practical applications. A review of some main deposition parameters which affect the Ta phase formation are presented as follows:

In some researches, the formation of β-Ta metastable phase was explained by the fact that atoms creating a lattice are not in the lowest energy positions [40, 41]. In other words, certain ion/atom bombardment energy is necessary for the formation of lattices in equilibrium positions. It indicates the important role of ion/atom bombardment energy in the formation of stable and metastable phases of Ta. Excessive ion/atom bombardment energy results in direct implantation of unstable lattice positions whereas insufficient ion/atom bombardment energy to overcome the barriers in the surface results in the arrangement of atoms not in their lowest energy positions. These

mechanisms define a "window of total ion/atom energy", where excessive and insufficient energy result in the formation of β phase [40, 41]. The effect of substrate biasing on the Ta phase formation [14, 42-44] can be explained by this energy window.

Read *et al*. [16] indicated that β-Ta forms in clean vacuum condition, whereas, α-Ta phase is stabilized by impurities like oxygen and nitrogen in the deposition chamber. The results presented by Nakamura *et al*. [45], Das [46], Gersteng [47], Krikorian [48], and Baker [49] agree well with those reported by Read *et al.* [16]. However, Westwood [50], Shwartz *et al.* [51], Axelrod *et al.* [52], Sosniak *et al.* [53], Feinstein *et al.* [54], Schauer *et al.* [55, 56] obtained opposite results. The mechanism of how impurities affect the formation of Ta phases is still under investigation.

Deposition temperature is a key factor that determines the crystal structure of Ta films. Increasing the substrate temperature leads to increased mobility of atoms on the surface and these more mobile atoms have higher possibility to find lower energy positions to form equilibrium α-Ta phase [14, 26, 57-59].

α-Ta phase was also found to preferentially form on the substrates of similar crystal structure with comparable lattice parameters. In this case, the atoms need less energy to sit on their equilibrium positions [14, 25, 60-64]. Niobium (Nb) [14, 60-62], Aluminum (Al) [63], and Titanium (Ti) [25, 64] are some substrate materials that promote α-Ta phase formation.

2.2.4 Ta thin films on CoCrMo alloy substrates for artificial hip joint applications

Deposition of Ta thin films on CoCrMo alloys would combine the high mechanical strength of the substrate alloy with the excellent biocompatibility of Ta film and thus improve their performance as biomedical implants [13, 33, 65-68]. In 2005, Spriano *et al*. [65] tried to modify the surface of the Co alloy sheets with Ta enriched layers to improve their biocompatibility and wear behavior. The modification was carried out in a solid salt mixture (NaCl 47 wt.%, K_2TaF_7 52 wt.%, and Ta 1 wt.%) at temperatures ranging from 800 to 1000 °C for one to two hours with Argon (Ar) flowing. Ta enriched layers of 1-3 μm thickness consisting of $CoTa_3$ and Co_2Ta intermetallic compounds appeared on the surface of the Co alloy sheets. The modified alloy sheets showed improved wear performance, lower coefficient of friction, lower ion release rate, and higher wettability compared to the untreated alloy sheets. In 2012, Balagna *et al*. [33, 66] investigated the

deposition and wear behavior of a multilayered Ta structure on the CoCrMo alloy. The multilayered structure consisting of tantalum carbides (TaC and Ta_2C) and metallic Ta (hcp structure) as a top layer of 1 μm thickness was deposited on the CoCrMo alloy by keeping the alloy samples in a solid salt mixture (K_2TaF_7 98 wt.%, and Ta wt.2%) at 950-1000 °C for 30-60 mins with Ar flowing. The results showed that the surface modification significantly improved the wear behavior of the alloys. In 2013, Hallmann *et al*. [13] reported the deposition of α-Ta thin films, 20-600 nm thick, on the CoCrMo alloy and the TiAlNb alloy using magnetron sputtering. They investigated the effect of sputtering parameters and substrate materials on Ta phase formation. However, no information was provided regarding the adhesion and properties of the Ta thin films deposited on the alloys. Dorn *et al*. [68] in 2014 investigated the corrosion behavior of CoCr alloy modular necks coated by Ta film using a hip simulator in a calf serum environment. Although no information on the Ta film deposition and structure was provided, they confirmed the protective effect of Ta film and evaluated the associated risk of failure when used as implants.

In summary, the controlled synthesis of Ta thin films on the CoCrMo alloy with desired crystal structure and high adhesion is very important for artificial hip joint applications. However, there is no systematic investigation in this regard so far. Therefore, part of the present thesis (Chapter 4) focuses on controlled synthesis of adherent Ta thin films on the CoCrMo alloy with different crystal structures using a magnetron sputtering deposition technique. Furthermore, the tribological and corrosion behavior of the thin films is investigated for the purpose of evaluating their potential to meet the demand for orthopedic implant applications and presented in chapter 5.

2.2.5 fcc Ta

fcc Ta formation has been reported only in a few journal articles under special processing conditions as dispersed fine grains embedded in α- and/or β-Ta thin films [27-31], or in heavily deformed bulk samples of Ta [32]. Ta with fcc structure was first reported by Denbigh *et al*. in 1966 [27]. They found epitaxial growth of fcc structure on MgO substrate in ultrathin (< 10 nm) Ta films deposited by electron beam evaporation below 400 °C, however, the film gradually changed to α-Ta when the film thickness increased from 10 nm to 25 nm, where only dispersed fcc fine grains existed, and fcc Ta grains disappeared when the thickness became greater than 25 nm. One year later, Chopra *et al*. [28] reported the nucleation of fcc Ta in Ta films of 50 nm thick

deposited by sputtering at temperatures below 400 °C. They attributed the nucleation and stabilization of fcc Ta to the relatively higher kinetic energy and higher electrostatic charges in the sputtering technique compared to evaporation. In 1968, Marcus *et al.* [29] further reported that fcc Ta structure could only exist in very thin (10 nm or thinner) Ta films deposited using electron beam evaporation technique due to the large contribution of surface forces and the incorporation of surface impurities. A subsequent study by Schrey *et al.* in 1970 [30] confirmed fcc Ta formation in very thin films (with thickness less than 20 nm) using radio frequency sputtering at 325 °C. Recently, Janish et.al. [31] tried a different approach in investigating fcc Ta formation. They found nucleation of fcc Ta in amorphous Ta thin films of 20 nm thick when annealed at 450 °C. In all the aforementioned published research papers, only a small amount of very fine fcc grains was found in the Ta films. Furthermore, in all the reported cases, the fcc structure of Ta disappeared when the film thickness or substrate temperature increased beyond a value. In addition, dispersed nanosized fcc Ta grains were found in heavily deformed bulk bcc Ta samples [32]. Nevertheless, up till now, only a small amount of nanosized fcc Ta grains have been obtained and observed using Transmission Electron Microscopy (TEM), which were embedded in other phases of Ta (α-Ta, β-Ta, or their mixture). Thus, the processing conditions and structural information on fcc Ta are very limited, and the properties of fcc Ta could not be measured. In the present thesis work, further attempt is made to synthesize stable fcc Ta thin films with high purity and to evaluate its structure and properties (Chapter 6).

2.3 Overview of DLC in biomedical applications

DLC thin films have high hardness, low friction coefficient, high wear resistance, and high biocompatibility, and thus attract considerable attention for many tribological applications, especially medical applications. DLC is one of the best candidates for improving the lifetime of human implants including artificial hip and knee joints. High quality DLC thin films have demonstrated great potential in reducing wear and friction coefficient of these implants [2, 69].

2.3.1 Structure and properties of DLC thin films

DLC is a carbon-based amorphous material containing diamond (sp^3) and graphitic (sp^2) bonding. It has high sp^3/sp^2 ratio with diamond-like properties. DLC exists in two major categories: amorphous carbon (a-C) and hydrogenated amorphous carbon (a-C: H). Figure 2.2 shows the

composition of different forms of amorphous carbon using a ternary phase diagram. The a-C is denoted as tetrahedral amorphous carbon (ta-C), when the percentage of sp^3 bonding is high. The center of the diagram is occupied by a-C: H with relatively high sp^2/sp^3 ratio and high hydrogen content while more sp^3 bonding with less hydrogen produces hydrogenated tetrahedral amorphous carbon (ta-C: H) [70]. Some of the properties of DLC compared to other carbon based materials are listed in Table 2.3.
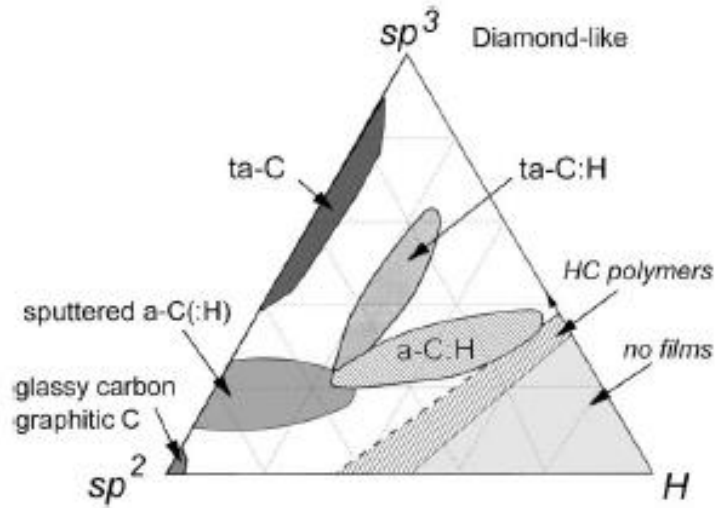
Figure 2.2. Ternary phase diagram of amorphous carbon [70]

Table 2.3. Properties of the various forms of DLC compared to diamond, graphite, C_{60}, and polyethylene [70]

	sp^3 (%)	H (%)	Density (gcm^{-3})	Hardness (GPa)
Diamond	100	0	3.515	100
Graphite	0	0	2.267	
C_{60}	0	0		
Glassy C	0	0	1.3-1.55	3
Evaporated C	0	0	1.9	3
Sputtered C	5	0	2.2	
ta-C	80-88	0	3.1	80
a-C: H hard	40	30-40	1.6-2.2	10-20
a-C: H soft	60	40-50	1.2-1.6	<10
ta-C:H	70	30	2.4	50
Polyethylene	100	67	0.92	0.01

2.3.2 DLC thin films deposition techniques

DLC coatings can be produced by various PVD or CVD techniques from a variety of solid or gaseous carbon sources. The methods include ion beam, sputtering, cathodic arc, pulsed laser deposition, plasma enhanced chemical vapor deposition [70].

Ion Beam Deposition (IBD) has been widely used for DLC film deposition. In this method, carbon ions or hydrocarbon ions created in an ion source are accelerated towards the substrate to form DLC films. DLC formation is highly dependent on the ion energy of the incident particles. In this method, ion energy and ion current density can be controlled independently to control the deposition, which is an advantage over other deposition methods.

2.3.3 DLC thin films on CoCrMo alloys substrates in artificial hip joints applications

The performance of DLC films on the Co alloy substrates has been studied and conflicting results were reported [71-76] between 2001 and 2010. The major challenge is the issue of weak adhesion of DLC films to the Co alloy substrates.

In general, owing to the high level of internal stresses of DLC films due to the high energy ion bombardment during the deposition processes and the large differences in physical properties between DLC and the substrates, DLC adheres weakly to most of the metallic substrates. Muller *et al*. [77] and Fallub *et al*. [78] in the year 2011 specifically analyzed the interface of DLC films on a CoCrMo alloy and indicated that the interface is a main factor to control the adhesion. They found that a very thin layer consisting of a mixture of carbides from all the alloy's metals formed at the interface and these interfacial carbides played an important role in the adhesion failure of DLC films on the CoCrMo alloy. Several approaches have been investigated to overcome these drawbacks and improve the adhesion of DLC films on CoCrMo alloys. These include designing a proper interlayer and changing the composition of the thin films by doping. In this regard, Falub *et al*. [78, 79] showed that the adhesion of DLC film on a CoCrMo alloy can be greatly improved by introducing a 90 nm thick Mo interlayer [78] or a Si-doped DLC interlayer [79]. Liu *et al*. [80, 81] and Guo *et al*. [82] also demonstrated better performance of DLC coatings on CoCrMo alloys through the application of Ti and Cr interlayers, respectively. These interlayers improve the adhesion by enhancing the interfacial bonding between the substrates and the DLC. However,

Huart *et al*. [83, 84] showed the failure of a DLC coated CoCrMo alloy that contained a 120 nm thick Si interlayer. In this case, the coating delamination was attributed to in-vivo crevice corrosion of the interlayer.

Recently, Ta has been introduced by Thorwarth *et al*. [85] as a promising candidate material for use as an interlayer to enhance DLC adhesion on CoCrMo alloys. Ta layer could also improve the performance of DLC due to its excellent corrosion and mechanical resistance, high biocompatibility, insolubility in body fluids, and good fatigue properties under long-lasting mechanical cyclic stresses. They reported that amorphous/α-Ta interlayers performed well with no evidence of corrosion or mechanical failure. However, very low contamination during the Ta interlayer deposition led to the formation of β-Ta, which caused coating failure.

In one word, DLC is a very promising material for coating implants, but its weak adhesion to the implant materials limits the application. In this regard, part of the present thesis (Chapter 7) attempts to evaluate the feasibility of using biocompatible Ta interlayer for enhancing DLC coating adhesion on the CoCrMo alloy. Measuring of DLC coating's internal stresses is an advantage to control the DLC deposition parameters and to deposit a high quality DLC coating. In this regard, Chapter 8 evaluates a simple non-destructive method as an appropriate and reliable method for DLC stress measurement. In these works, ion beam deposition technique is used to deposit the DLC films.

CHAPTER 3
MATERIALS AND EXPERIMENTAL METHODS

In this research work, magnetron sputtering and ion beam systems were used for thin film deposition. The thermal stability of the thin films was investigated by treating the samples at different temperatures using a furnace. Surface morphological, chemical and structural, and properties characterization of the samples were studied by different techniques including SEM, optical profiler, contact angle goniometer, optical microscope, XRD, XPS, XAS, Raman spectroscopy, Rockwell C indentation testing, nano-indentation, tribological testing, and corrosion testing. This chapter provides detailed description of the materials, equipment, and characterization techniques used in this work.

3.1 Materials

CoCrMo alloy

ASTM F1537 CoCrMo alloy prepared by M. Vincent & Associates Inc. was used as substrate. This ASTM F1537 CoCrMo alloy meets the requirements of standard as biomedical implants. Table 3.1 and 3.2 show the chemical composition and mechanical properties of the alloy, respectively.

Silicon wafer

(100) silicon wafer of 0.5 mm thick produced by University Wafer Inc. was also used as reference substrate.

Tantalum

Metallic Ta of 99.9% purity produced by Plasmionique Inc. was used as sputtering target.

Table 3.1. Chemical composition of the CoCrMo alloy

Element	wt%
Cr	27.7
Mo	5.48-5.51
Si	0.61-0.74
Mn	0.65
Fe	0.18-0.19
N	0.148-0.157
C	0.055
Ni	0.03
W	0.02
P	0.005
S	0.0004-0.0005
Co	balance

Table 3.2. Mechanical properties of the CoCrMo alloy

Rockwell Hardness	38-42 HRC
Ultimate tensile strength	1339-1344 MPa
Yield strength (0.2% offset)	927-931 MPa
Elongation at fracture	37.2-40.2%
Reduction in area	26.0-26.4%
Phase transition temperature	1150 °C

3.2 Thin film deposition

3.2.1 Magnetron sputtering deposition

Magnetron sputtering, the most common method for depositing uniform and adherent metal films, was used for Ta thin film deposition in this thesis work. The magnetron sputtering system used for the deposition is made by Plasmionique Inc. and it is located in the Department of Mechanical Engineering, University of Saskatchewan (Figure 3.1). The equipment is composed of a vacuum chamber, a pumping system, a power supply, and a computer control system. Inside the vacuum chamber, there are three magnetrons, a remote plasma source, and a substrate mounting. Each magnetron can be connected to a Direct Current (DC), a pulsed DC, or Radio Frequency (RF) power source. During the sputtering deposition process [86, 87]:

- The chamber was first evacuated to 1.33 x 10^{-4} Pa to minimize the partial pressures of all background gases and potential contaminants

- Sputtering gas, Ar, was then introduced into the chamber

- Plasma was generated by applying a high voltage between the cathode (located behind the target) and anode (connected to the chamber as electrical ground)

- Positive sputter gas ions were accelerated towards the target, these collisions causing target materials to be ejected

- Sputtered materials were transported to and deposited on the substrate to form thin films.

In the magnetron sputtering system, a magnetic field is used to confine the electrons near the target and thus enhance ionization and plasma density, leading to a higher sputtering efficiency. This is one of the main advantages of magnetron sputtering over other sputtering methods.

Ta thin film deposition in the magnetron sputtering system was performed at a pressure ranging from 0.80 Pa to 1.87 Pa by introducing Ar gas into the chamber with a flow rate of 35 sccm and using a Ta target of 99.9%. The distance between the target and the sample was 35 mm and the sample stage was made to rotate at a speed of 3 rpm. The mean voltage of the target ranged from 100 V to 200 V. Substrate temperature ranged from room temperature to 600 °C and substrate bias voltage ranged from -115 V to 0 V.

Figure 3.1. The magnetron sputtering system used in this work

3.2.2 Ion beam deposition

Because of the capability to control the ion energy and the ion current density independently, the ion beam deposition method has been widely used to produce DLC films. The dual ion beam system made by 4Wave Inc., located in the Department of Mechanical Engineering, University of Saskatchewan, was used for DLC thin film deposition in this thesis work. The main components of the equipment include a vacuum chamber, a pumping system, a power supply, and a computer control system (Figure 3.2). Inside the vacuum chamber, there are two ion sources (ion source I for etching the substrate and direct ion beam deposition, and ion source II for sputtering), a target assembly with four targets, and a substrate holder. Figure 3.3 presents a schematic structure of the system. Following procedures were used to deposit DLC thin films:

- The chamber was first pumped down to a high vacuum of 1.33×10^{-5} Pa
- Precursor gases were then introduced into ion source I
- The ions from the source directly bombarded the substrate surface to etch the substrate or to deposit DLC thin films depending on the gas composition and ion energy
- Argon gas might be simultaneously introduced into ion source II to sputter a target to obtained doped DLC thin films.

DLC thin film deposition was carried out using ion source I. The substrate holder was mounted inclined at 45° with respect to the ion source. Methane (CH_4) and Ar mixture was used as precursor gases, the working pressure was 0.0933 Pa, and the ion energy for deposition ranged from 65 eV to 85 eV.

Figure 3.2. The ion beam system used in this work
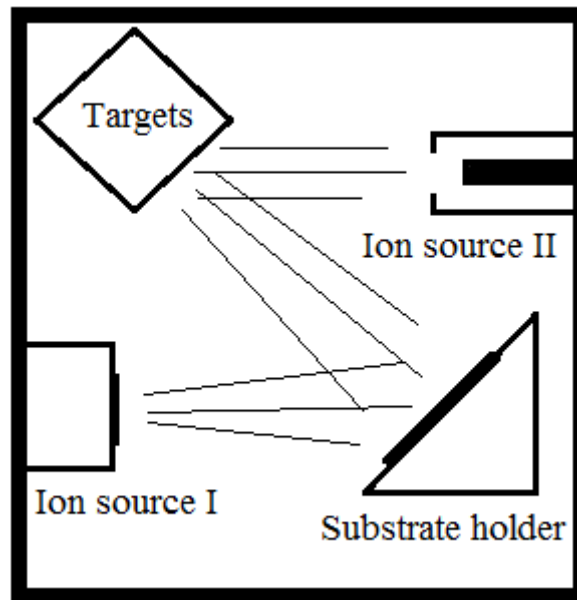
Figure 3.3. Schematic structure of the ion beam system

3.3 Heat treatment

GSL-1500X furnace located in the Department of Mechanical Engineering, University of Saskatchewan (Figure 3.4), was used to heat the thin films in order to understand their thermal

stability. The furnace includes a high purity alumina tube and a SiC heating element. A gas or gases can be introduced into the tube to control the treatment environment. The furnace can reach a temperature up to 1500 °C [88]. In the present research, fcc thin film samples were annealed at temperatures ranging from 700 °C to 900 °C for one hour. The heating rate was 10 °C/min and the samples were cooled down to room temperature with the furnace after the treatment.

Figure 3.4. The furnace used in this work

3.4 Characterization techniques

3.4.1 SEM

SEM is non-destructive and easy to use technique for surface morphology observation with a high resolution. It can provide the topography of the surface with a wide range of magnifications from 10 to 500,000 times. In this thesis work, Jeol JSM-6010LV SEM (Figure 3.5) located in the Department of Mechanical Engineering, University of Saskatchewan, and SU8010 SEM located in the Western College of Veterinary Medicine, University of Saskatchewan were used to observe the morphology of sample surface and to measure the thin film thickness using cross sectional images of the samples. The SEM uses an electron beam to create images of the samples under study. An electron gun (thermionic or field emission electron gun) produces high-energy electrons, which are focused and accelerated using magnetic and electrical fields to form a beam. When the beam strikes a sample, interactions occur and the emitted signals are detected by various detectors.

Figure 3.6a shows the main signals from a sample after illuminated with an electron beam. The signals use in a SEM include Backscattered Electrons (BSE) and Secondary Electrons (SE). BSE are produced when the incident electrons scatter backward from the sample, and SE are produced when the incident electrons loosen the electron bounds in the sample atoms, and sample electrons emerge from the surface as shown in Figure 3.6b and c. A SEM image is a distribution map of the signal intensities, which provides the details of the scanned area. BSE provides topological and compositional information of the sample, while SE provides morphological information of the sample.

Figure 3.5. The SEM used in this work
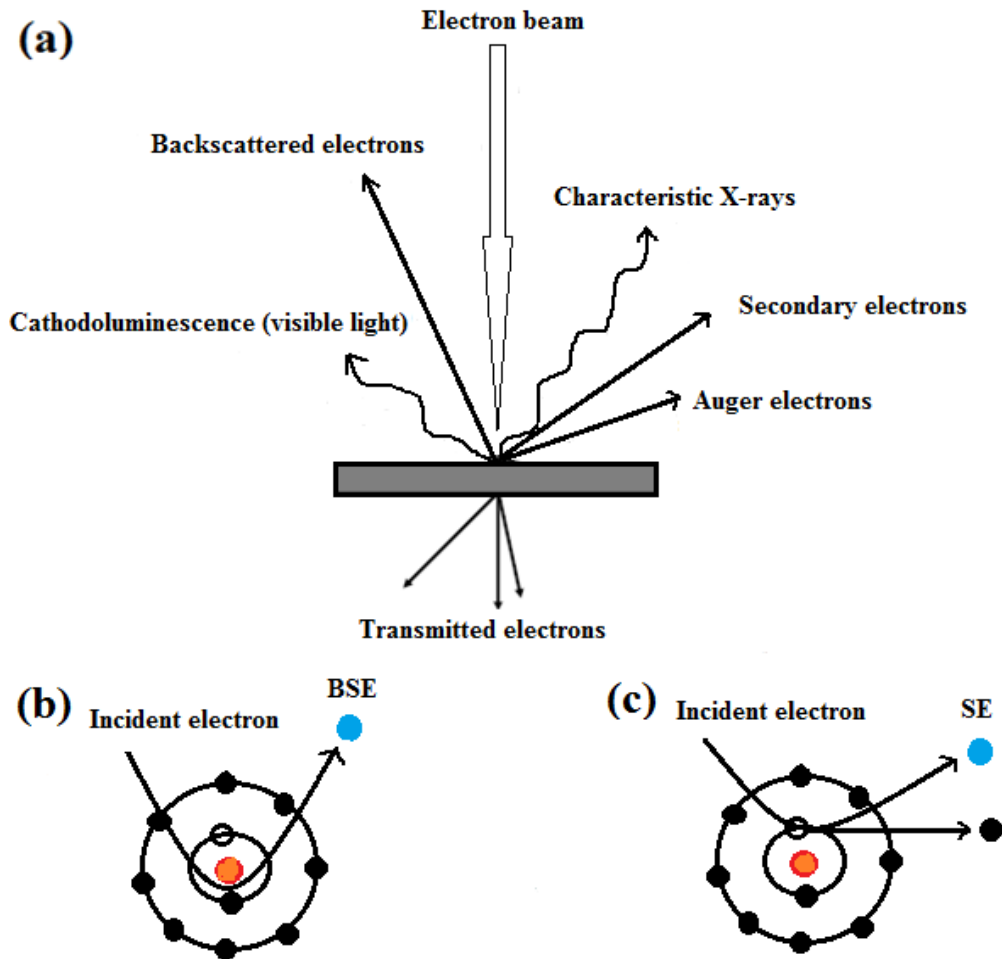
Figure 3.6. (a) Signals of the electron beam interaction with a sample (b) BSE signals principle schematic (c) SE signals principle schematic

3.4.2 Optical profiler

Optical profiler is a simple and convenient technique to observe and measure the surface topographic properties of the samples. Zygo NewView 8000 optical profiler (Figure 3.7) located in the Department of Mechanical Engineering, University of Saskatchewan, was used to measure the surface roughness, the curvature radii, and the thin film thickness of the investigated samples. The profiler uses Coherence Scanning Interferometry (CSI) to provide graphic image and high resolution numerical analysis of surfaces in three dimensions. The profiler works based on the wave properties of light as schematically presented in Figure 3.8a. The light beam is split, half the beam is reflected from the sample surface, and the other half is reflected from a reference surface, which is perfectly flat. When the distance between the beam splitter and the reference is the same

as the distance between the beam splitter and the sample, the split light beams recombine with constructive and destructive interference depends on the sample surface height variances. For example, two beams in one phase create a recombined beam with double intensity (Figure 3.8b), and two beams out of phase create a zero recombined beam. This creates light and dark bands into a camera, known as interference fringes, where the constructive interference areas are lighter, and the destructive interference areas are darker. Each pixel on the camera produces a signal, comparing the signals, and with knowing the light wavelength, surface height variances can be calculated, and three dimensions map can be achieved (Figure 3.8c) [89].

In the present thesis research, the profiler was used to measure the thickness of the thin films by measuring the height difference between the thin film and the uncoated substrate surface. In this case, part of the substrate was as covered with a tape during the thin film deposition. The profiler was also used to measure the surface roughness of the samples. Surface roughness describes the statistical distributions of surface height variations. Root mean square height (Rq) and arithmetical mean roughness (Ra) are two main parameters to present surface roughness. In this thesis work, Ra values were presented based on the topographical data of the samples surfaces on an area of 335.48 μm x 335.48 μm.

Figure 3.7. The optical profiler used in this work
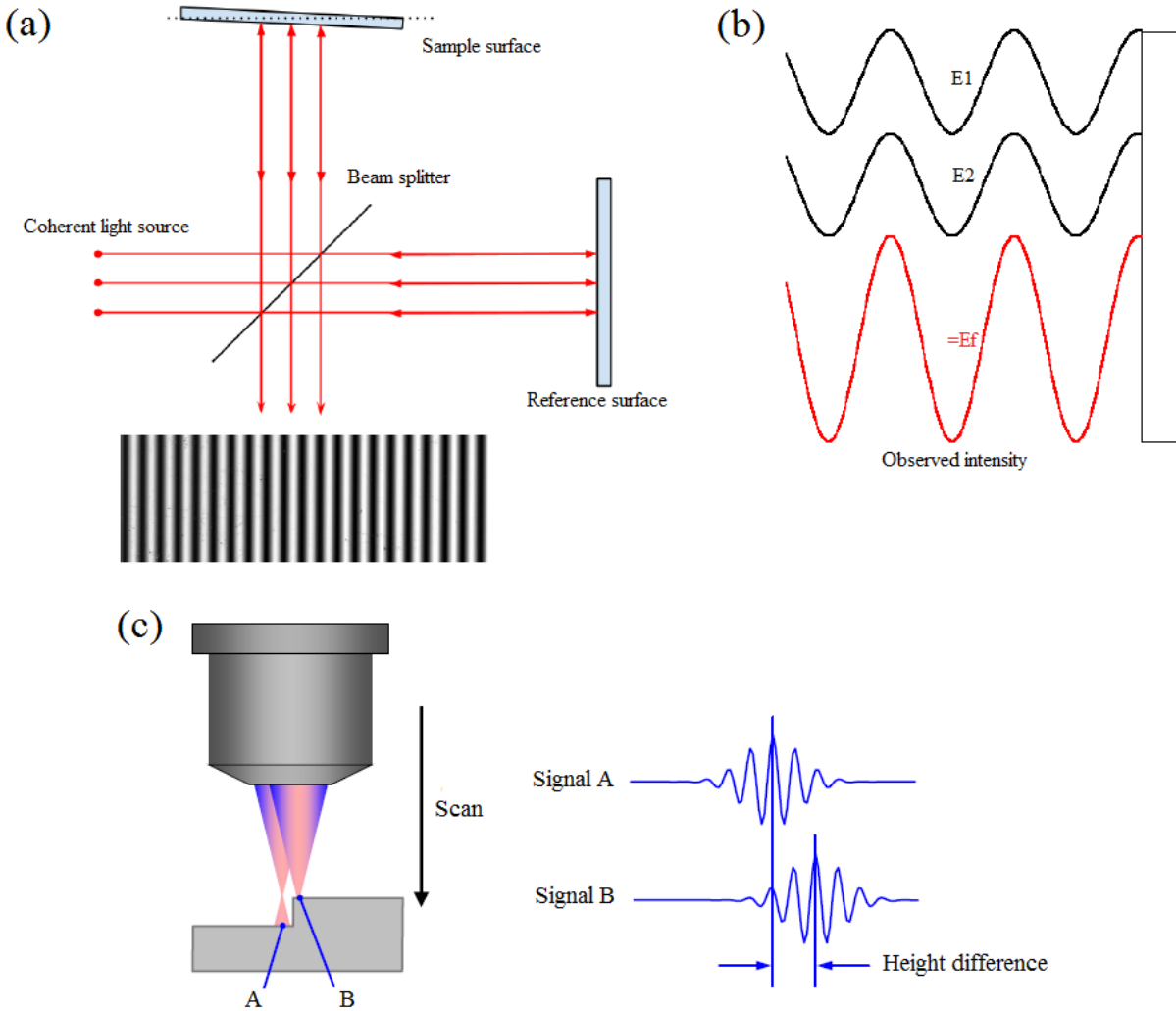
Figure 3.8. (a) Profiler operation (b) recombined beam creation schematic (c) three dimensions map creation schematic [89]

3.4.3 Contact angle goniometer

Contact angle goniometer (PG-X pocket goniometer), shown in Figure 3.9, located in the College of Agriculture, University of Saskatchewan, was used to measure the contact angle of a droplet of a solution on the samples in order to understand their surface wettability . A pump delivers a droplet of a specified solution on the sample surface and the camera equipped in the tester captures the image. The droplet volume is adjustable, and the image can be taken at static mode or dynamic mode [90].

Figure 3.9. Contact angle meter [90]

3.4.4 Optical microscope

OLYMPUS BX41M-LED optical microscope located in the Department of Mechanical Engineering, University of Saskatchewan, was used to observe wear of the UHMWPE balls after the tribology testing. Optical microscope creates a magnified image of the samples simply by using visible light and a set of lenses.

3.4.5 XRD

XRD is the most widely used non-destructive characterization technique to disclose the detailed information on materials' crystallographic structure. Rigaku Geigerflex XRD instrument with Cobalt K-alpha radiation (Co-Kα) (Figure 3.10), located in the Department of Physics & Engineering Physics, University of Saskatchewan, and grazing XRD using Very Sensitive Elemental and Structural Probe Employing Radiation from a Synchrotron (VESPERS) beamline with 15 keV energy at Canadian Light Source (CLS), were used to study the crystallographic structure of the thin films. The main components of a typical XRD are X-ray source, goniometer (sample & detector stage), X-ray detector, and electronics for counting detector pulses. During XRD process, X-ray is generated in an X-ray tube by bombarding the target material (anode) with accelerated electrons. Different target materials like Co and Cu targets produce X-rays with different wavelengths. When X-rays strike the sample surface at varying incident θ angle, diffraction of the X-rays occurs as shown in Figure 3.11. Considering the X-rays scattered from atoms P and Q in planes A and B, constructive interference of diffracted waves 1' and 2' occurs if the path length difference between them is equal to nλ, according to the Bragg's Law. Therefore:

Path length difference = $2d_{hkl}\sin\theta = n\lambda$ (3.1)

Where θ = X-ray incident angle, n = order of diffraction (an integer), λ = X-ray wavelength, and d_{hkl} = interplanar spacing of planes A and B.

The diffracted X-rays are received by the detector at angle 2θ. The intensities of the diffracted X-rays and the 2θ angles are recorded to create an XRD pattern. As such, the interplanar spacing can be calculated based on the X-ray wavelength and the diffraction angle. The interpretation of the XRD results involves comparing the measured interplanar spacing with standard reference patterns. Each crystal material has its own characteristic XRD pattern.

The X-ray source used for the CLS XRD is synchrotron light radiation. In synchrotron, electrons are accelerated to very high speeds in circular paths using strong bending electromagnets. These confined electrons in the circular path can radiate electromagnetic waves with tuned wavelengths suited to study different types of materials. High energy X-rays can be generated in synchrotron.

Figure 3.10. The XRD used in this work
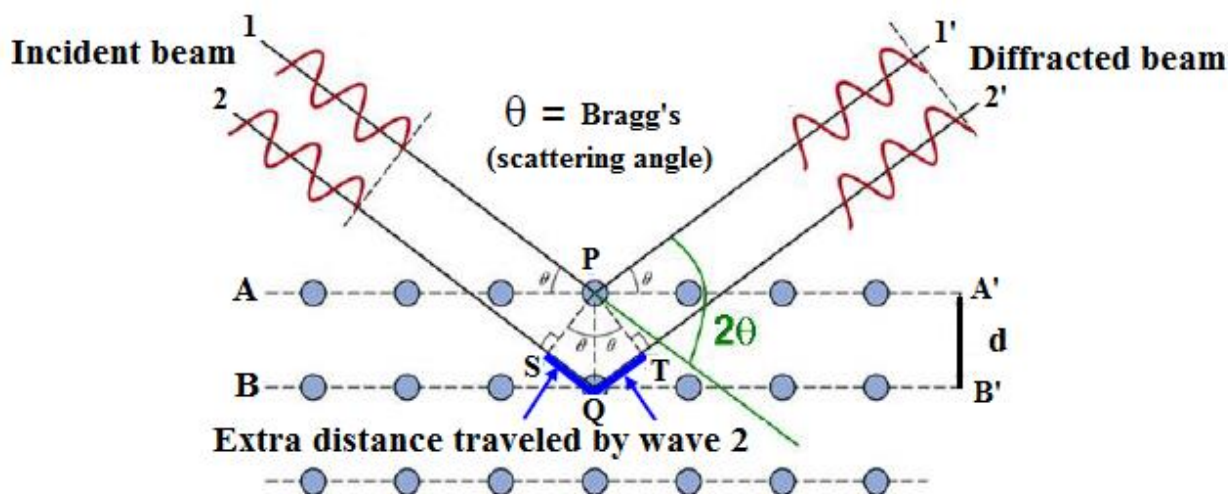
Figure 3.11. A schematic diagram of Bragg's Law [91]

3.4.6 XPS

XPS is a surface and chemical sensitive technique for chemical composition analysis. XPS (model: AIXS SUPRA) with Aluminum K-alpha (Al-Kα) radiation as the excitation source at SSSC, University of Saskatchewan, was used to investigate the chemical composition and chemical states of the thin films. X-ray interaction with the material can initiate electron transition in the material leading to ejection of photoelectrons. In XPS instrument, X-rays are generated by bombarding a metallic anode with high energy electrons, then X-rays strike the surface sample and eject electron from the shell of the sample with a measurable kinetic energy (Figure 3.12). The detector measures the ejected photoelectrons' kinetic energy, and the binding energy can be calculated using Equation 3.2:

$$E_B = h\upsilon - E_{kin} - \Phi_{work} \tag{3.2}$$

Where, E_B is the binding energy, E_{kin} is the kinetic energy, Φ_{work} is the work function, and $h\upsilon$ is the incident energy of the X-ray photons. Each atom has a unique binding energy for each shell, therefore, the energy of ejected electrons is unique for each element. In other words, each element has a unique set of binding energies. The XPS counts the number of electrons ejected from the sample's surface at a sequence of energies, and the spectra shows the plot of binding energy versus intensity. In this thesis work, the chemical states of the thin films and their depth profiling were

obtained using XPS combined by Ar ion sputtering. Each measurement consists of sequences of etching steps using Ar ions with 4 keV energy.
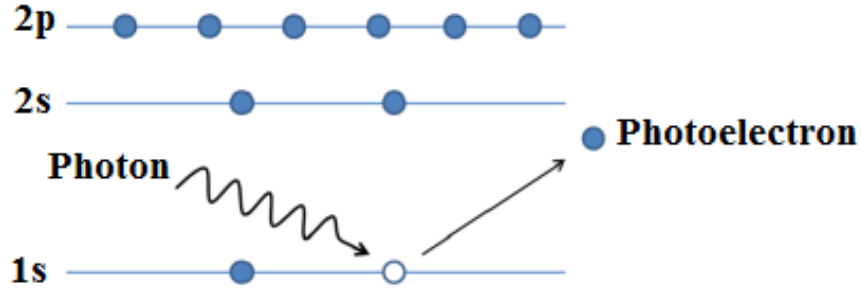
Figure 3.12. Ejection of photoelectron in the XPS [91]

3.4.7 XAS

XAS end station of Hard X-ray MicroAnalysis (HXMA) beamline at CLS was used to investigate the chemistry (oxidation state) of the Ta thin films. The XAS measurement was configured to the grazing incidence setup and the data collection was in fluorescence mode. The XAS principle is based on the X-ray absorption coefficient measurement. When a monochromatic X-ray beam with I_0 intensity, which is created in synchrotron radiation, strikes the sample, the transmitted X-ray intensity ($I(x)$) is reduced due to the X-ray absorption according to Equation 3.3:

$$I(x) = I_0e^{-\mu x} \tag{3.3}$$

Where x is the sample thickness, and μ is the absorption coefficient.

Each element has a unique binding energy, which is the energy that a core electron needs to absorb in order to escape from the nucleus, so, the absorption edge on XAS can show the element speciation of the samples. Generally, XAS shows the measurement of the absorption coefficient as a function of photon energy.

Beside transmittance, X-ray beam interaction with material can cause emission of photoelectron, auger electron, and X-ray fluorescence (Figure 3.13). Based on these emissions, there are two other methods for the XAS measurement: Total Fluorescence Yield (TFY), which measures all the

fluorescence photons and gives an exact count of absorbed photons, and Total Electron Yield (TEY), where absorption can be measured using emitted photoelectrons and auger electrons.
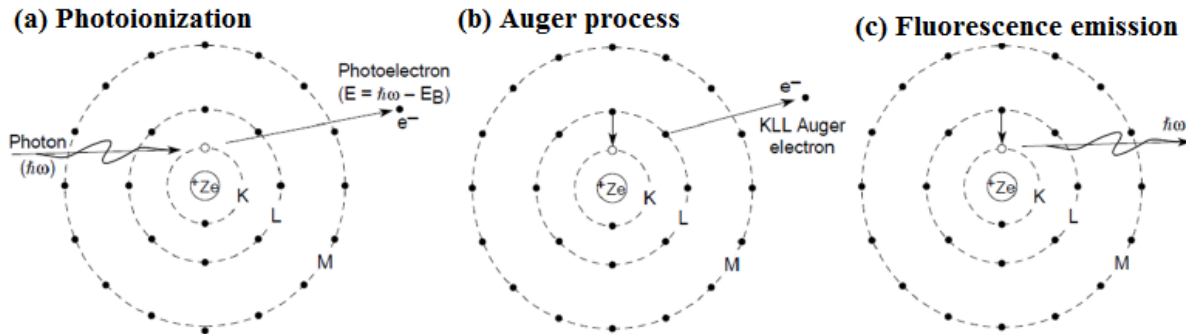
Figure 3.13. Schematic diagram of (a) emission of photoelectron, (b) emission of auger electron, and (c) X-ray fluorescence [91]

3.4.8 Raman spectroscopy

Raman spectroscopy is a powerful technique used for studying bonding structure of different forms of carbon. Renishaw model 2000 Raman spectrometer at SSSC, University of Saskatchewan, was used to obtain Raman spectra of the DLC thin films. The operating laser wavelength was 514 nm. Raman spectroscopy works based on inelastic scattering of monochromatic light. There are three basic components of the Raman spectrometer: a light source, an optical system (to collect the Raman scattered light), and a detector. The light strikes the sample surface, absorbs by sample's molecules, and scattered with a different frequency. The shift in light frequency is called the Raman shift. Raman spectrum is presented a plot of scattered light's intensity versus Raman shift. The interpretation of the plot involves comparing the obtained spectra with reference spectra.

As shown in Figure 3.14 [70], Raman spectra of different forms of carbon are widely known. Diamond has a peak at around 1332 cm^{-1}, single crystalline graphite has a peak at around 1580 cm^{-1}, and DLC has two broad peaks, D and G, at around 1350 cm^{-1} and 1580 cm^{-1}, where the position and relative intensity of the D and G peaks give detailed information about the bonding of DLC films.

29
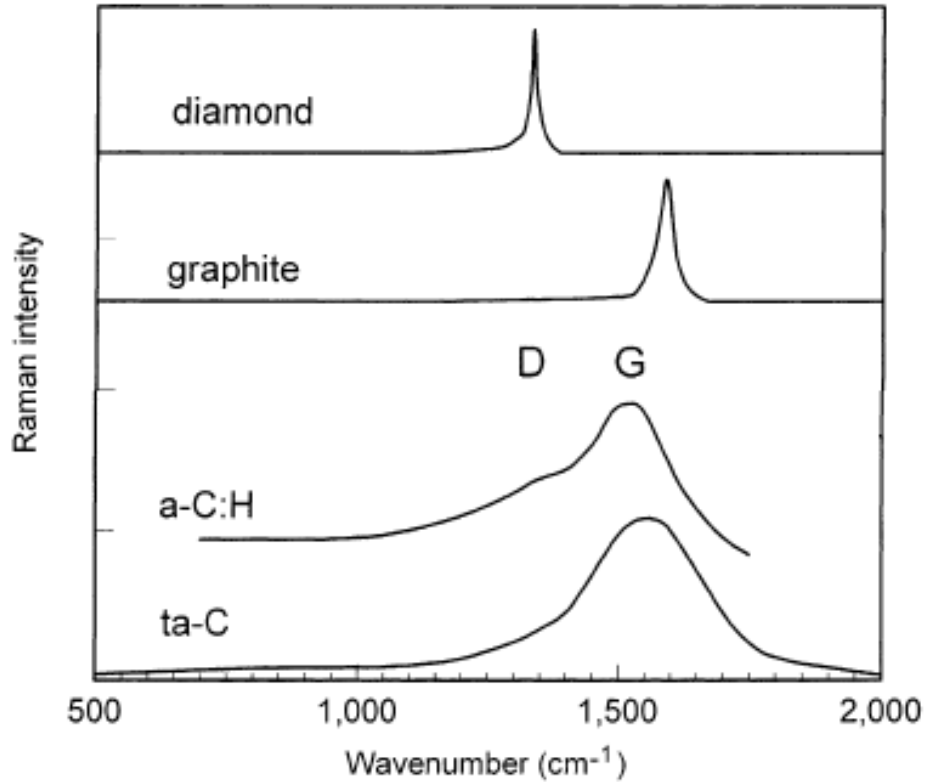
Figure 3.14. Comparison of typical Raman spectra of carbons [70]

3.4.9 Rockwell C indentation testing

Rockwell C indentation testing is a fast, easy, reliable, and low-cost qualitative technique for evaluation of coating adhesion. Instron Wolpert GmbH Rockwell C hardness tester (Figure 3.15), located in the Department of Mechanical Engineering, University of Saskatchewan, was used to evaluate the adhesion of the Ta thin films on the CoCrMo alloy. During the testing, the Rockwell C diamond indenter with a load of 1470 N was gradually pressed into the film to create an impression. Cracking and delamination of the coating occurred and extended at the area surrounding the indentation. The resistance to the propagation of the cracks was then investigated as an adhesion measurement. According to VDI 3198 guideline [92], a film with good adhesion should have less spallation and cracks around the indentation imprint comparing to the unacceptable failure images, as shown in Figure 3.16.

Figure 3.15. The Rockwell C hardness tester used in this work
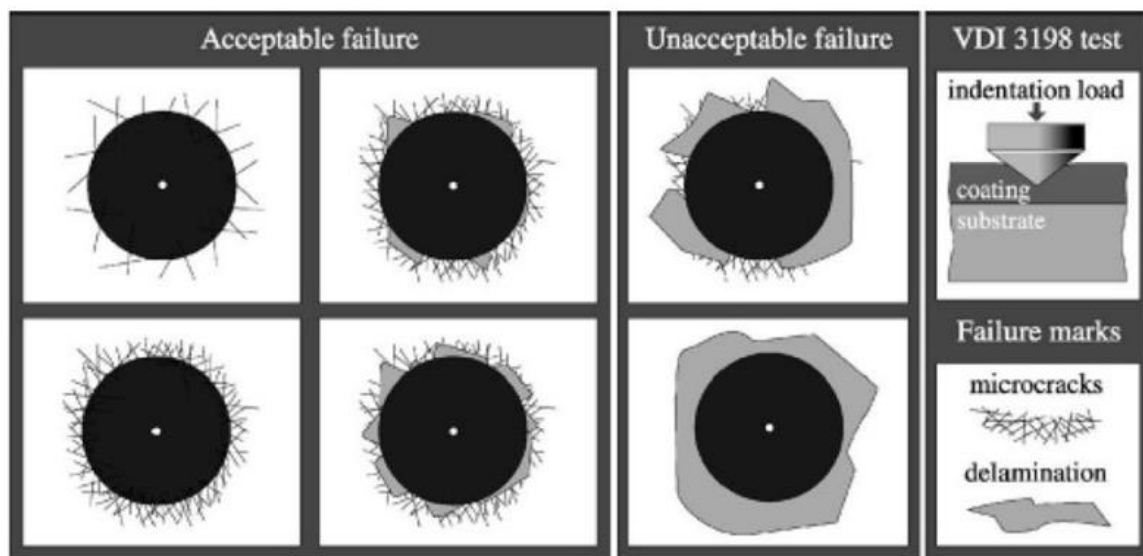
Figure 3.16. The principle of the VDI 3198 indentation test [92]

3.4.10 Nano-indentation

Nano-indentation is the main technique used to determine the mechanical properties of thin films. Nano-indentation tester (Figure 3.17) manufactured by Center for Tribology (CETR) Inc., located in Department of Mechanical Engineering, University of Saskatchewan, was used to measure the hardness and Young's modulus of the samples. A Berkovich indenter is pressed into the sample surface by increasing the load to a defined value, the indenter is left with the applied load for specific amount of time, then the load is gradually reduced to zero. During the testing, applied force and displacement are recorded and the Universal Material Tester (UMT) software analyzes the load-displacement curve to give hardness and Young's modulus. To ensure reproducibility of the hardness data, testing was performed at 50 different locations (a matrix of 5 x 10 spots) at loads varying from 0.5 to 60 mN for each sample. The hardness and Young's modulus values were achieved from the average amount of those values in the depth of one tenth of the coatings thickness in accordance with ISO 14577-4 standard [93]. It should be noted that the nano-indentation results can be affected by the roughness of the substrate's surface.
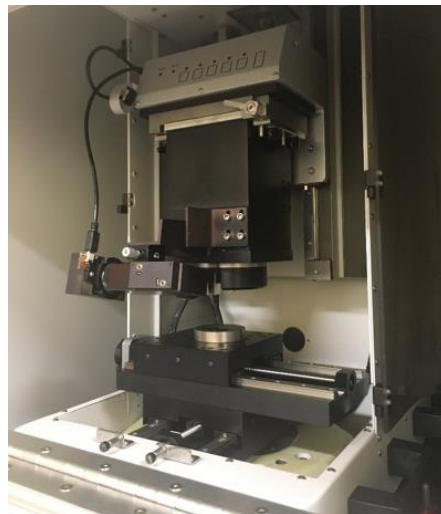
Figure 3.17. The nano-indentation tester used in this work

3.4.11 Tribological testing

In this thesis work, ball-on-disk tribo tester (Figure 3.18) built in a UMT manufactured by CETR Inc., located in the Department of Mechanical Engineering, University of Saskatchewan, was used to investigate the tribological behavior of the samples. This test method involves a ball-shaped

upper specimen that slides against a disk as a lower specimen, in a linear reciprocating motion under prescribed set of conditions of applied load, displacement, number of cycles, linear speed, and type of applied lubricant. In these experiments, UHMWPE balls with a diameter of 2 mm were sliding on Ta-coated disks and uncoated CoCrMo alloy disks in a phosphate-buffered saline (pbs) solution at room temperature, in accordance with ISO 14242-1 standard [94] specified for wear of hip joint prostheses. The load applied was 10 N and the displacement length was 2.5 mm. A linear speed of 5 mm/s was used and the movement was repeated for 10,000 cycles. The UMT software provides the actual applied load, friction force, and Coefficient of Friction (COF), which is the ratio of the frictional force to the loading force on the disk. The wear rate of the balls is measured using Equation 3.4:

$$W = \frac{V}{F \times L} \tag{3.4}$$

Where, V is ball volume loss, F is applied load, and L is displacement length. The ball volume loss needs to be measured after each test. The following equation is used to calculate the volume loss:

$$V = \frac{\pi \times (D)^4}{64 \times (R)} \tag{3.5}$$

Where, D is wear scar diameter, and R is ball radius. The equations are in accordance with ASTM G99–17 [95].
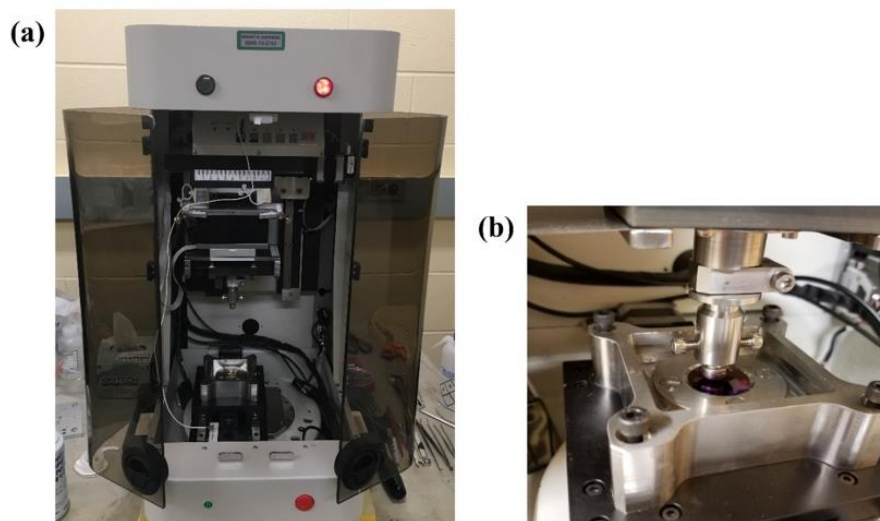
Figure 3.18. (a) The UTM and (b) the ball-on-disk configuration used in this work

3.4.12 Corrosion testing

Gamry instruments reference 600 potentiostat, located in the Department of Chemical Engineering, University of Saskatchewan, was used to evaluate the corrosion resistance of the samples. The electrochemical cell setup includes various electrodes, electrolyte, cabling, and a cell which is connected to the potentiostat, as shown in Figure 3.19. In the electrochemical cell, the specimen is used as the working electrode, a pure graphite rod as the counter electrode, and a saturated calomel electrode as the reference electrode. The potentiostat controls the voltage difference between the working and reference electrodes. The potentiostat implements this control by flowing current between the working and counter electrodes [96]. The samples with an area of $1cm^2$ were exposed to pbs solution at room temperature in accordance with ASTM G61-86 [97]. The polarization potential was measured against the standard calomel reference electrode using a scanning rate of 0.5 mV/s. Potentiodynamic polarization curve was obtained and Tafel extrapolation technique was applied to find the corrosion current density.

Figure 3.19. The electrochemical cell setup connected to the potentiostat used in this work

CHAPTER 4

GROWTH AND CHARACTERIZATION OF TANTALUM THIN FILMS ON CoCrMo ALLOY SHEETS FOR ORTHOPEDIC IMPLANT APPLICATIONS

In this chapter, growth and characterization of Ta thin films on a CoCrMo alloy are investigated for improving the surface functionality of this alloy which has been widely used to make femoral heads in artificial hip joints. In this regard, the effect of deposition parameters on the formation of different phases of Ta, and the development of adherent Ta thin films on a CoCrMo alloy are explained. This chapter is published in "Thin Solid Films" as follows:

"Growth and characterization of tantalum multilayer thin films on CoCrMo alloy for orthopedic implant applications, S. Shiri, C. Zhang, A. Odeshi, Q. Yang, Thin Solid Films 645 (2018) 405-408".

My contributions to this paper are: review of the relevant literature, design and conduct the experiments, analysis of test results and preparing the manuscripts under the supervision of Professor Qiaoqin Yang and Professor Akindele Odeshi. The manuscript was reviewed and revised by my supervisors, Professor Qiaoqin Yang and Professor Akindele Odeshi, before submission to the journal for publication. The present manuscript is a modified version of the published paper. The copyright permission is obtained and provided in the Appendix section.

Abstract

In this study, Ta thin films deposited (by magnetron sputtering) on biomedical CoCrMo alloy substrates are studied using XRD, SEM, and Rockwell C indentation tests. The results show that single phase α-Ta thin films with low adhesion forms at substrate temperature of 400 °C or above, while thin films with a mixture of α-Ta and β-Ta and a low adhesion form at substrate temperature lower than 400 °C. By applying a negative substrate bias voltage from 78 V up to 90 V, single phase β-Ta thin films is obtained at room temperature. β-Ta thin films deposited at a negative bias of 78 V is of high adhesion. Further increasing the bias voltages to 115 V, single phase α-Ta forms

on the alloy, with poor adhesion. Based on the results, a multilayered Ta thin film, β-Ta/β-Ta+α-Ta/α-Ta, with controlled structure is developed on CoCrMo alloy sheets with high adhesion, which is promising for biomedical applications.

4.1 Introduction

Ta has drawn increasing attention in recent years for orthopedic implant applications due to its high hardness and good biocompatibility [2]. However, the high cost and the difficulty in making dense Ta implants limit its applications [34, 35]. Deposition of Ta thin films on CoCrMo alloys would combine the high mechanical strength of the substrate alloy with the excellent biocompatibility of Ta film and thus the performance of the implants would be greatly improved [13, 33, 65-68]. Generally, Ta thin films exist in two crystalline structures; body-centered cubic structure (α-Ta) and tetragonal structure (β-Ta). α-Ta is ductile and tough whereas β-Ta is hard and brittle [17, 22-26].

The formation of α- and β-Ta thin films is strongly dependent on the film thickness, substrate material, and processing parameters. Researches have been done to understand the effect of processing parameters on the formation of different phases of Ta, however, the results obtained are controversial and the understanding is very limited [13, 14, 16, 19, 22, 23, 25-26, 40-64]. This is probably due to the combined effect of different parameters. Films containing a mixture of both Ta phases can be easily deposited using physical vapor deposition [13-15], but it is hard to obtain single phased α- or β-Ta thin films or to accurately control the crystal structure of Ta thin films to meet the demand of practical applications. Although α-Ta films with a thickness of between 20 nm and 600 nm have been deposited on CoCrMo alloy (ASTM F1537) substrate using magnetron sputtering by Hallman *et al*. [13], the adhesion of Ta films on the CoCrMo alloy, and consequently their functionality have not been investigated yet.

In this work, systematic investigation of the relationships between the processing parameters and the resulted film structures have been performed. Based on the results, controlled synthesis of Ta thin films on both CoCrMo alloy sheets and Si wafers with different crystal structures has been achieved. Furthermore, highly adherent α- and β-Ta thin films on CoCrMo alloy sheets to meet the demand for biomedical implant applications have been developed.

4.2 Experimental details

Ta thin films were deposited on CoCrMo alloy (ASTM F1537) sheets and silicon wafers (as a reference) using a RF magnetron sputtering system made by Plasmionique Inc. CoCrMo alloy substrates, 25 mm in diameter and 3 mm in thickness, were ground and polished using Struers automatic polisher: first ground with 320 grit size silicon carbide paper, then polished with diamond paste of 9 μm and 3 μm sequentially, and finally polished with silica suspension of 0.04 μm. After each step, samples were cleaned in distilled water. The polished samples were ultrasonically cleaned in ethanol for 15 min, and then cleaned in the deposition chamber by Ar sputtering at a substrate bias of 80 V for 5 min. Deposition was performed at a pressure of 1.33 Pa by introducing Ar gas into the chamber with a flow rate of 35 sccm and using a Ta target of 99.9% purity. The distance between the target and the sample was 35 mm and the sample stage was made to rotate at a speed of 3 rpm. Substrate temperature and substrate bias voltage were varied to deposit Ta thin films. The sputtering parameters for Ta thin film deposition are summarized in Table 4.1. The deposition time was also varied to control the film thickness. The deposition experiments were repeated for a chamber pressure of 0.80 Pa and 1.87 Pa, respectively. With the understanding of the deposition conditions for α-Ta and β-Ta phases, two-layered and multilayered gradient Ta films consisting of both α and β phases were prepared, including sample 1: β-Ta deposition for 2 h (condition e in Table 4.1) plus α-Ta deposition for 1 h (condition c in Table 4.1), sample 2: β-Ta deposition for 1 h (condition e in Table 4.1) plus α-Ta deposition for 1 h (condition c in Table 4.1), and sample 3: β-Ta deposition for 1 h (condition e Table 4.1), plus α-Ta+β-Ta deposition for 30 min (condition a in Table 4.1 with substrate temperature from room temperature to 400 °C) and α-Ta deposition for 1 h (condition c in Table 4.1).

The crystallographic structures of the synthesized thin films were investigated using Rigaku XRD instrument with Cobalt K-alpha radiation, where the XRD tube was operated at 30 kV and 20 mA, and the data were collected in Bragg–Brentano geometry with theta/2theta motion. Mechanical properties of the Ta thin films on silicon wafers (hardness and Young's modulus) were measured using nano-indentation in accordance with ISO 14577-4 standard [93], where the testing was performed with a berkovich indenter on 50 different locations at loads varying from 0.5 to 60 mN for each sample. The hardness and Young's modulus reported were the average values of those with a penetration depth of less than one tenth of the coating thickness. The thin films thickness

was measured using Jeol JSM-6010LV SEM operated at 15 kV. Conventional Rockwell C hardness testing was performed using 1470 N load to evaluate the relative adhesion strength of the films. The imprint and its surrounding area after indentation were observed using SEM.

Table 4.1. Sputtering parameters for Ta thin film deposition

Condition	Magnetron RF power (W)/ voltage (V)	Temperature (°C)	Substrate bias power (W)/ voltage (V)	Pressure (Pa)
(a)	150 W/ 200 V	Room	0	1.33
(b)	150 W/ 200 V	200	0	1.33
(c)	150 W/ 160 V	400	0	1.33
(d)	150 W/ 160 V	600	0	1.33
(e)	150 W/ 100 V	Room	30W/ 78V	1.33
(f)	150 W/ 105 V	Room	50W/ 90V	1.33
(g)	150 W/ 100 V	Room	70W/ 115V	1.33

4.3 Results and discussion

4.3.1 Effect of deposition parameters on α- and β-Ta thin films formation

Figure 4.1 presents the XRD patterns of Ta thin films on CoCrMo alloy and silicon substrates deposited at different substrate temperatures for 2 h (condition a-d in Table 4.1). The Ta thin films deposited on both substrates exhibit a mixture of α- and β-Ta phases at room temperature. With an increase in the deposition temperature of up to 400 °C, the proportion of β-Ta phase decreases and the β-Ta phase completely disappears at 400 °C. At deposition temperature of 400 °C or above, the Ta films are composed of a single α-Ta phase. Other researchers [14, 23, 98] reported that the β-Ta to α-Ta transformation temperature is above 750 °C. The results show that deposition temperature is a key factor determining the crystal structure of Ta films. High purity α-Ta thin films can be obtained at deposition temperature as low as 400 °C. This is probably due to the relative high energy of particles during sputtering deposition. It should also be noted that the Ta films deposited on silicon and CoCrMo alloy substrates under similar conditions have the same

crystal structure, indicating that substrate material has no effect on the formation of crystal structure of Ta films.

Figure 4.2 reveals the effect of substrate bias voltage on the formation of crystal structure of Ta films on CoCrMo alloy and silicon wafer substrates (deposited at condition e-g in Table 4.1). Single β-Ta film was obtained by applying a substrate bias voltage from 78 V to 90 V at room temperature for 2 h; further increasing the bias voltages to 115 V, single phased α-Ta thin films were obtained. These results suggest that low energy ion bombardment induces the formation of metastable β-Ta phase whereas high energy ion bombardment induces the formation of α-Ta phase.

Deposition experiments using condition a-g in Table 4.1 were repeated for deposition time up to 4 h and the results are the same as obtained for 2 h. The thickness of the films, as measured using SEM, is approximately 0.8 μm for 2 h deposition and 1.5 μm for 4 h deposition. In addition, all the deposition experiments were repeated for deposition pressures of 0.80, 1.33, and 1.87 Pa, respectively, on both CoCrMo alloy and silicon substrates, and the results show that deposition pressure has no effect on the phase composition of Ta thin films. However, previous researchers [13, 19, 25, 41] reported on deposition of Ta thin films with a thickness less than 600 nm and studied the effect of process parameters on the formation of Ta phases. Their results showed that the processing pressure and substrate materials affected the phase composition of Ta thin films, which are contradictory to our present results. It should be noted that the thickness of the Ta thin films in present research is between 0.7 μm and 1.5 μm which is less than 600 nm in the cited literatures.
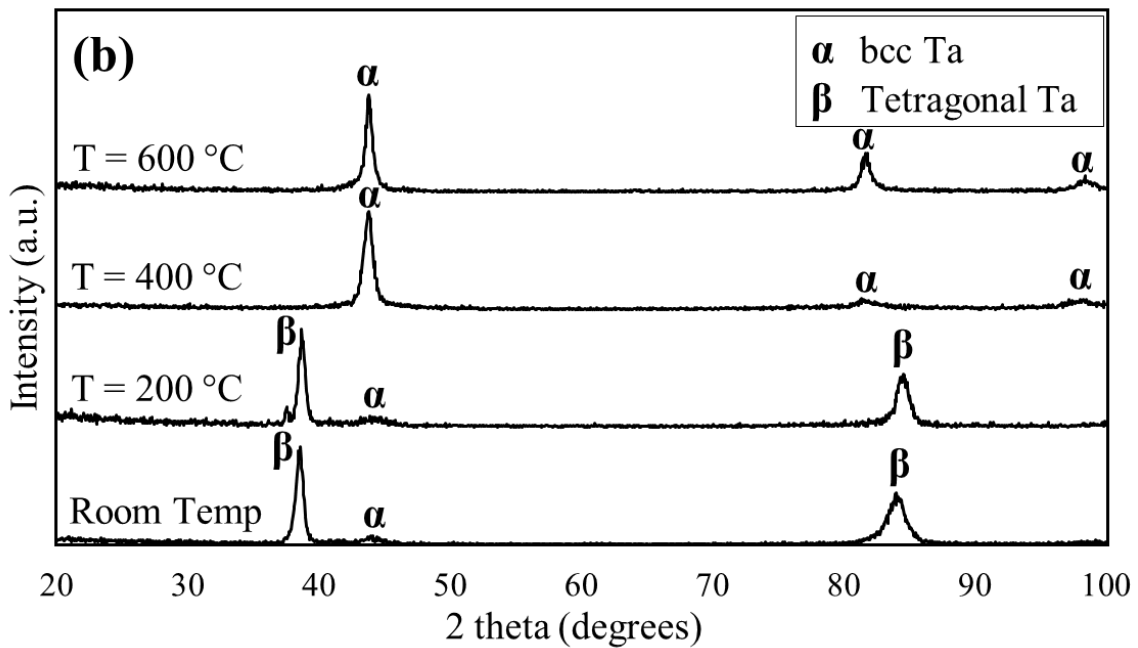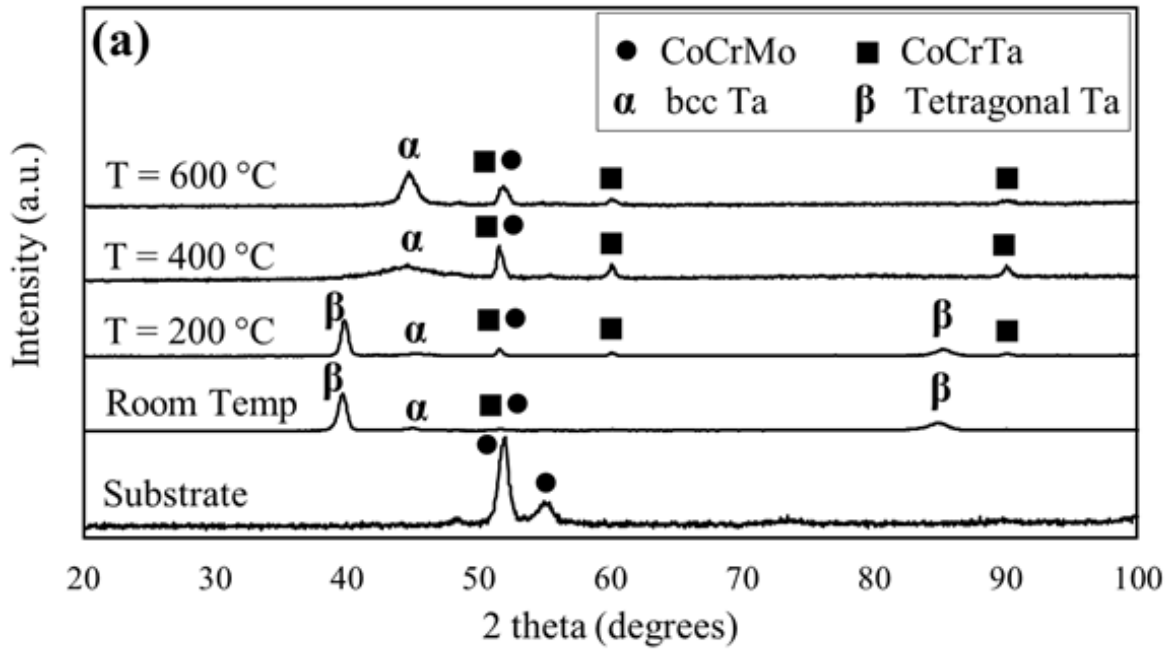
Figure 4.1. XRD patterns of Ta thin films deposited on (a) CoCrMo alloy and (b) silicon substrates at room temperature, T = 200 °C, T = 400 °C, and T = 600 °C
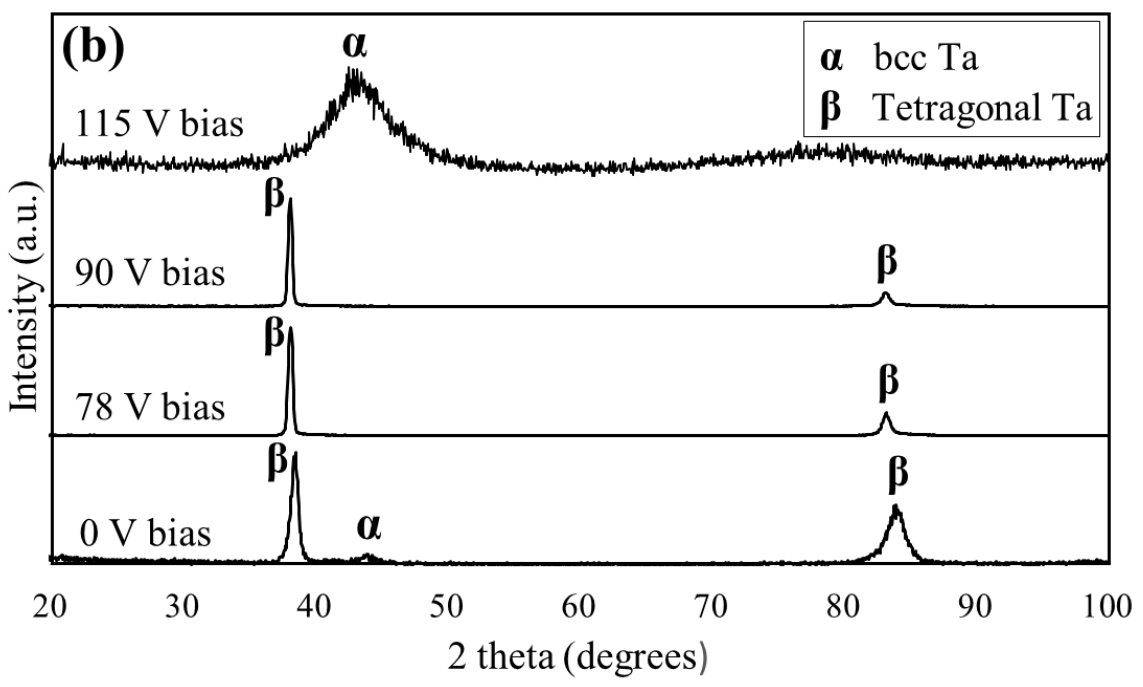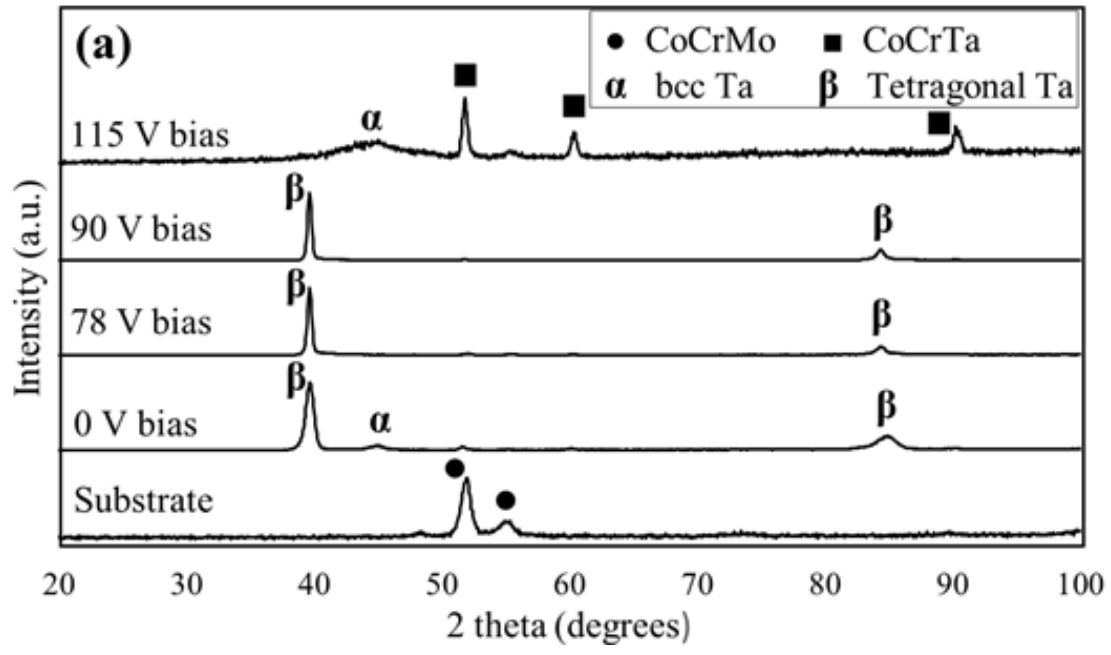
Figure 4.2. XRD patterns of Ta thin films deposited on (a) CoCrMo alloy and (b) silicon substrates at different substrate bias voltages: 0 V, 78 V, 90 V and 115 V

4.3.2 Development of adherent Ta thin film on CoCrMo alloy sheets

The Ta films deposited on CoCrMo alloy substrate at room temperature, without bias, consisting of a mixture of α- and β-Ta phases, show sever delamination. In this case, the brittleness of β-Ta and its difference in hardness and Young's modulus with α-Ta phase are probably the main reasons causing the films delamination. The hardness and Young's modulus of the α-Ta and β-Ta thin films deposited in this research are listed in Table 4.2. It can be seen that the hardness and Young's modulus of the α-Ta thin films are much lower than those of β-Ta thin films.

Table 4.2. Mechanical properties of α- and β-Ta thin films

Ta crystalline phase	Hardness ± S.D. (GPa)	Young's modulus ± S.D. (GPa)
α-Ta	14.9 ± 0.4	211 ± 8
β-Ta	18.7 ± 0.7	229 ± 14

As presented in Section 4.3.1, single phase α-Ta thin films could be deposited on CoCrMo alloy substrate under two different conditions:

- At deposition temperature of 400 °C or above (condition c in Table 4.1)
- At bias voltage of 115 V or above (condition g in Table 4.1)

The α-Ta film deposited at a bias voltage 115 V for 2 h showed sever delamination right after the deposition. In this case, the delamination is probably due to the high internal stress induced by high energy ion bombardment.

Figure 4.3 shows the SEM images of the single phase α- and β-Ta thin films on the CoCrMo alloy sheets after indentation testing. The α-Ta film deposited at 400 °C for 2 h with a thickness of approximately 0.8 μm attached well to the substrate after deposition but delaminated after indentation testing, as shown in Figure 4.3a. In this case, high thermal stress was likely induced during the cooling down from the high deposition temperature due to the large thermal expansion coefficient difference between the α-Ta phase and the CoCrMo alloy substrate. This high stress is probably the main cause of the film delamination during indentation testing.

On the contrary, the single β phase Ta thin film similar thickness (approximately 0.8 μm) synthesized on the CoCrMo alloy at condition e in Table 4.1 with a low negative bias of 78 V for 2 h, adhered well to the alloy substrate (Figure 4.3b) even after the indentation testing.
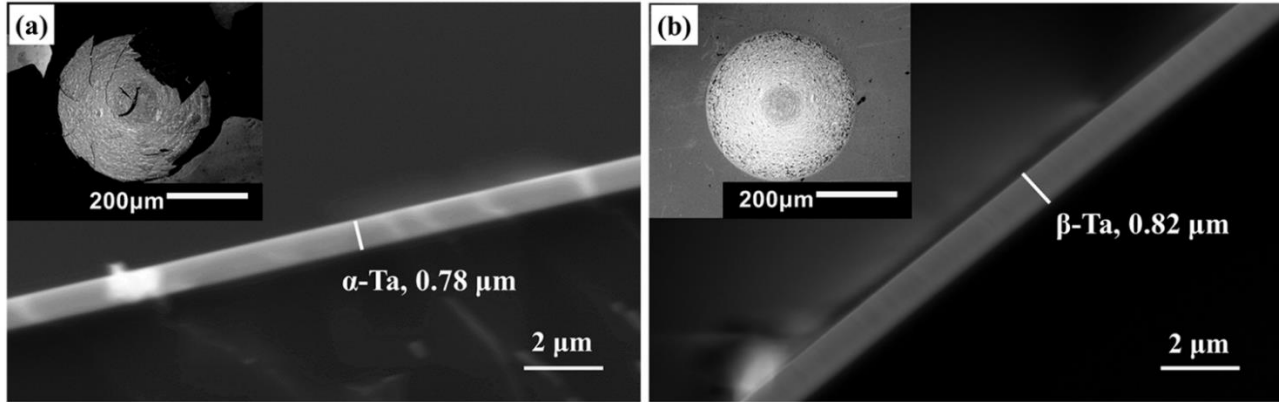
Figure 4.3. SEM images of Ta thin films (a) α-Ta film, (b) β-Ta film

In order to enhance α-Ta film adhesion and performance, thin films containing two-layers and multilayers were deposited on CoCrMo alloy sheets. Figure 4.4 illustrates the SEM images of the Ta thin films on CoCrMo alloy sheets with more than one layer after indentation testing. All the samples with more than one layer show better adhesion than single layered α-Ta film (Figure 4.3a), the two-layered film with 0.8 μm thick β-Ta layer (sample 1) shows better adhesion than the film with 0.5 μm thick β-Ta layer (sample 2), and the multilayered gradient film (sample 3) shows the best adhesion. There is no delamination observed within the indentation imprint or its surrounding area for the multilayered film, as shown in Figure 4.4c, indicating very good adhesion according to VDI 3198 standard [92].

Figure 4.5 shows the XRD pattern of the multilayered gradient Ta film (sample 3). The film consists of both β-Ta and α-Ta, indicating that the metastable β-Ta formed at low temperature did not transform to α-Ta at 400 °C. As reported previously, the β-Ta would not transform to α-Ta until it is exposed to a high temperature of 750 °C [14, 23, 98], it is reasonable that the deposition of the α-Ta top layer at 400 °C can keep the β-Ta phase in the sublayers remains stable. Based on the understanding of the effect of substrate bias voltage and temperature on the formation of α- and β-Ta phases in this study, we were able to control the crystal structure of Ta thin films. Consequently, we have successful developed adherent β-Ta and gradient Ta film with top layer of

α-Ta film on the CoCrMo alloy, which is very promising for biomedical or other protective applications.
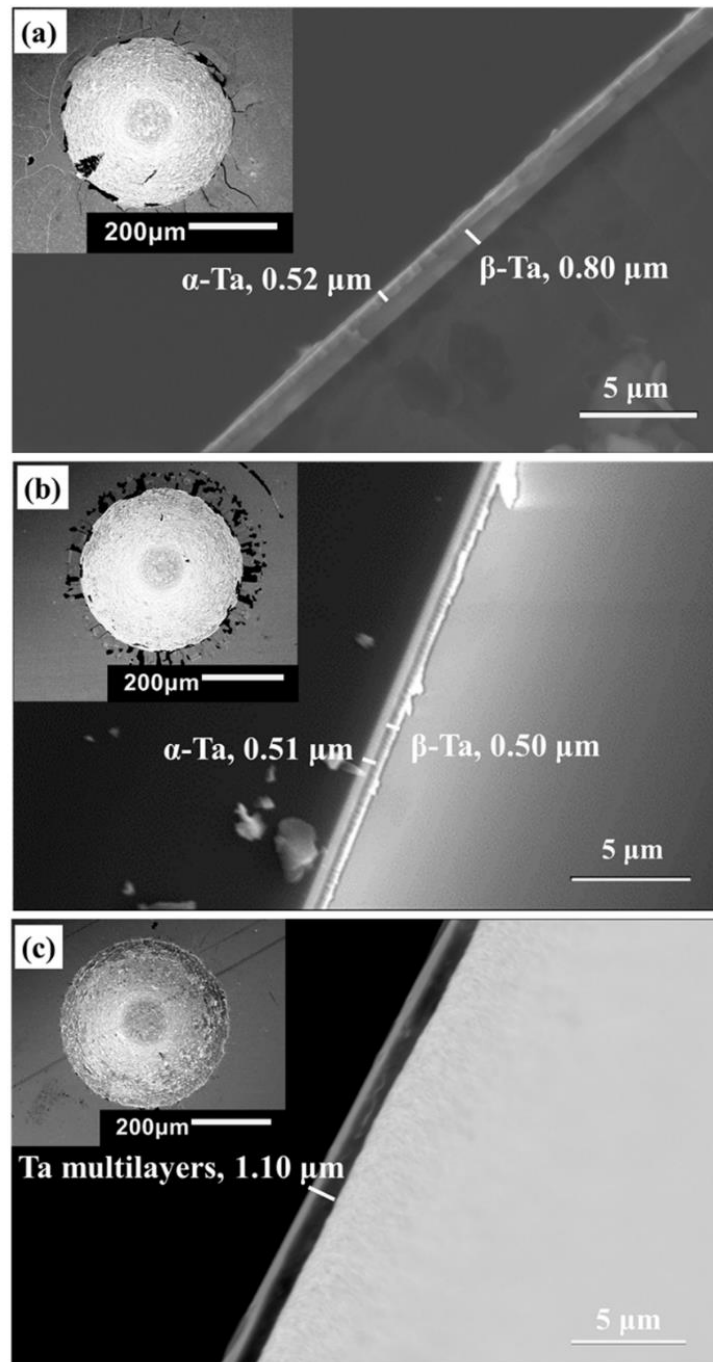
Figure 4.4. SEM images of Ta thin films (a) α-Ta film (0.5 μm thickness) deposited on β-Ta interlayer (0.8 μm thickness), (b) α-Ta film (0.5 μm thickness) deposited on β-Ta interlayer (0.5 μm thickness), and (c) multilayered structure of Ta
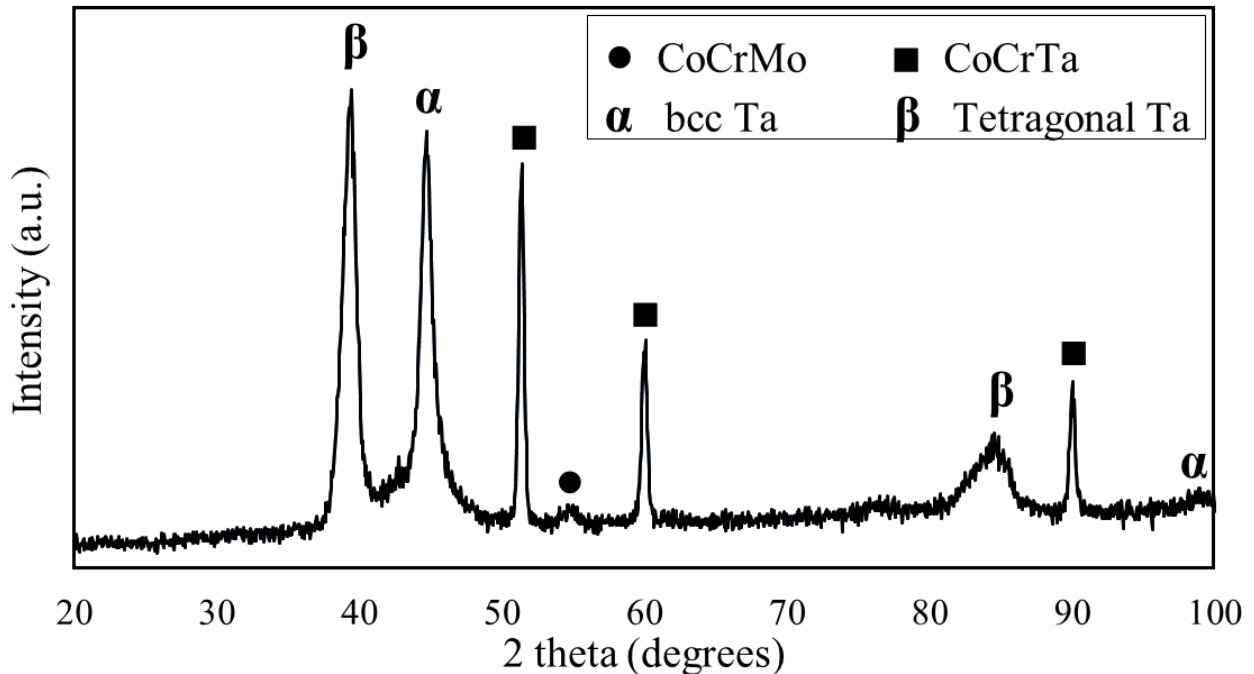
Figure 4.5. XRD pattern of the multilayered gradient Ta film (sample 3)

4.4 Conclusions

RF magnetron sputtering was used to investigate the deposition of Ta thin films on CoCrMo alloy sheets. Substrate temperature and bias voltages have been determined to be the most important factors that influence the formation of α and β phases. When the deposition temperature is 400 °C or higher, single phase α-Ta films with poor adhesion forms, whereas a mixture of α- and β-Ta thin films with poor adhesion is obtained when the deposition temperature is lower than 400 °C. By applying a substrate bias voltage from 78 V up to 90 V, single phase β-Ta films can be obtained at room temperature. In this regard, the adhesion of the thin film decreases with increasing the bias voltage. Further increasing the bias voltage to 115 V, single α-Ta phase was deposited on the alloy with a very low adhesion. Consequently, controlled synthesis of Ta thin films has been achieved. Moreover, β-Ta and α-Ta thin films with a multi Ta interlayer have been developed on the CoCrMo alloy sheets with high adhesion, overcoming one of the main barrier of using Ta thin films for biomedical applications.

CHAPTER 5
TRIBOLOGICAL AND CORROSION BEHAVIOR OF TANTALUM COATED CoCrMo ALLOY SHEETS

In order to improve the biocompatibility, corrosion, and tribological behavior of CoCrMo alloy for orthopedic implant applications, adherent α-Ta and β-Ta thin films were deposited on CoCrMo alloy sheets using magnetron sputtering as mentioned in chapter 4. In this chapter, the results of investigations on tribological and corrosion behavior of the coated and uncoated CoCrMo alloy sheets are discussed. This chapter has been submitted to "Thin Solid Films" and it is under review. My contributions to this paper are: review of the relevant literature, design and conduct the experiments, analysis of test results and preparing the manuscripts under the supervision of Professor Qiaoqin Yang and Professor Akindele Odeshi. The manuscript was reviewed and revised by my supervisors, Professor Qiaoqin Yang and Professor Akindele Odeshi, before submission to the journal for publication.

Abstract

In this study, adherent α-Ta and β-Ta thin films are deposited on CoCrMo alloy sheets using magnetron sputtering. The mechanical and surface properties of the Ta coatings are characterized using nano indentation testing, an optical profiler, and a contact angle goniometer. The tribological and corrosion behavior of the coated and uncoated CoCrMo alloy sheets are studied using a ball-on-disk tribo tester, an optical microscope, potentiostat, XPS, and SEM. The tribological testing results show that the coefficient of friction between the α- and β-Ta coating and UHMWPE balls in phosphate-buffered saline solution is 0.08 ± 0.01 and 0.09 ± 0.01, respectively, and the ball wear rate is 3.00 ± 0.02 x 10^{-5} mm^{3}N^{-1}m^{-1} and 3.25 ± 0.01 x 10^{-5} mm^{3}N^{-1}m^{-1}, respectively, which are lower than those (0.14 ± 0.01 and 8.14 ± 0.01 x 10^{-5} mm^{3}N^{-1}m^{-1}) for uncoated CoCrMo alloy sheets sliding with UHMWPE balls. The corrosion current density of the α- and β-Ta coated CoCrMo alloy sheets in phosphate-buffered saline solution was determined to be 1.4 x 10^{-8} Acm^{-2} and 9.9

x 10^{-8} Acm^{-2}, respectively, which are significantly lower than that (1.0 x 10^{-5} Acm^{-2}) for uncoated CoCrMo alloy sheet. This indicates a significant improvement on the corrosion resistance of the CoCrMo alloy as a result of coating with Ta thin films. These results suggest that applying Ta thin films on the CoCrMo alloy in both α- and β-Ta phases is desirable for orthopedic implant applications.

5.1 Introduction

One of the most widely used artificial hip joints comprises of a CoCrMo alloy femoral head articulating against an UHMWPE liner [2]. Despite the relative good durability of these combinations, human body system (patient's level of activities, body weight, and quality and quantity of body fluid) decreases the functionality of this kind of artificial hip joints. For example, the friction of these bearing surfaces in the body fluid increases the corrosion rate of the CoCrMo alloys, releases toxic Co and Cr ions. In addition, it produces metal and polymer wear debris which increases the friction and wear of the bearings, all limiting the lifetime of the implants [2, 9].

A promising approach to address the aforementioned challenges is to engineer the CoCrMo alloy surface with biocompatible and wear and corrosion resistant coatings. Deposition of a proper thin film on CoCrMo alloy would combine the good properties of the substrate materials with the excellent surface properties offered by the coating, and thus improve the performance of these bearing surfaces. Ta would be an appropriate candidate to coating CoCrMo alloy due to its excellent corrosion and mechanical resistivity, and high biocompatibility [13, 33, 65-68]. In this regard, Balagna *et al*. [33, 66, 67] deposited multilayered coating consisting of Ta carbides and metallic Ta as a top layer on a CoCrMo alloy by thermal treatment in molten salts and reported that the coating improved the wear resistant of the alloy. Moreover, Dorn *et al*. [68] investigated the corrosion behavior of CoCr alloy modular necks coated with Ta films in calf serum environment. They reported the protective effect of Ta film in mitigating the risk of corrosion and implant failure by using macrophotography alone to analyze the surface but provided no information on Ta film structure and deposition technique.

Ta thin films usually exist in two crystalline structures; body-centered cubic structure (α-Ta) and tetragonal structure (β-Ta). Previous researches claimed that α-Ta is more ductile and tougher than β-Ta and more desirable for orthopedic implants, which are subjected to mechanical stress and

47

wear [13, 26]. However, obtaining adherent single phased α-Ta thin film on the CoCrMo alloy is difficult as mentioned in Chapter 4. Therefore, no research results have been reported on its potential for orthopedic implant applications. Although Hallmann *et al*. [13] reported the deposition of α-Ta thin films on a CoCrMo alloy using magnetron sputtering, no information on the adhesion and other properties of the Ta thin film was provided. We investigated the formation of α- and β-Ta thin films on CoCrMo alloy sheets in Chapter 4. The results showed that β-Ta thin film with good adhesion could be achieved on CoCrMo alloy sheets by biasing the substrate and α-Ta thin films with good adhesion could be achieved by applying a gradient Ta interlayer.

In the present work, the tribological and corrosion behavior of CoCrMo alloy sheets coated with β-Ta and α-Ta thin films has been further investigated and the results are compared with the uncoated alloy sheets for the purpose of evaluating their potential to meet the demand for orthopedic implant applications.

5.2 Experimental details

Polished circular CoCrMo alloy (ASTM F1537) sheets with a thickness of 3 mm and a diameter of 25 mm were used as substrates and Ta thin film deposition was carried out using RF magnetron sputtering. Ta target with a purity of 99.9 % and a diameter of 51 mm was used for the Ta film deposition. Target and sample distance was 35 mm. After the alloy substrates were put into the substrate holder, the chamber was pumped to a pressure of 1.33 Pa. Ar gas with a purity of 99.99% was then introduced into the chamber with a flow rate of 35 sccm. The deposition pressure was kept at 1.33 Pa and RF power for sputtering was kept at 150 W. β-Ta thin film samples were deposited at room temperature by applying a negative bias of 78 V onto the substrate holder and α-Ta thin film samples were prepared through three steps: (1) a β-Ta layer of approximately 0.3 μm by applying a negative bias of 78 V at room temperature; (2) a layer of approximately 0.3 μm with a mixture of β-Ta and α-Ta by increasing the substrate temperature from room temperature to 400 °C gradually without biasing; and (3) an α-Ta layer of 0.5 μm by keeping the substrate holder at 400 °C without biasing. The more detailed preparation procedure for the substrates and the Ta thin films is explained in Chapter 4. Figure 5.1 shows the XRD patterns of β-Ta, α-Ta, and α-Ta thin films with a gradient Ta interlayer (β-Ta plus a mixture of β-Ta and α-Ta) on CoCrMo alloy sheets. The thickness of the β-Ta thin films is approximately 0.8 μm and the α-Ta thin films

are composed of a gradient interlayer of approximately 0.6 μm and an α-Ta top layer of approximately 0.5 μm.

Nanoindentation tester was used to measure the hardness and Young's modulus of the samples, where the testing was performed with a berkovich indenter on 50 different locations at loads varying from 0.5 to 60 mN for each sample in accordance with ISO 14577-4 standard [93]. Zygo optical profiler was used to measure the surface roughness in terms of Ra arithmetical mean roughness. Contact angle goniometer (PG-X pocket goniometer) was used to characterize the surface wettability using pbs solution, a simulated body fluid.

The tribological behavior of the Ta-coated and uncoated CoCrMo alloy sheets was investigated using a ball-on-disk tribo tester equipped in a UMT manufactured by CETR Inc., where UHMWPE ball was sliding on the Ta-coated and uncoated CoCrMo alloy sheets by applying a 10 N load with a 2.5 mm displacement length and a linear speed of 5 mm/s for 10,000 cycles in pbs solution at room temperature in accordance with ISO 14242-1 standard [94]. The COF was recorded during the sliding. After the testing, the wear of the balls was observed using OLYMPUS BX41M-LED optical microscope, and measured in accordance with ASTM G99–17 [95].

The potentiondynamic polarization curves of the Ta-coated and uncoated CoCrMo alloy sheets were obtained using Gamry instruments reference 600 potentiostat, where samples with an area of 1 cm^2 were exposed to pbs solution (Sigma P-38135, pH: 7.4) at room temperature in accordance with ASTM G61-86 [97]. The polarization potential was measured against the standard calomel reference electrode using a scanning rate of 0.5 mV/s. Tafel extrapolation technique was applied to find the corrosion current density, an important indicator of corrosion rate. Two samples of each coated and uncoated CoCrMo alloy sheets were tested to ensure reproducibility of the results. AIXS SUPRA XPS with aluminum K-alpha radiation as the excitation source was used to analyze the chemical composition and state of the thin film surfaces before and after corrosion to understand the corrosion mechanism. Depth profiling chemical state of Ta was done using XPS combined by Ar sputtering, with settings of 4 keV energy of Ar ions. The surface morphology of the samples before and after corrosion testing was observed using SU8010 SEM operated at 5 kV.
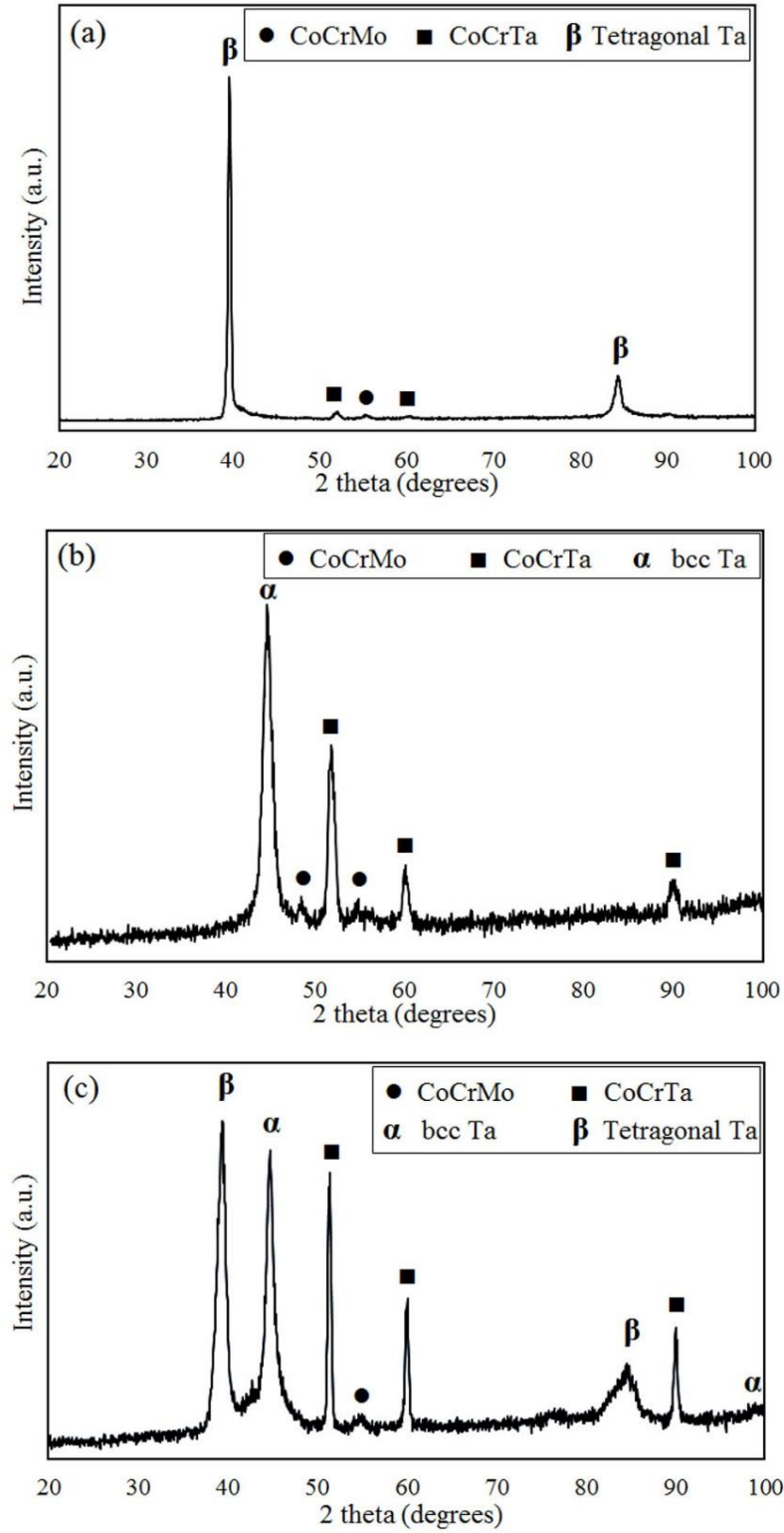
Figure 5.1. XRD patterns of (a) β-Ta, (b) α-Ta, and (c) α-Ta thin films with a gradient Ta interlayer on CoCrMo alloy sheets

5.3 Results and discussion

5.3.1 Surface properties

The hardness, Young's modulus, roughness, and contact angle of the uncoated and α- and β-Ta coated CoCrMo alloy sheets are presented in Table 5.1. The hardness of α-Ta with body-centered cubic structure is lower than that of the β-Ta with tetragonal structure, but both the Ta coatings show much higher hardness than the substrate.

Figure 5.2 shows optical profiler micrograph of the uncoated and α- and β-Ta coated CoCrMo alloy sheets. The roughness of the coated samples is lower than that of the uncoated samples, indicating that the deposition processing decreases the surface roughness. The deposition of β-Ta thin films was achieved by applying a negative bias and the deposition of α-Ta thin films was carried out at a relatively high substrate temperature (400 °C). Either biasing or deposition at high temperature increases the mobility and lateral diffusion of the Ta atoms and provides a uniform surface with lower roughness [99].

The wettability of the α- and β-Ta coated samples is similar, both show significantly lower contact angle, and therefore higher wettability than the uncoated alloy samples (Figure 5.3). Low contact angle of Ta coatings indicates a high surface energy of the materials, which would lead to better cell attachment [34, 100, 101] for the development and maintenance of the functionality of tissues [102].

Table 5.1. Surface properties of uncoated and Ta-coated CoCrMo alloy samples

	Hardness ± S.D. (GPa)	Young's modulus ± S.D. (GPa)	Surface roughness (nm)	Contact angle in pbs solution (degree)
Untreated CoCrMo alloy	5.6 ± 0.2	285 ± 20	22 ± 2	80 ± 1
α-Ta coated CoCrMo alloy	14.6 ± 0.9	235 ± 16	16 ± 2	64 ± 1
β-Ta coated CoCrMo alloy	17.1 ± 0.9	261 ± 27	16 ± 2	62 ± 1
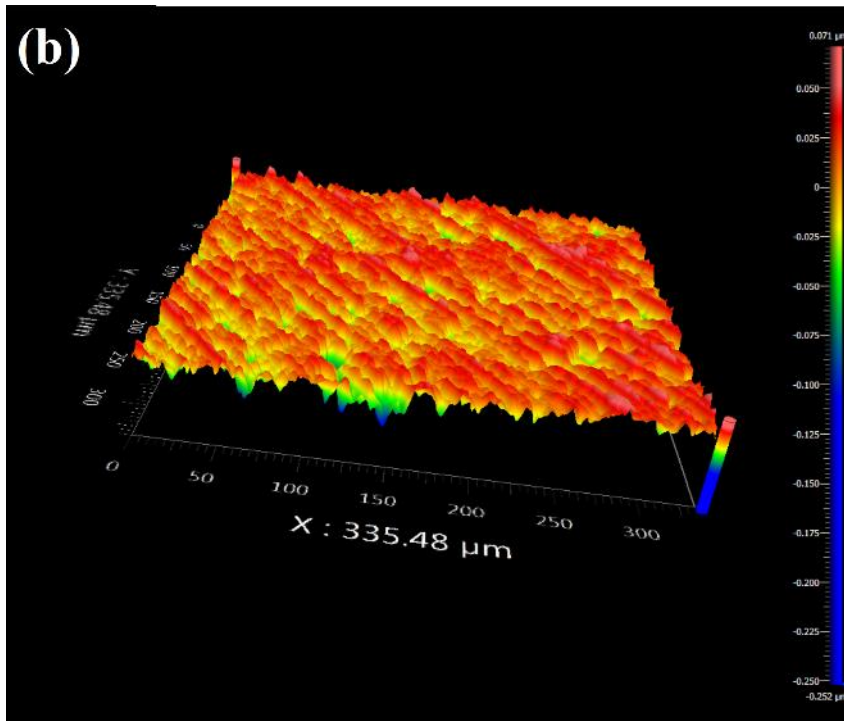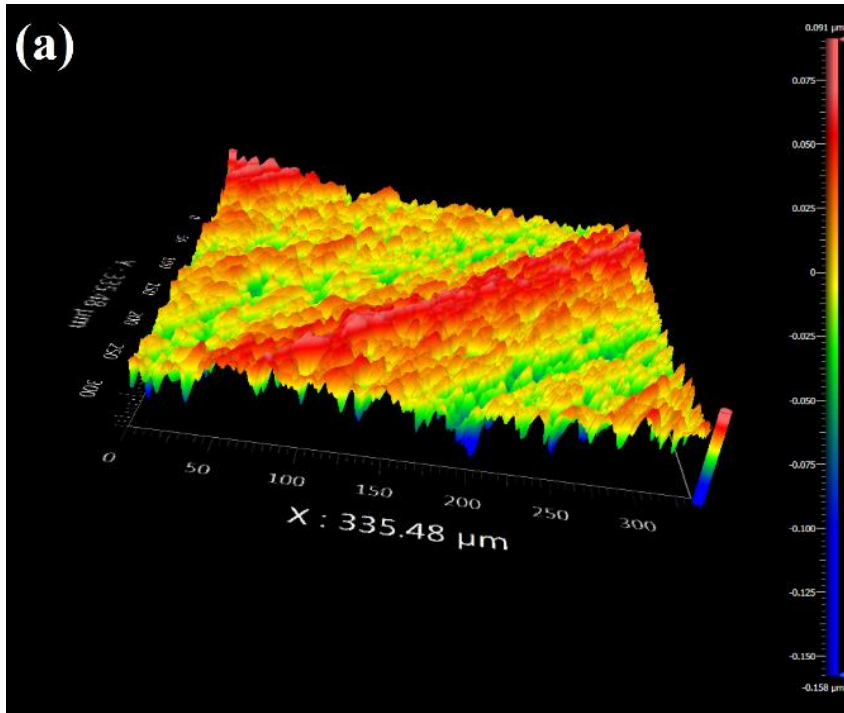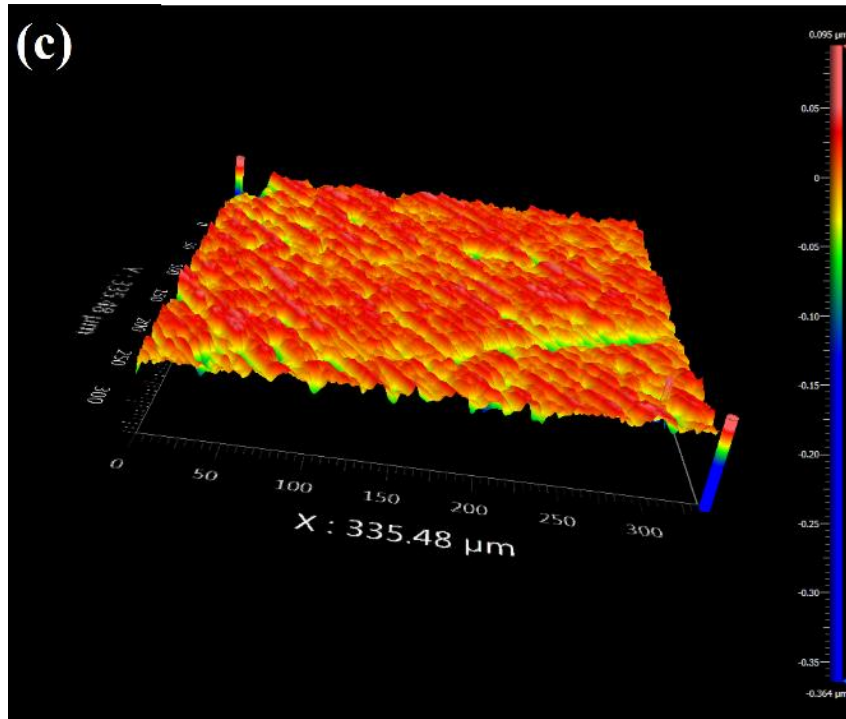
Figure 5.2. Optical profiler micrograph of the (a) uncoated, (b) α-Ta coated, and (c) β-Ta coated CoCrMo alloy sheets
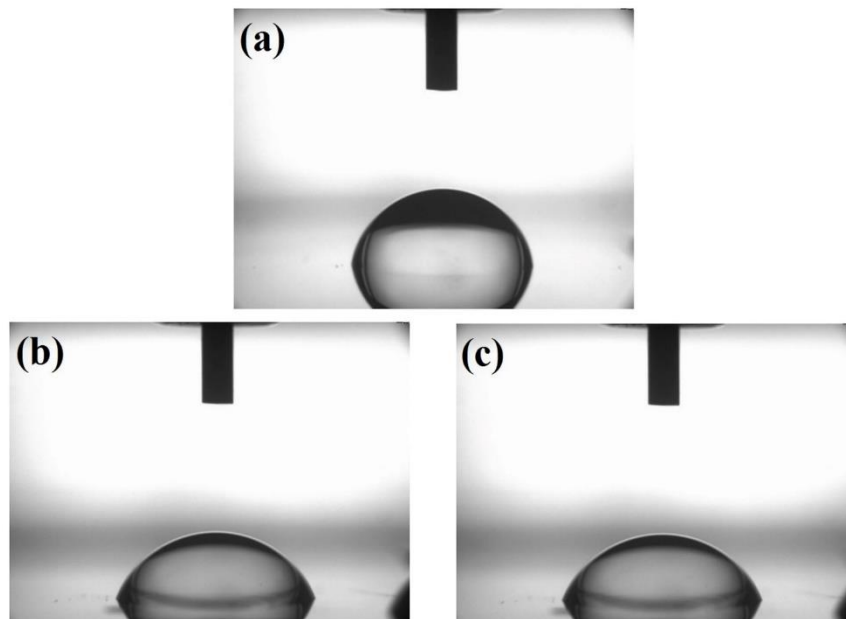
Figure 5.3. Wettability of the (a) uncoated CoCrMo alloy, (b) α-Ta, and (c) β-Ta coated CoCrMo alloy sheets in pbs solution

5.3.2 Tribological behavior

After the tribological testing, no wear was observed for the coated and uncoated CoCrMo alloy sheets, indicating high wear resistance of the samples against UHMWPE. However, wear of the UHMWPE balls shows that the wear mechanism of these pairs is abrasive wear of the balls as shown in Figure 5.4. In this case, only the wear rate of UHMWPE balls and the COF are presented in Table 5.2. We can see that the COF and UHMWPE ball wear rate for the α-Ta coated samples are slightly lower than those for the β-Ta coated samples and both are lower than those for the uncoated CoCrMo alloy samples. As one of the major failure mechanism for Metal-on-Polymer artificial joints is the wear of UHMWPE, the fact that the Ta coating reduce the wear rate of UHMWPE is favorable for joint applications. This improved tribological performance of Ta coated samples is probably a result of the improved surface properties presented in Table 5.1. Firstly, the Ta coated CoCrMo alloy sheets show much higher wettability in pbs solution. This better wettability in α- and β-Ta coated CoCrMo alloy sheets increases the lubrication, decreases the COF, and subsequently reduces the wear rate of the UHMWPE balls. Secondly, Ta coating decreases the surface roughness of the CoCrMo alloy sheets. As lowering roughness usually decreases COF and the wear rate of the counterpart at the beginning of wear testing [103], the lower roughness of the coated CoCrMo alloy sheets might partially account for the lower COF and UHMWPE ball wear rate. The slight difference in COF and wear resistance between the α- and β-Ta coated CoCrMo alloy sheets is probably due to the difference between their mechanical properties. As Table 5.1 shows, the hardness of the α-Ta is lower than the β-Ta, as a result, COF and UHMWPE wear rate of the α-Ta is little bit lower than the β-Ta. Similarly, Balagna *et al*. [33, 66] have reported that hcp Ta coatings (with TaC/Ta_2C interlayer) on a CoCrMo alloy improved the wear resistance of the alloy when sliding against alumina ball.
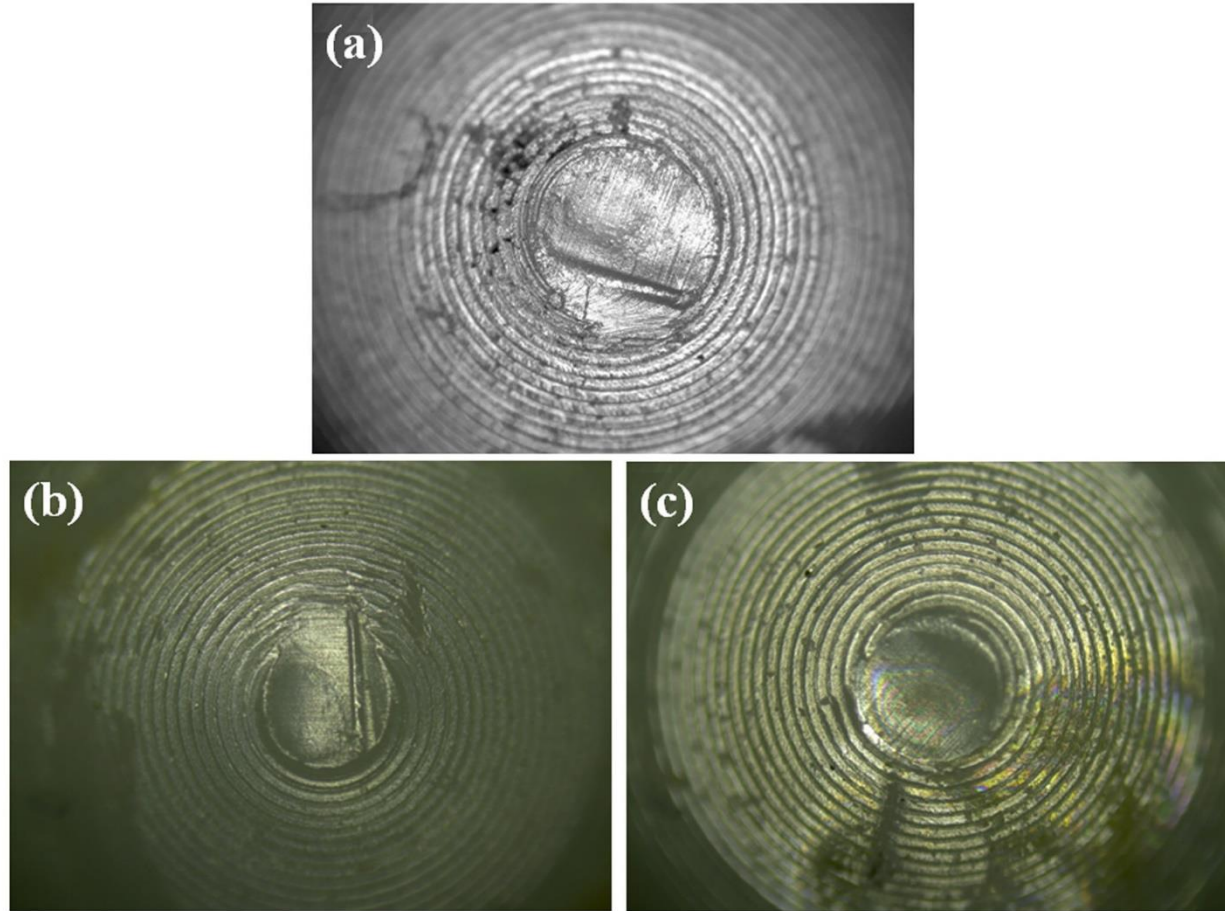
Figure 5.4. Wear of the UHMWPE balls for (a) uncoated CoCrMo alloy, (b) α-Ta, and (c) β-Ta coated CoCrMo alloy sheets after the tribology testing

Table 5.2. Tribological properties of uncoated and Ta-coated CoCrMo alloy samples

	COF ± S.D.	UHMWPE ball wear rate ± S.D. ($mm^3N^{-1}m^{-1}$)
Untreated CoCrMo alloy	0.14 ± 0.01	8.14 ± 0.01 x 10^{-5}
α-Ta coated CoCrMo alloy	0.08 ± 0.01	3.00 ± 0.02 x 10^{-5}
β-Ta coated CoCrMo alloy	0.09 ± 0.01	3.25 ± 0.01 x 10^{-5}

5.3.3 Corrosion behavior

Figure 5.5 shows the potentiodynamic polarization curves of uncoated and α- and β-Ta coated CoCrMo alloy sheets during corrosion testing in a pbs solution. Applying Tafel extrapolation technique to the polarization curves, we can get the corrosion current density (i_{corr}), an important indicator of corrosion rate. The i_{corr} for α- and β-Ta coated CoCrMo alloy sheets is determined to be 1.4×10^{-8} Acm^{-2} and 9.9×10^{-8} Acm^{-2}, respectively, which are significantly lower than that, 1.0×10^{-5} Acm^{-2}, for the uncoated CoCrMo alloy sheet. This indicates a significant improvement in corrosion resistance of the CoCrMo alloy as a result of applying Ta coatings. Comparing Ta coatings with different crystal structure, α-Ta thin films show a little bit higher corrosion resistance. Nevertheless, both the Ta coatings have demonstrated to be able to reduce the risk of CoCrMo implants' failure due to corrosion. The adhesion, thickness and density of the coatings can be a factor to decrease the corrosion current density of the samples, however, the main factor would be related to the reactivity or stability of the oxide film on the surface which is investigated further here [104-108].

A typical polarization curve can be divided to two parts: anodic polarization part, referring to the dissolution of the tested material, and cathodic polarization part, indicating hydrogen evolution. In the case of α- and β-Ta coated CoCrMo alloy sheets, the anodic polarization part is directed to a passivation region at 3.6×10^{-8} Acm^{-2} and 5.8×10^{-8} Acm^{-2} corrosion current density, respectively. This stable passivation region suggests the existence of a uniform Ta oxide film on the surface, which acts as a barrier to corrosion, and subsequently improves the corrosion resistance.
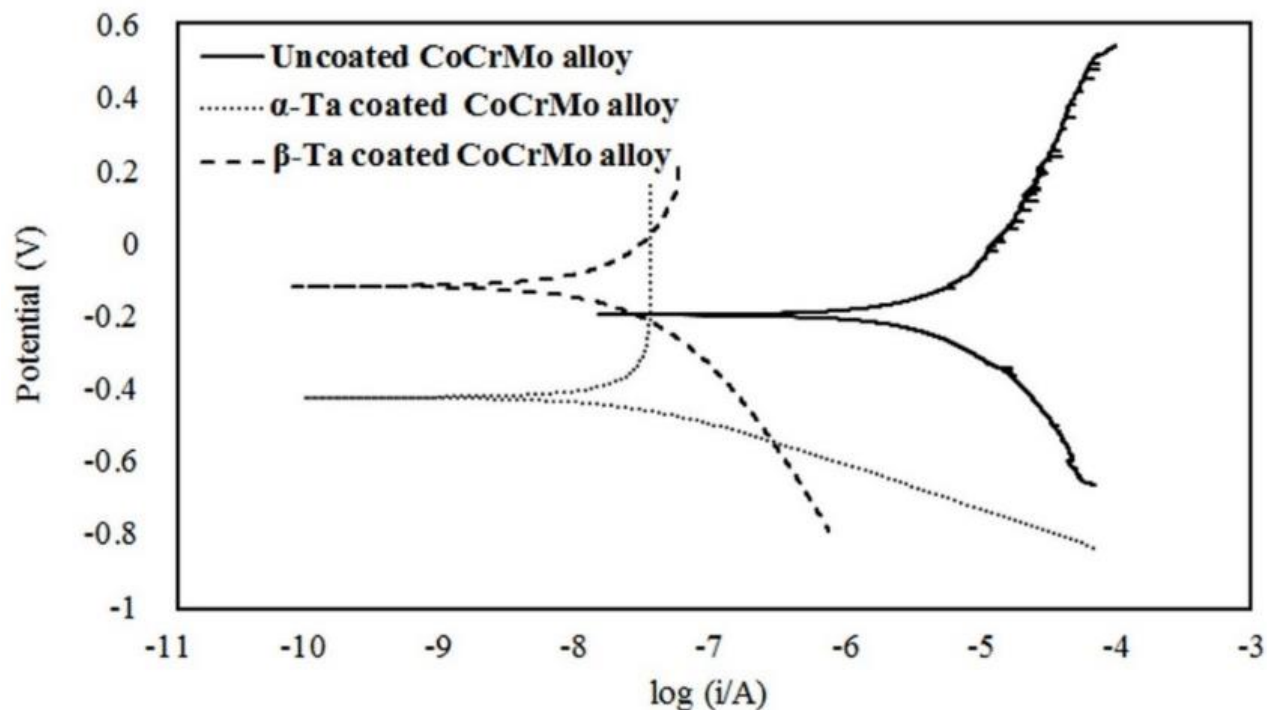
Figure 5.5. Potentiodynamic polarization curves of the uncoated CoCrMo alloy and the α- and β-Ta coated CoCrMo alloy sheets in pbs solution

Figure 5.6 shows Ta 4f fine XPS spectra of the α- and β-Ta surface before and after the corrosion testing. The spectra of the surface (without Ar etching) before corrosion testing show four peaks (two doublets). The two peaks at lower binding energies (approximately 22 eV and 24 eV) can be assigned to metallic Ta 4f7/2 and 4f5/2 and the two peaks at higher binding energies (approximately 26 eV and 28 eV) are corresponding to Ta 4f7/2 and 4f5/2 in Ta_2O_5 compound [104, 105, 107], indicating that part of the Ta thin film surface was oxidized to Ta_2O_5 when exposed to air. For the samples after the corrosion testing, the XPS measurements were done with sequences of etching steps (each step with Ar etching for 2 seconds). The spectra without Ar etching show no metallic Ta peaks for both the Ta thin films, indicating that the metallic Ta on the surface was oxidized to form Ta_2O_5 during the corrosion testing. After 2 seconds Ar ion etching, metallic Ta appears for β-Ta thin film whereas only oxidized peaks presence for α-Ta thin film. After 4 seconds etching, α-Ta thin film also shows metallic Ta peaks beside Ta_2O_5 peaks. With increasing the etching time to 12 seconds, α-Ta thin film still shows peaks of both Ta_2O_5 and metallic Ta, whereas oxidized peaks completely disappear for β-Ta thin film. Even after 20

57

seconds etching, Ta₂O₅ still exists in α-Ta thin film. Those XPS results confirm the formation of a Ta₂O₅ layer on the surfaces of both Ta thin films during corrosion testing and the Ta₂O₅ layer formed on the α-Ta thin film is thicker than the one on the β-Ta thin film. Therefore, with similar corrosion mechanism, it is reasonable that the corrosion resistance of the α-Ta thin film is a little higher than β-Ta.
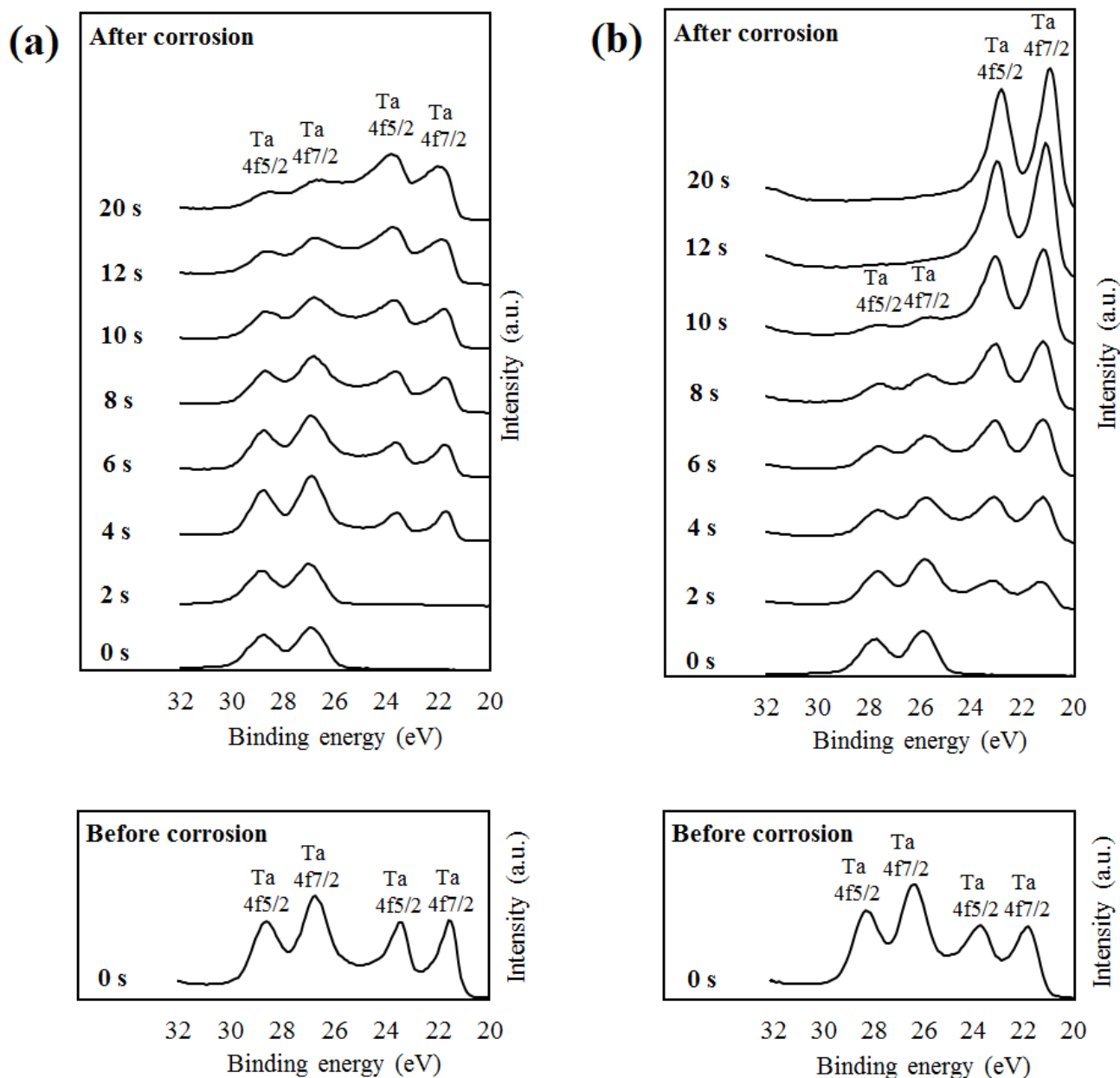
Figure 5.6. Ta 4f fine XPS spectra of the (a) α-Ta and (b) β-Ta coated CoCrMo alloy surfaces before and after the corrosion testing

The SEM surface morphologies of the α- and β-Ta coated CoCrMo alloy sheets before and after the corrosion testing are illustrated in Figure 5.7. Before the corrosion, the samples show relatively smooth surfaces with some scratches generated during the sample's preparation, and also some porosities, but at high magnification, the surface shows a dense and continuous films with small grains. However, after the corrosion test no corrosion observes at the sample's surfaces, and in most of the regions the coating is intact. Based on the observations, we can contribute the superior corrosion resistance of the Ta coatings to the high stability and passivity of the Ta oxide layer on the surface.

In summary, both the α- and β-Ta coatings decrease the roughness and increase the hardness and wettability of CoCrMo alloys, and thus decrease the COF and wear rate of the counter balls when sliding against UHMWPE ball in pbs solution. In addition, the Ta coatings significantly increase the corrosion resistance of the CoCrMo alloy in pbs solution. With similar corrosion mechanism, the corrosion resistance of the α-Ta thin film is higher than β-Ta. These results suggest that development of adherent Ta coatings on the CoCrMo alloy are very promising for orthopedic implant applications.
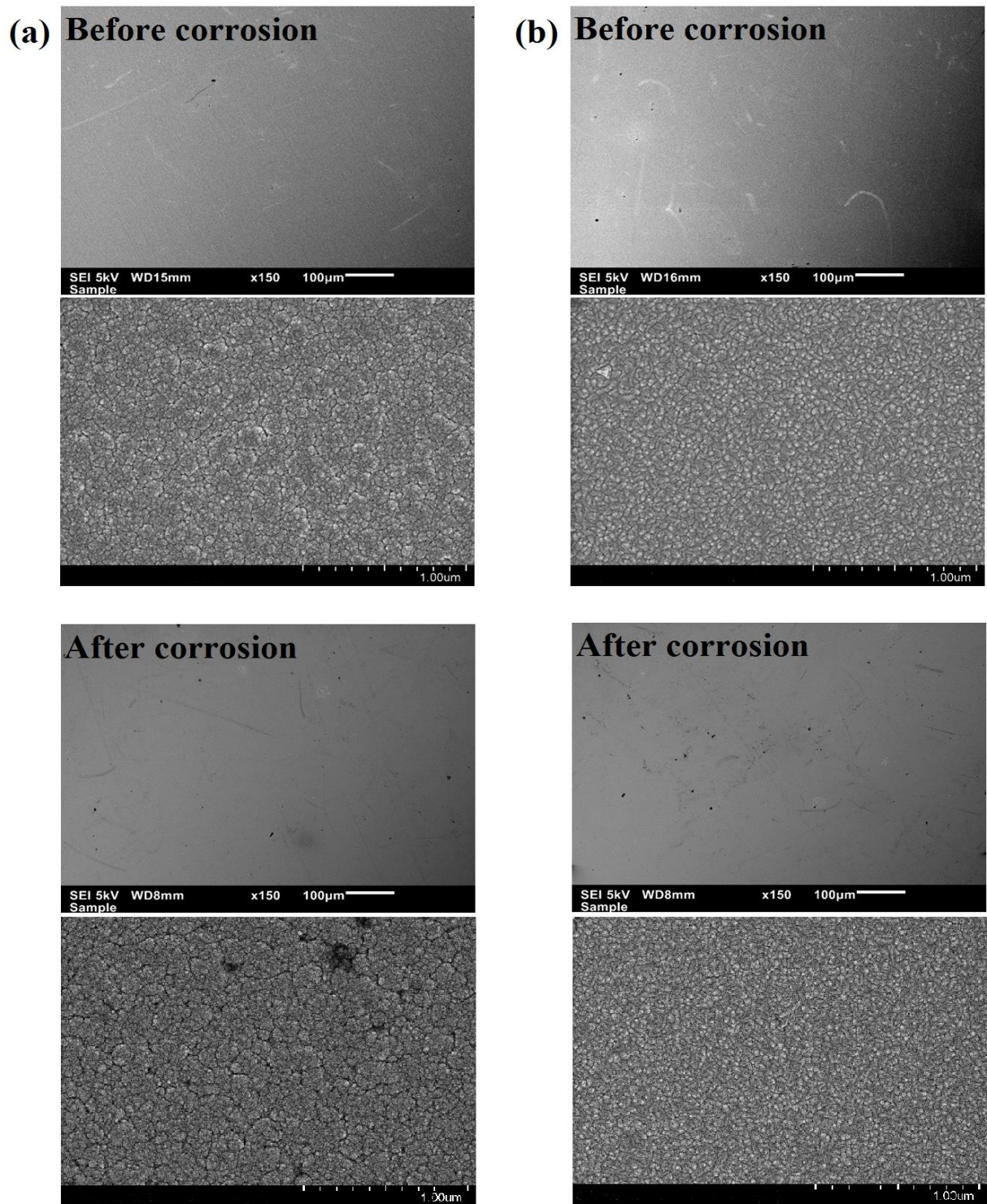
Figure 5.7. SEM images of the (a) α-Ta and (b) β-Ta coated CoCrMo alloy surfaces before and after the corrosion testing

5.4 Conclusions

Adherent β-Ta and α-Ta thin films were developed on CoCrMo alloy sheets for tribological and corrosion investigation. Sliding testing with UHMWPE ball in pbs solution show that both the coatings decrease the COF and wear rate of the balls, which is probably due to the better wettability and lower roughness of the Ta thin films. The corrosion testing results show that both α- and β-Ta coatings can significantly improve the corrosion resistance of the CoCrMo alloy in pbs solution and the superior corrosion resistance of the coatings can be attributed to the formation of a uniform dense Ta_2O_5 film on the surface during the corrosion testing. In this regard, α-Ta shows even higher corrosion resistance due to the formation of a thicker Ta_2O_5 on the surface. Those results suggest that Ta thin films (β-Ta or α-Ta) can be applied to improve corrosion and wear behavior of the CoCrMo alloy, and possibly the performance of the alloy in orthopedic implant applications.

CHAPTER 6

fcc TANTALUM THIN FILMS DEPOSITED BY MAGNETRON SPUTTERING

Tantalum exists in body-centered cubic (α phase), tetragonal (β phase), and face-centered cubic (fcc) crystal structures. The β phase is a metastable structure formed in thin films and is often mixed with the α phase. The fcc phase has only previously been reported as dispersed fine grains embedded in α or β phase. The present chapter reports the structure, formation mechanism, and stability of fcc Ta thin films. This chapter has been submitted to "Surface and Coatings Technology" and it is under review. My contributions to this paper are: review of the relevant literature, design and conduct the experiments, analysis of the test results and preparing the manuscripts under the supervision of Professor Qiaoqin Yang and Professor Akindele Odeshi. The manuscript was reviewed and revised by my supervisors, Professor Qiaoqin Yang and Professor Akindele Odeshi, before submission to the journal for publication.

Abstract

In this study, Ta thin films are deposited on silicon substrates by magnetron sputtering. A mixture of α and β phases is observed in the films when the deposition temperature is lower than 400 °C. The β phase content decreases gradually with the increase in deposition temperature, and completely disappears at 400 °C. It is interesting that when the deposition temperature reaches 500 °C, both α and β phases disappear, and Ta films appears as fcc structure. The structure and the stabilization of the fcc Ta thin films are further investigated using XRD, SEM, XPS, and XAS, and the results are presented in the present chapter. This new finding would open new research and application directions for Ta materials.

6.1 Introduction

Tantalum has been used in many areas including microelectronics, biomedical implants, and surgical instruments due to their excellent corrosion resistance, high ductility, desirable electrical

properties, and refractory nature [2, 18, 109]. Ta thin films generally exist in bcc crystal structure (α phase), although it can also exist in two other allotropic forms with tetragonal (β phase) and fcc crystal structures. Deposition techniques and deposition parameters, film thickness, and substrate material have influence on the formation of different Ta phases. Researchers have investigated the effect of processing parameters on the formation of α- and β-Ta phases [13, 14, 16, 19, 22, 23, 25, 26, 40-64], however, the results are diverse due to the combined effect of different parameters.

Only six journal articles have reported the formation of fcc Ta under special conditions [27-32]. The fcc Ta has been reported as dispersed fine grains embedded in α and/or β Ta thin films [27-31], or in bulk samples of heavily deformed Ta [32].

Ta with fcc structure was firstly reported by Denbigh *et al*. in 1966 [27]. They found epitaxial growth of fcc structure in ultrathin (< 10 nm) Ta films deposited on MgO substrate by electron beam evaporation below 400 °C, which changed to dispersed fcc fine grains of Ta as the Ta film thickness increased to 25 nm and fcc Ta grains disappeared when the thickness became greater than 25 nm. One year later, Chopra *et al*. [28] reported the nucleation of fcc Ta in Ta films of 50 nm deposited by sputtering at temperatures below 400 °C. They attributed the nucleation and stabilization of fcc Ta to the relatively higher kinetic energy and higher electrostatic charges in the sputtering technique compared to evaporation. In 1968, Marcus *et al*. [29] further reported that fcc Ta structure could only exist in very thin (10 nm or thinner) Ta films deposited using electron beam evaporation technique due to the large contribution of surface forces and the incorporation of surface impurities. Later, the study of Schrey *et al*. in 1970 [30] confirmed the fcc Ta formation in very thin films (within thickness less than 20 nm) deposited by radio frequency sputtering at 325 °C, consistent with the previous reports. Recently, Janish et.al. [31] tried a different approach in investigating the fcc Ta formation. They showed nucleation of fcc Ta in amorphous structure of Ta thin films of 20 nm thickness when annealed at 450 °C. In all aforementioned published works, only a small amount of very fine fcc grains was found in the Ta films. Furthermore, in all the reported cases, the fcc structure of Ta disappeared when the film thickness or substrate temperature increased beyond a value. In addition, dispersed nanosized fcc Ta grains were found in heavily deformed bulk bcc Ta samples [32]. Nevertheless, up to now, only a small amount of nanosized fcc Ta grains have been obtained and observed using only TEM, which were embedded in other phases of Ta (α phase or β phase or their mixture). As such, the processing conditions and structural

information of fcc Ta are very limited, and the properties of fcc Ta could not be measured. Here we report on the synthesis of fcc Ta thin films of 2.0 μm thickness and their X-Ray diffraction data.

6.2 Experimental details

The Ta thin films were deposited on (100) silicon wafers, α-Ta coated silicon wafers, and Co alloy (ASTM F1537) sheets using a magnetron sputtering deposition system made by Plasmionique Inc. Mirror polished substrates were ultrasonically cleaned in ethanol for 15 min. Deposition was performed at a pressure of 1.33 Pa using ultra high pure Ar gas flowing at a rate of 35 sccm, and 99.9% purity Ta target. The mean voltage of the target ranged from 175 V to 200 V. Different substrate temperatures (room temperature, 200, 400, 500, 600 °C) and different substrate bias voltages were applied to deposit Ta thin films.

In order to understand the effect of impurities on the formation of Ta thin film structure, nitrogen (supplied by gas source), oxygen (supplied by gas source), and carbon (supplied by graphite target and methane (CH_4) sources) were introduced into the deposition chamber during the Ta film deposition as shown in Table 6.1, while keeping other deposition parameters the same as aforementioned. The deposition time for all the experiments was 2 h. The thicknesses of the deposited films were measured using Jeol JSM-6010LV SEM. The crystallographic structure of the as-deposited thin films was investigated using Rigaku XRD instrument with Cobalt K-alpha radiation (Co-Kα), and grazing XRD using Synchrotron VESPERS beamline with 15 keV energy at the CLS. The chemical composition of the thin films was investigated using XPS (model: AIXS SUPRA) with Al Kα radiation as the excitation source at the SSSC. Each XPS measurement consists of sequences of etching steps, using Ar gun 4 keV for 120 s in each etching step. CasaXPS software was used to analyze the obtained XPS data. The chemistry (oxidation state) of Ta thin films was investigated using X-ray absorption near edge structure (XANES) data from the Ta L3 edge, measured at XAS end station of HXMA beamline at the CLS. The XAS measurement for thin films was configured to the grazing incidence setup and the data collection was in fluorescence mode. Athena software was used to analyze the data. In order to understand the thermal stability of the fcc Ta thin films, the coated silicon samples were annealed at temperatures ranging from 700 °C to 900 °C for one hour using a GSL-1500X furnace. The heating rate of the furnace was

10 °C/min and the cooling was done with the furnace until room temperature. The whole processing was performed with Argon gas flowing under a pressure of 0.08 MPa.

Table 6.1. Deposition parameters for introducing nitrogen, carbon, and oxygen into the chamber

Condition	Gas flow rate	Temperature
1	N/ (N + Ar): 12-22%	Room Temp
		500-600 °C
2	O/ (O + Ar): 12-22%	Room Temp
		500-600 °C
3	CH_4/ (CH_4 + Ar): 12-22%	Room Temp
		500-600 °C
4	Graphite target: 10/35 W/V	Room Temp
		500-600 °C
5	Graphite target: 50/120 W/V	Room Temp
		500-600 °C

6.3 Results and discussion

Figure 6.1a and 6.1b show the XRD patterns of Ta thin films deposited on silicon substrate at different substrate temperatures using Co-Kα X-ray. The XRD patterns of the Ta thin films deposited with the presence of a piece of Kapton tape covering part of the substrate surface are shown in Figure 6.1a. When the deposition temperature is lower than 400 °C, the film consists of a mixture of α and β phases. With the increase of deposition temperature from room temperature to 400 °C, the proportion of β phase decreases, the β phase completely disappears at 400 °C, and the film is composed of single phased α-Ta. When the deposition temperature reaches 500 °C or 600 °C, both α and β phases disappear and the Ta films are composed of a single fcc phase. Similar results are obtained for other substrates, such as α-Ta coated silicon wafers and Co alloy sheets.

On the other hand, the XRD patterns of the Ta thin films deposited without Kapton tape, presented in Figure 6.1b, show similar results for deposition temperature up to 400 °C but no fcc phase formation at deposition temperature of 500 °C or 600 °C. Instead, the Ta films are composed of a single α-Ta phase at deposition temperatures of 400 °C and above. Again, these results are on the

same for other substrates. The XRD results indicate that the presence of impurities in the high vacuum deposition chamber is important to the formation of the aforementioned fcc phase, since the growth of this phase depends on the presence of a piece of Kapton tape on the substrate surface. The tape, containing carbon, oxygen, nitrogen, hydrogen, and silicon, would be evaporated and decomposed during the Ta film deposition at 500 °C or 600 °C.
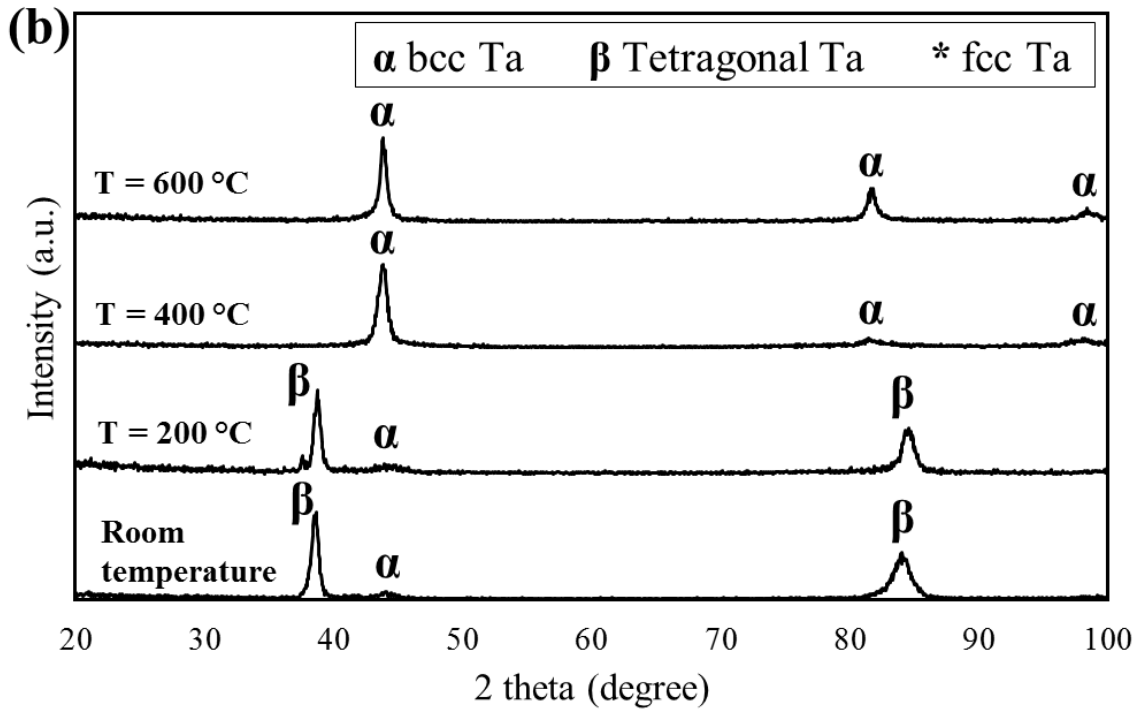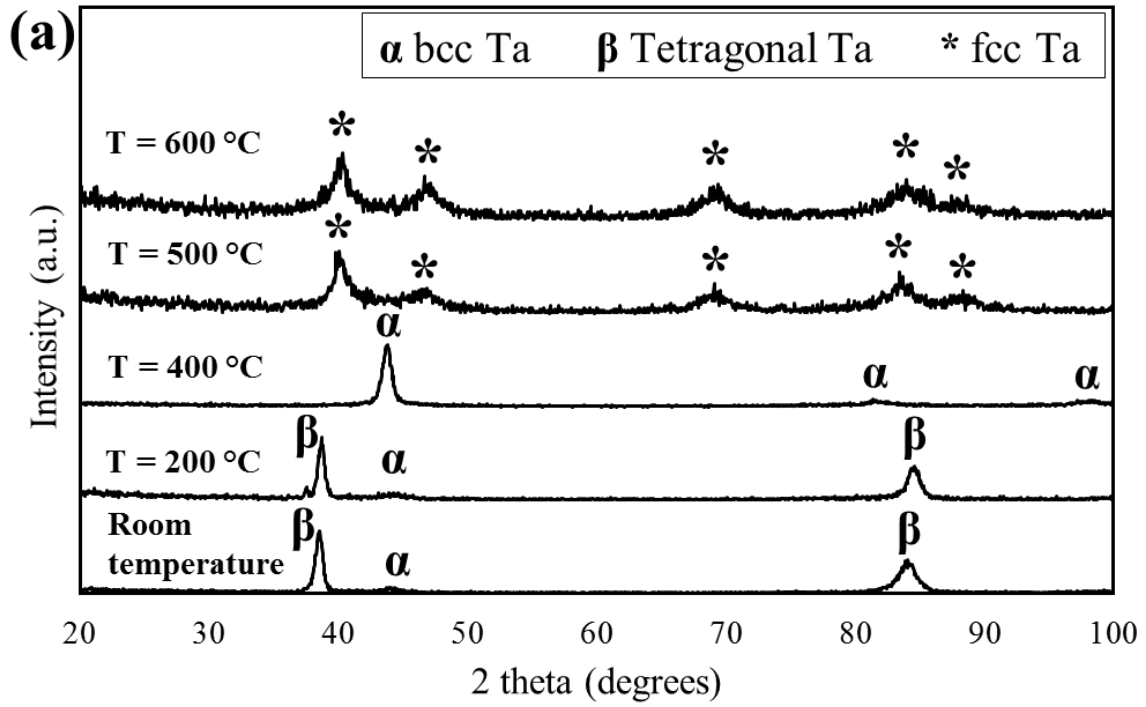
Figure 6.1. XRD patterns of Ta thin films deposited on silicon substrate (a) with the presence of kapton tape, and (b) without kapton tape

Figure 6.2 and Table 6.2 display the XRD diffraction pattern of fcc structure using 15 keV synchrotron X-ray and a list of crystallographic planes and interplanar spacing (d) values respectively. The high background at high d values in the XRD diffraction pattern is probably introduced by the fluorescent radiation from the Ta thin film. Based on these XRD data, the lattice parameter of the fcc phase has been determined to be 4.5065 Å using Nelson and Riley extrapolation function [110, 111], which is distinct but close to those of fcc TaC, TaO, and TaN, where a = 4.4547 Å for TaC, a = 4.4220 Å for TaO, and a = 4.3310 Å for TaN.

Because the tape used to cover part of the substrate in the deposition experiments may induce carbon, oxygen, nitrogen, hydrogen, and silicon impurities into the thin films, further analyses including XPS and XANES were performed to clarify if there is a formation of TaC, TaO, and TaN phases in the fcc Ta films.
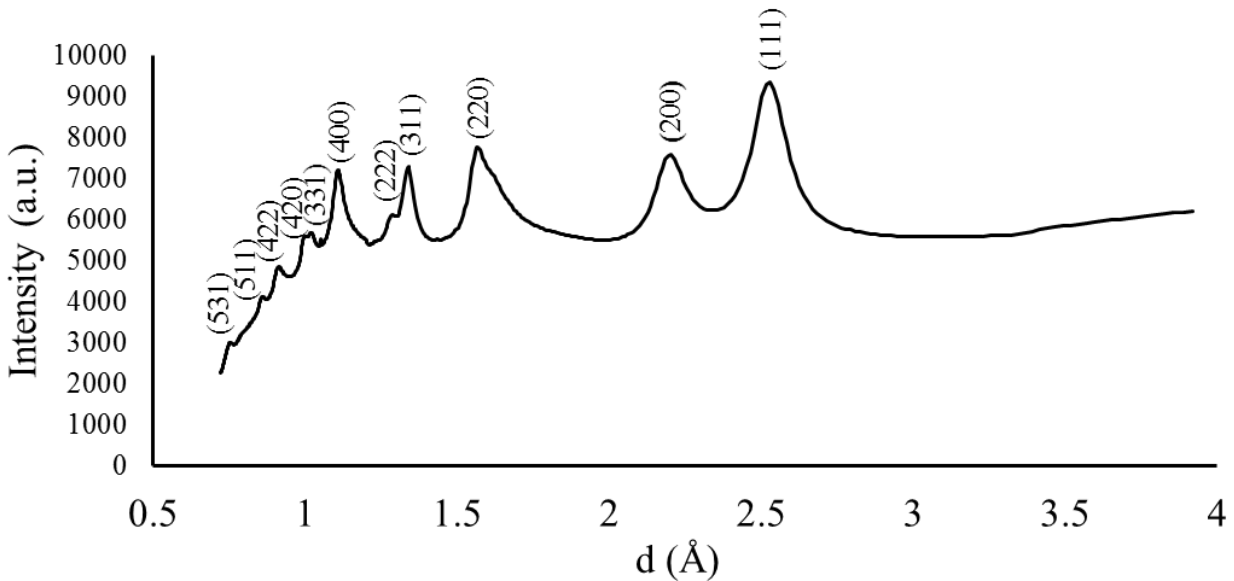
Figure 6.2. XRD pattern and observed crystallographic planes (hkl) of fcc phase thin film on silicon substrate

Table 6.2. Crystallographic planes (hkl) and corresponding interplanar spacing (d) values of fcc phase thin film on silicon substrate

No.	(h k l)	d (Å)
1	(1 1 1)	2.53
2	(2 0 0)	2.2
3	(2 2 0)	1.59
4	(3 1 1)	1.34
5	(2 2 2)	1.29
6	(4 0 0)	1.11
7	(3 3 1)	1.02
8	(4 2 0)	1
9	(4 4 2)	0.92
10	(5 1 1)	0.86
11	(5 3 1)	0.76

Figure 6.3 illustrates the XPS survey spectra of the fcc Ta thin film before and after Ar etching. The XPS spectrum of the film without in-situ Ar etching shows strong O 1s and C 1s peak and weak Ta peaks but no nitrogen and silicon peaks. As the film has been exposed to the atmosphere, it is reasonable that the film surface is contaminated and contains high amount of O and C. In contrast, one can see stark differences of the XPS spectrum of the film after 120 s etching, namely the Ta peaks are strong, O 1s peak is weak, and there is no trace of carbon impurity (or if there is any, it is below the detection limit of the XPS analysis). Continuing to increase the etching time step by step up to 1800 s to reach the silicon substrate, with 120 s Ar etching in each step, does not change the overall XPS spectrum, indicating that the chemical composition of the thin film is preserved as a function of thickness. By far, we can infer that there is no indication of TaC or TaN phases in the thin film.
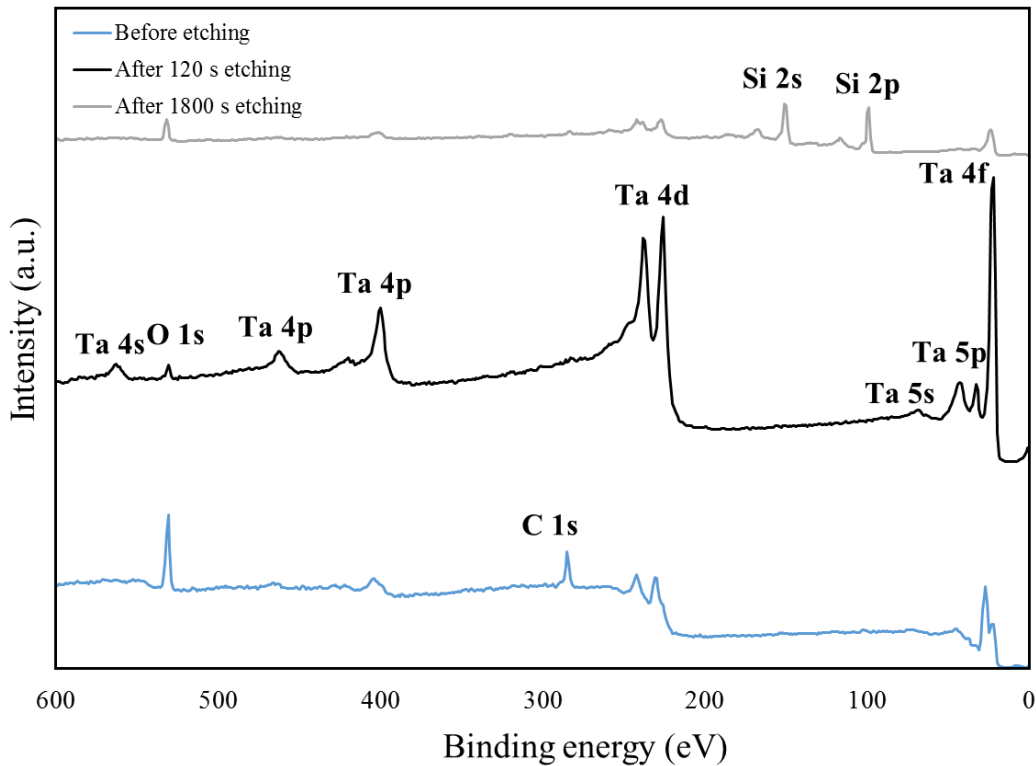
Figure 6.3. XPS spectra of fcc Ta thin film in a wide range with different etching time

In order to understand the bonding states of O and Ta in the films, fine XPS O 1s and Ta 4f peaks are further analyzed for Ta thin films with different crystal structures. Their O 1s spectra and Ta 4f spectra before and after 120 s Ar etching are shown in Figure 6.4a and Figure 6.4b, respectively, where the α (bcc) Ta thin film was obtained at a substrate temperature of 400 °C, and β (tetragonal) Ta thin film was obtained by applying 78 V substrate bias voltage at room temperature as mentioned in Chapter 4. For all the three samples, the O 1s peaks are similar and the relative concentration of O 1s peaks decreases significantly after 120 s etching. However, O 1s peaks with very low intensities, exactly same as O 1s peaks intensity after 120 s etching, still exist even after surface etching up to 1800 s. As can be seen from Figure 6.4b, the Ta 4f peaks related to the Ta oxide compounds disappeared after 120 s etching, indicating that all the Ta films are metallic and free of any oxide compounds [112, 113]. Nevertheless, the binding energy of Ta 4f is different slightly in different crystal structures as shown in Figure 6.4b.

Figure 6.5 shows the normalized XANES spectra at the Ta L3 edge of fcc, α (bcc), and β (tetragonal) Ta thin film samples. It can be seen from Figure 6.5b that the absorption edge of fcc

Ta thin film, with no chemical shift, is exactly the same as those of α and β Ta thin films. These results also clearly show that the fcc Ta film prepared in this research is a fcc metallic Ta rather than a mixture of fcc Ta and its compounds, since the absorption edge of Ta varies with respect to the chemical states [114].
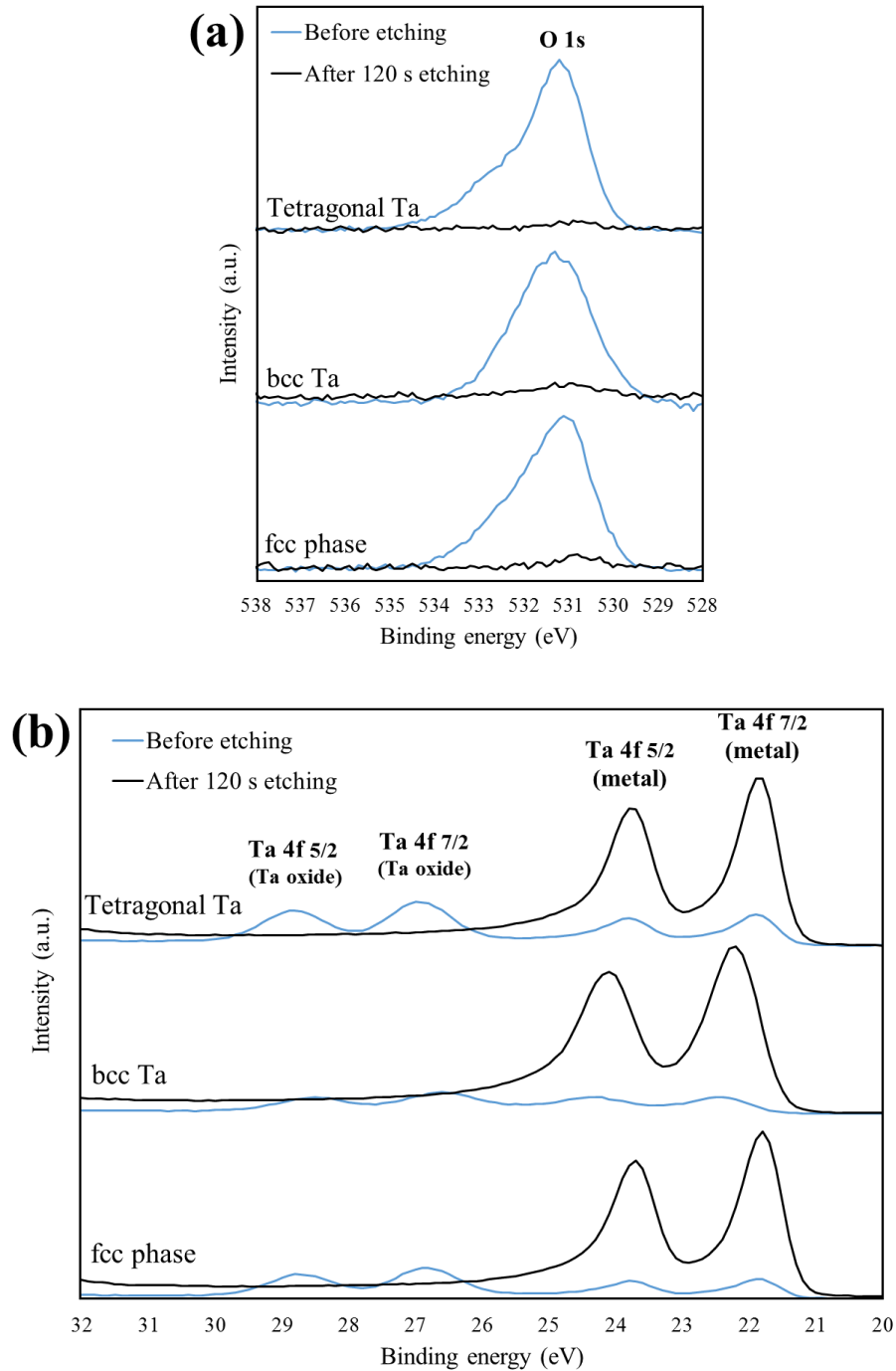
Figure 6.4. (a) O1s (b) Ta 4f fine XPS spectra of tetragonal, bcc, and fcc Ta thin films
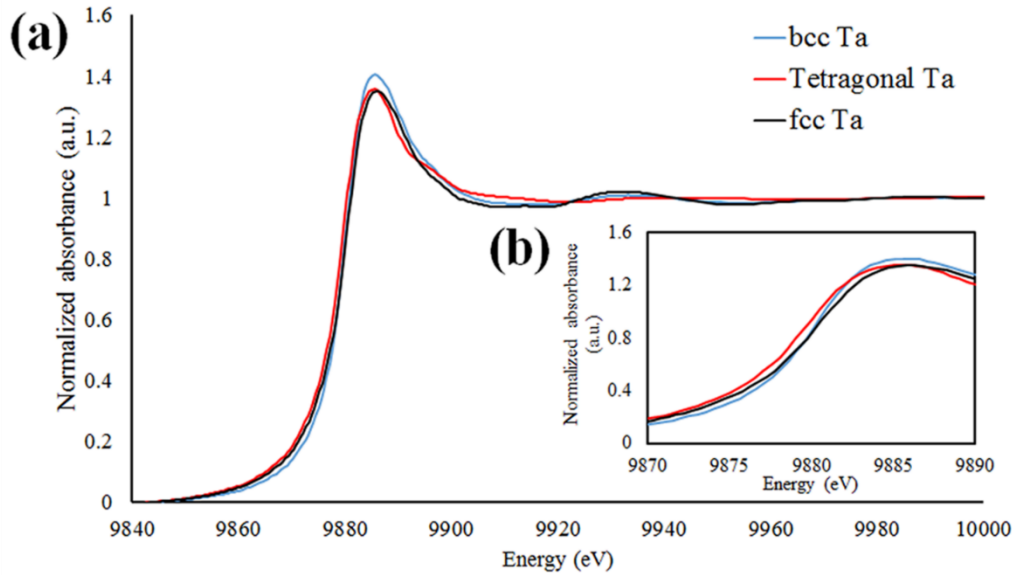
Figure 6.5. Normalized XANES spectra at the Ta L3 edge of tetragonal, bcc, and fcc Ta thin films (a) in a wide range (b) in a specific range

Researchers have reported the existence of fine grains of fcc Ta in Ta thin films previously and indicate that the surface forces and epitaxial growth on the appropriate substrate in the early stage of film deposition are the main mechanisms for fcc Ta formation [27-31]. The fact that fcc Ta exists in the films of 2 μm thickness in this study indicates that the epitaxial growth, which happens in very thin films at the very early stage of thin film growth (< 50 nm thickness), could not be the main formation mechanism of fcc Ta. Furthermore, similar fcc Ta thin films (their XRD patterns are shown in Figure 6.6) were also formed on α-Ta coating and Co alloy sheets, demonstrating that the crystal structure of the substrates materials has no effect on the formation of fcc Ta.

It is possible that the high kinetic energy of sputtered atoms may result in direct implantation of the Ta atoms into unstable lattice positions to strain the thin film on the substrate to facilitate the formation of fcc Ta, as surface forces have been proposed as a possible mechanism for formation of fcc Ta [28, 29]. Moreover, the present results show that the formation of fcc Ta is dependent on the impurities induced by a piece of tape on the sample's surface and high deposition temperature. It is possible that the small impurity atoms from the evaporation of the tape stay at interstitial sites and induce fcc Ta nucleation and growth. In this regard, Marcus *et al*. [29] reported the necessity of at least one monolayer oxygen impurity on the substrate for the growth of fcc structure in 5 nm Ta thin film. To have a better understanding of the effect of impurities on the crystal structure of

Ta thin films, a low amount of nitrogen, carbon, and oxygen was intentionally introduced into the deposition chamber during the Ta film deposition. In these experiments, no fcc Ta could be obtained, similar to the case without the tape. Further researches are needed to be done in order to clarify the underlying formation mechanism of fcc Ta.

Figure 6.7 shows the XRD patterns of the fcc Ta thin films deposited at 500 °C without and with an annealing at 700 °C and 750 °C. The patterns show that the fcc Ta keeps its structure up to 700 °C and transforms to α-Ta phase with a bcc structure at 750 °C or above. It should be noted that the formation of fine grains of fcc Ta reported previously occurred at relatively low temperatures (room temperature up to 400 °C), moreover, with increasing the temperature this structure disappears [27-31]. However, it requires a deposition temperature of 500 °C or 600 °C with a tape to obtain fcc Ta films of 2 μm thickness in the present research study, and the fcc structure is stable up to 700 °C. Further research is being carried out to have a deeper understand of the formation mechanism of fcc Ta. Furthermore, because of the nanosize of the fcc Ta grains, the dispersed nature, and the tiny amount obtained from previously researches, it was impossible to get a reliable XRD pattern of fcc Ta and thus no papers have reported the XRD patterns of fcc Ta until now. The lattice parameter of fcc Ta was estimated by Denbigh *et al*. [27], Chopra *et al*. [28], Marcus *et al*. [29], Schrey *et al*. [30], Janish *et al*. [31] to be 4.42, 4.39, 4.42, 4.48, 4.30 Å, respectively, using electron diffraction in TEM, which are very close to those of TaC, TaO, and TaN and a little bit smaller than the value determined by XRD in the present research. The present manuscript is the first to report the synthesis of fcc Ta thin films with microscale thickness and to present the XRD data and the accurate lattice parameter for fcc Ta.
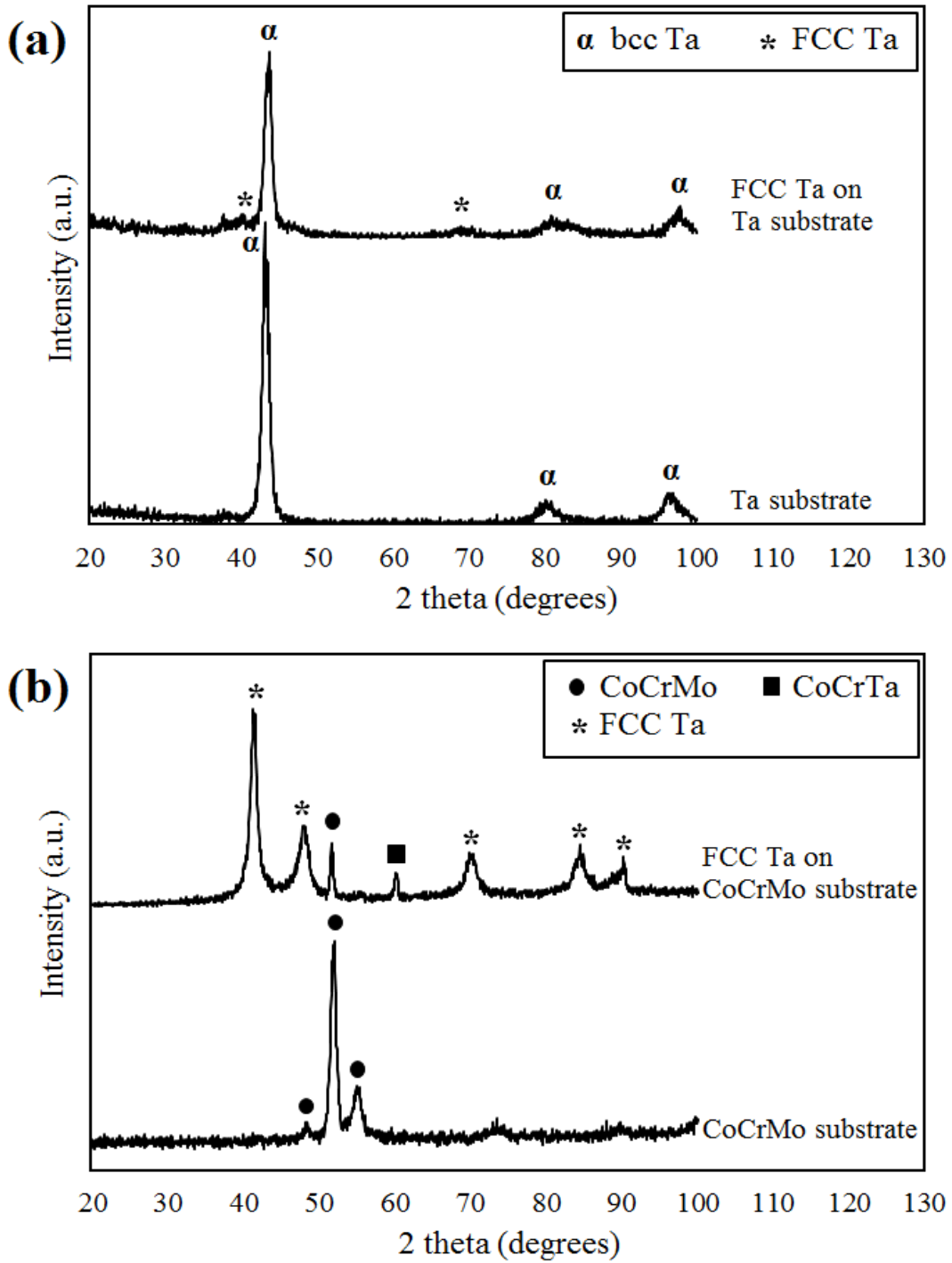
Figure 6.6. XRD patterns of fcc Ta formation on (a) Ta (b) Co alloy
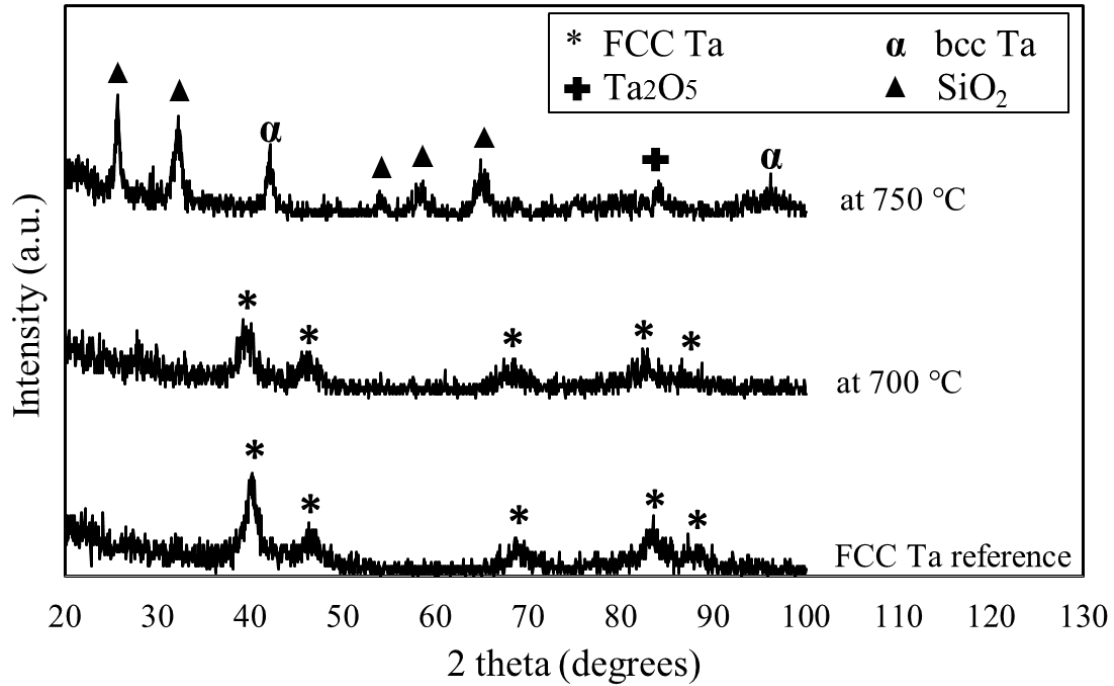
Figure 6.7. XRD patterns of fcc Ta samples annealed at different temperatures

6.4 Conclusions

fcc Ta thin films with a thickness of 2.0 ± 0.2 μm were successfully synthesized using magnetron sputtering at a substrate temperature of 500 °C and 600 °C for the first time. The results show that the formation of fcc Ta is dependent on thin film deposition parameters and impurity level. The XRD patterns of the mentioned phase is obtained and reported for the first time, and the lattice parameter is determined to be 4.5065 Å using XRD. The crystal structure of the substrate materials has no effect on the formation of fcc Ta and the fcc Ta keeps its crystal structure up to 700 °C but it transforms to α-Ta after annealing at 750 °C.

CHAPTER 7

INVESTIGATING THE ADHESION OF DLC COATINGS ON CoCrMo ALLOY SHEETS USING TANTALUM INTERLAYERS

DLC coatings attract considerable attention for many tribological applications especially in medical implants and prosthesis. In view of the attractiveness of CoCrMo alloys for use in artificial hip joints, research has been carried out to prevent the release of Co into body fluids and to reduce the wear rate of polyethylene cup using DLC coatings. However, poor adhesion has remained a major challenge of DLC coatings on CoCrMo alloys. In this chapter, the results of investigation of Ta as an interlayer to enhance the adhesion of DLC coating on CoCrMo alloy are presented and discussed. This chapter is a transition chapter and will not be submitted as a journal paper. My contributions to this chapter are: review of the relevant literature, design and conduct the experiments, and analysis of the test results under the supervision of Professor Qiaoqin Yang and Professor Akindele Odeshi.

Abstract

In this study, we report on using Ta as an interlayer to enhance the adhesion of DLC coatings on CoCrMo alloy sheets. Ta and DLC coatings are deposited on CoCrMo alloy sheets using magnetron sputtering and ion beam deposition, respectively. Severe delamination of the DLC coatings is observed on the samples using iPhone 6s camera and SEM images. Raman spectroscopy and XPS are used to characterize the composition and bonding states of the coatings. The results show that the DLC coatings delamination is due to the interface layer formation with the Ta film on one side and the DLC film on the other side. This layer consists of a mixture of Ta carbides and metallic Ta, and shows weak mechanical bond with DLC film.

7.1 Introduction

DLC coatings have high hardness, low friction coefficient, high wear resistance, and excellent biocompatibility and thus attract considerable attention for medical applications in implants and

prostheses [2, 69]. Several research investigations have been carried out on the tribological behavior of DLC coated CoCr alloys. Conflicting results have been obtained. A major issue for these coatings is the weak adhesion of DLC to the substrate. Owing to the high level of internal stresses of DLC films and the large differences in physical properties between DLC coatings and substrates (e.g. thermal coefficient of expansion), DLC have a tendency to have weak adhesion to metallic substrates. Muller *et al*. [77] and Fallub *et al*. [78] investigated the interface between DLC films on a CoCrMo alloy and indicated that the interface is a main factor that controls adhesion. These authors reported that a very thin layer consists of a mixture of carbides from all the alloy's metal components was formed in the interface. They mentioned that these interfacial carbides played an important role in promoting poor adhesion of the DLC films on the CoCrMo alloy. So far, several approaches have been investigated to overcome these drawbacks and improve the adhesion of DLC film on the substrate. These include designing a proper interlayer (a single or a graded layer), and doping and changing the composition of the thin films. Falub *et al*. [78, 79] reported that the adhesion of DLC film on CoCrMo alloy can be greatly improved by using Mo [78] or Si-doped DLC [79] interlayers. These interlayers affect adhesion by enhancing the interfacial bonding between the substrate and the DLC, while the chemical bonds at the interface are mostly Mo carbides for the Mo interlayer, and metal carbides and metal silicides for the Si-doped DLC interlayer. However, they showed that the adhesion of DLC film on the CoCrMo alloy is impaired by Co interlayer because of the instability of Co carbides at the interface. Liu *et al*. [80, 81] and Guo *et al*. [82] reported that Ti and Cr interlayers have positive effects on the performance of DLC coated CoCrMo alloys. Huart *et al*. [83, 84] used Si interlayer to improve DLC adhesion, but showed the failure of the DLC coated CoCrMo alloy mainly caused by in vivo crevice corrosion of the interlayer. Recently, Ta has been introduced by Thorwarth *et al*. [85] as a promising candidate for use as an interlayer to enhance DLC adhesion on CoCrMo alloys and improve the performance of DLC, distinguished by its excellent corrosion and mechanical resistance, high biocompatibility, insolubility in body fluids, and good fatigue properties under long-lasting mechanical cyclic stresses. They showed that amorphous/α-Ta interlayers performed well with no corrosion or mechanical failure, but very low contamination during the Ta interlayer deposition led to the formation of β-Ta, which caused coating failure. In this study, α- and β-Ta phases are investigated as potential interlayers to enhance DLC adhesion on the CoCrMo alloy.

7.2 Experimental details

CoCrMo alloy (ASTM F1537) sheets with a thickness of 3 mm and a diameter of 25 mm were ground, polished, and cleaned as explained in Section 4.2. The prepared sheets were used as substrates for Ta interlayer and DLC thin film deposition. Ta interlayer was deposited on the CoCrMo alloy sheets using RF Magnetron Sputtering. Ar gas was introduced into the chamber at a flow rate of 35 sccm. The deposition pressure was kept at 1.33 Pa while RF power for sputtering was kept at 150 W. β-Ta films were deposited at room temperature by applying a negative bias of 78 V for 30 min onto the substrate holder. α-Ta thin film samples were prepared in three steps as follows:

1. A β-Ta layer by applying a negative bias of 78 V at room temperature for 10 min
2. A layer with a mixture of β-Ta and α-Ta by increasing the substrate temperature from room temperature to 400 °C gradually without biasing for 15 min
3. An α-Ta layer by keeping the substrate holder at 400 °C without biasing for 15 min.

A more detail discussion on the Ta thin films deposition is provided in Section 4.2.

DLC films were deposited on the Ta-coated CoCrMo alloy samples using End Hall Ion (EHI) source in ion beam deposition system manufactured by 4Wave Inc. The substrate holder was mounted inclined at 45° with respect to the ion source. Prior to the deposition, the prepared samples were cleaned in the deposition chamber by introducing 12 sccm Ar gas into the ion source, and applying of 50 eV ion energy for 10 min. For DLC deposition, CH_4 and Ar gases were introduced into the ion source, the working pressure was 0.0933 Pa, and the deposition time was 6 h. The details of the DLC deposition under the two different conditions are listed in Table 7.1.

Table 7.1. Deposition conditions of DLC thin films on CoCrMo alloy sheets with Ta interlayers

Condition	Ion energy (eV)	CH_4 flow rate (sccm)	Ar flow rate (sccm)	Temperature (°C)
(a)	65-70	15	10	30
(b)	80-85	12	6	30

The thickness of the thin films was measured using Zygo optical profiler. The surface morphology of the thin films was characterized using iPhone 6s camera, and Jeol JSM-6010LV SEM operated at 5 kV. The chemical bonding of the thin films was analyzed using Raman spectrometer (Reinshaw model 2000) equipped with 514 nm wavelength of Ar laser. Furthermore, the chemical composition of the samples was investigated using XPS (model: AIXS SUPRA) with Al Kα radiation as the excitation source at the SSSC. CasaXPS software was used to analyze the obtained XPS data.

7.3 Results and discussion

Figure 7.1 shows the images of the DLC thin films deposited on CoCrMo alloy sheets with α- and β-Ta interlayers using different ion energy ranging from 65-70 eV to 80-85 eV. The thickness of all the interlayers is about 200 nm. In the SEM images, the grey area corresponds to the exposed substrate/interlayers, and the black area corresponds to the remaining film that is adhered to the substrate/interlayers. In this study, the growth of continuous DLC films on the samples with a range of ion energy seems impractical. Having a good knowledge on the DLC coatings adhesion mechanism is an important factor for the success of such coatings. Therefore, further investigation is carried out to study the poor adhesion of DLC films on the samples.

Figure 7.2 displays the Gaussian-fitted Raman spectra of the deposited DLC films in the non-delaminated area, showing two broad peaks centered at around 1350 cm^{-1} (D band) and 1580 cm^{-1} (G band), like a typical DLC [115]. The intensity ratio of D and G peaks (Id/Ig) is related to the deposition ion energy and decreases with the increase in ion energy as shown in Table 7.2. The Id/Ig value represents the sp^3 carbon bond content in the films. The sp^3 bond content of the DLC films increases with the decrease in Id/Ig value. Therefore, applying high ion energy during the deposition creates large amount of sp^3 carbon bonds.
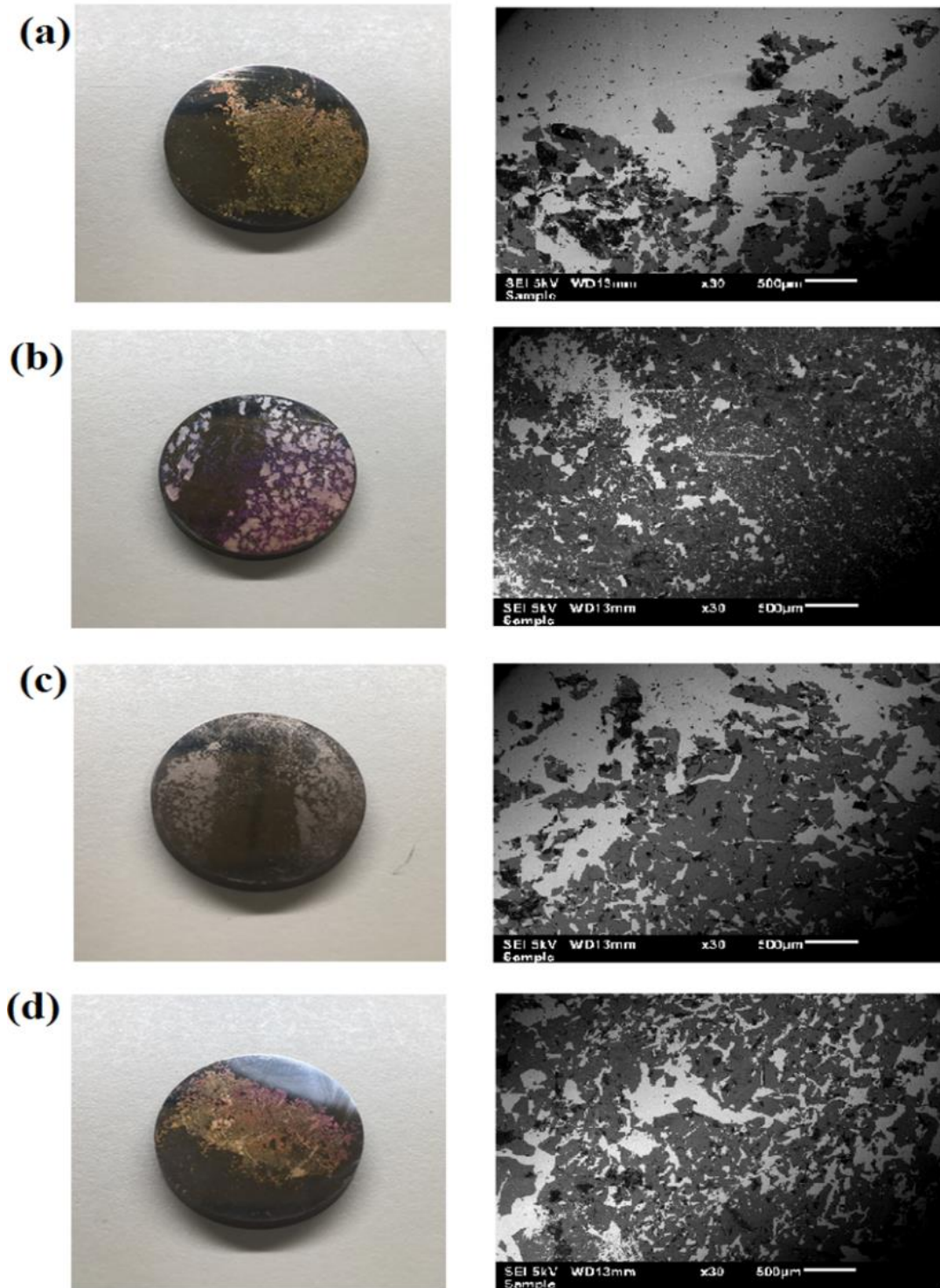
Figure 7.1. Photograph and SEM images of DLC thin films deposited on CoCrMo alloy sheets with α-Ta interlayer at (a) 80-85 eV (b) 65-70 eV ion energy, and with β-Ta interlayer at (c) 80-85 eV (d) 65-70 eV ion energy
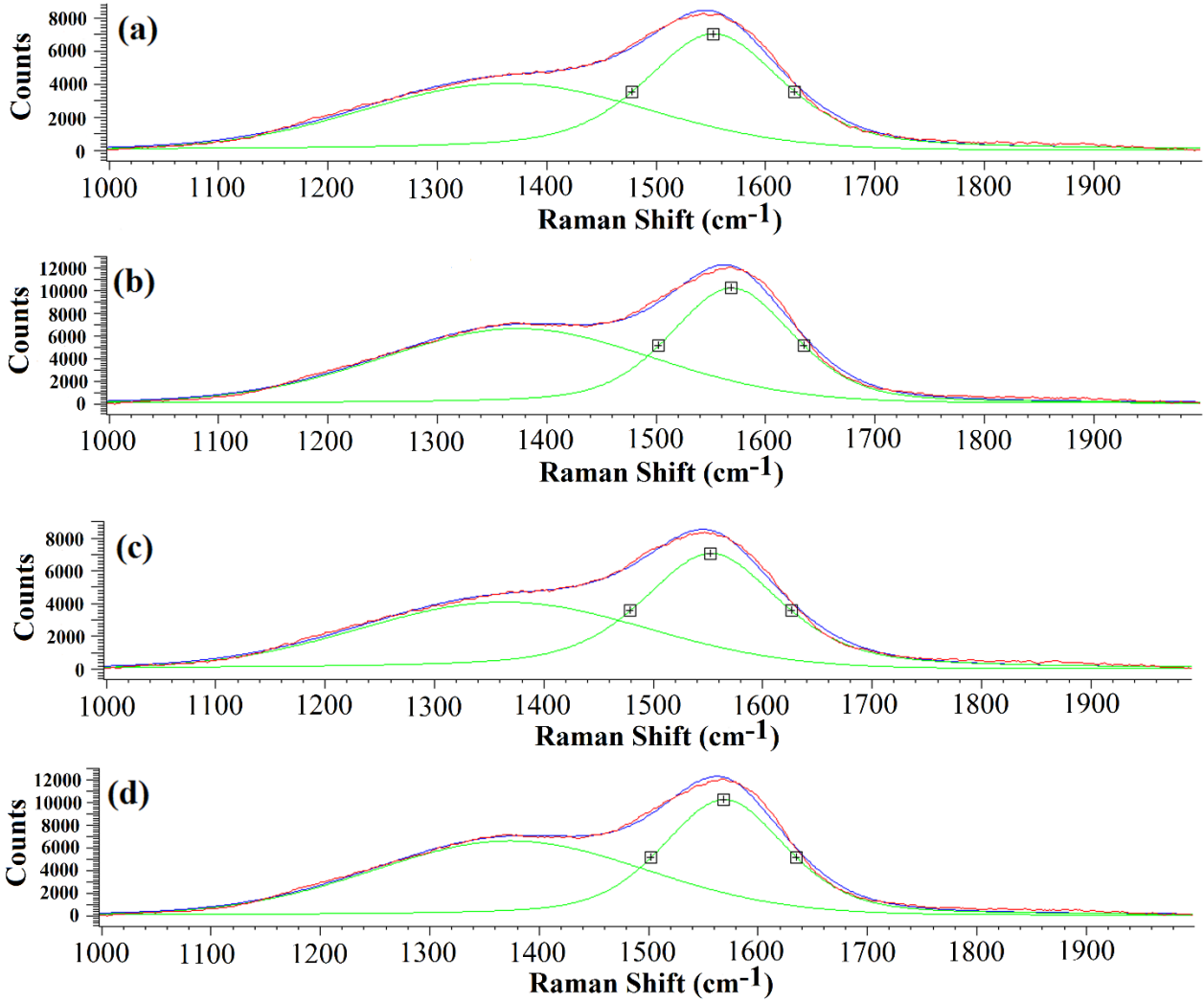
Figure 7.2. Raman spectra of DLC thin films deposited on CoCrMo alloy sheets with α-Ta intelayer at (a) 80-85 eV (b) 65-70 eV ion energy, and with β-Ta interlayer at (c) 80-85 eV (d) 65-70 eV ion energy

Table 7.2. The intensity ratio of D and G peaks (Id/Ig) as a function of deposition ion energy

Ion energy (eV)	80-85	65-70
Id/Ig for CoCrMo alloy + α-Ta interlayer samples	1.07	1.28
Id/Ig for CoCrMo alloy + β-Ta interlayer samples	1.04	1.22

It is observed in this study that applying high ion energy in DLC deposition process induces high intrinsic stress into the DLC film, which can lead to film delamination. However, applying lower ion energy (the lowest amount of ion energy that form DLC) shows the similar results, which is bad adhesion but less delamination. The results show that the delamination is not just related to the amount of ion bombardment energy which induced intrinsic stress into the film, but also related to the interfacial bonding between DLC, interlayers, and substrate. In this regard, XPS measurement was carried out on the samples' surfaces in the DLC-coated and delaminated areas to determine which interface fails, substrate/interlayer or interlayer/DLC. Figure 7.3 provides the full XPS spectra of CoCrMo alloy/α-Ta/DLC (deposited at 80-85 eV ion energy) sample. Only Ta interlayer peaks and no substrate peaks are observed on the sample's surfaces on both coated and delaminated area, which indicates that Ta interlayer exists on the sample and the failure occurred at the Ta interlayer/DLC interface. Ta is observed to exhibit very low intensity peaks while C 1s has very high intensity peak on the coated area compare to the delaminated area. All the samples show similar results.
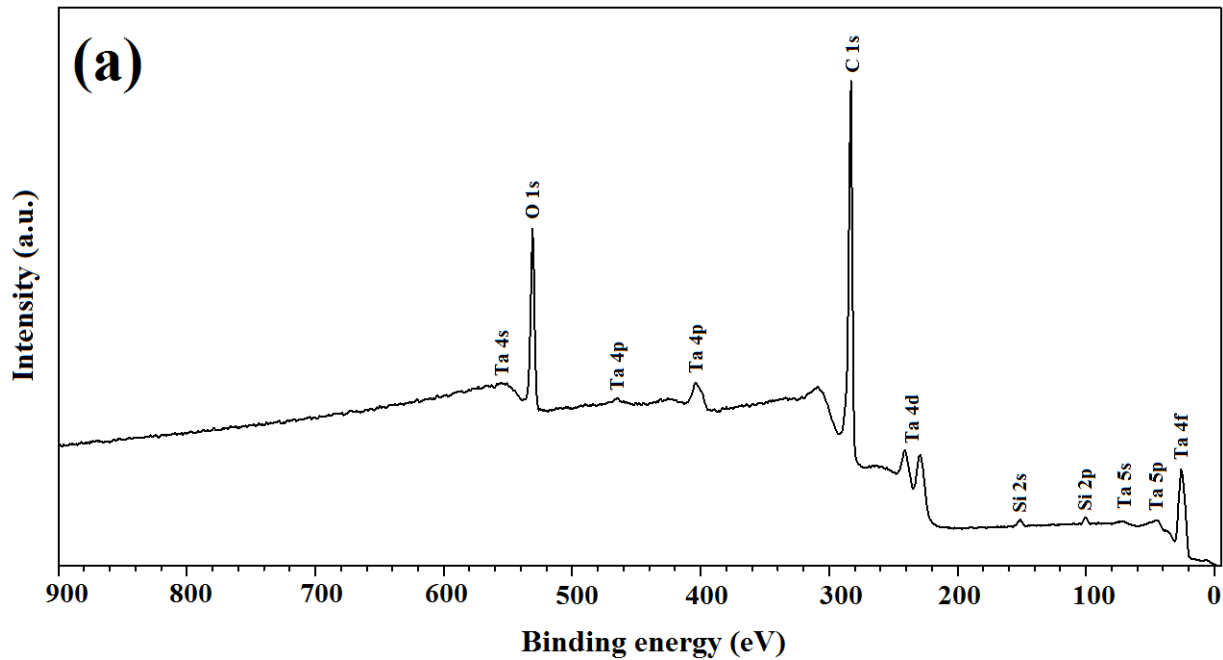
Figure 7.3. XPS spectra of "CoCrMo alloy/α-Ta/DLC (deposited at 80-85 eV ion energy)" sample on the (a) DLC-coated and (b) delaminated area

Further investigation was done on Ta 4f and C 1s XPS spectra of the samples, and the results presented in Figures 7.4 and 7.5, respectively. In total, six peaks are observed for Ta 4f XPS spectra (Figure 7.4): at approximately 22 eV and 24 eV binding energies assigned to metallic Ta, at approximately 23 eV and 25 eV binding energies assigned to TaC, and at approximately 26 eV and 28 eV binding energies assigned to Ta_2O_5 [112, 116-118]. The C 1s XPS spectra is also fitted by four peaks at approximately 283 eV, 284 eV, 285 eV, and 286 eV binding energies assigned to TaC, sp^2, sp^3, and adventitious carbon contamination on the samples [119] (Figure 7.5). This is an indication of the existence of TaC and Ta_2O_5 compounds, and metallic Ta on the samples' surfaces. Ta_2O_5 is an inevitable compound that forms on the Ta metal surface when the sample is exposed to air, while TaC is suggested to have formed during the DLC deposition. The poor adhesion of the DLC films might be related to the existence of mixed Ta carbide and metallic Ta in the films. Ta is not a strong carbide former and cannot form an interface layer of carbide, so its mixture with metallic Ta may cause a weak mechanical bond between this interface layer and DLC. The only difference in XPS spectra of the samples at DLC-coated and delaminated area is in their peaks intensities.
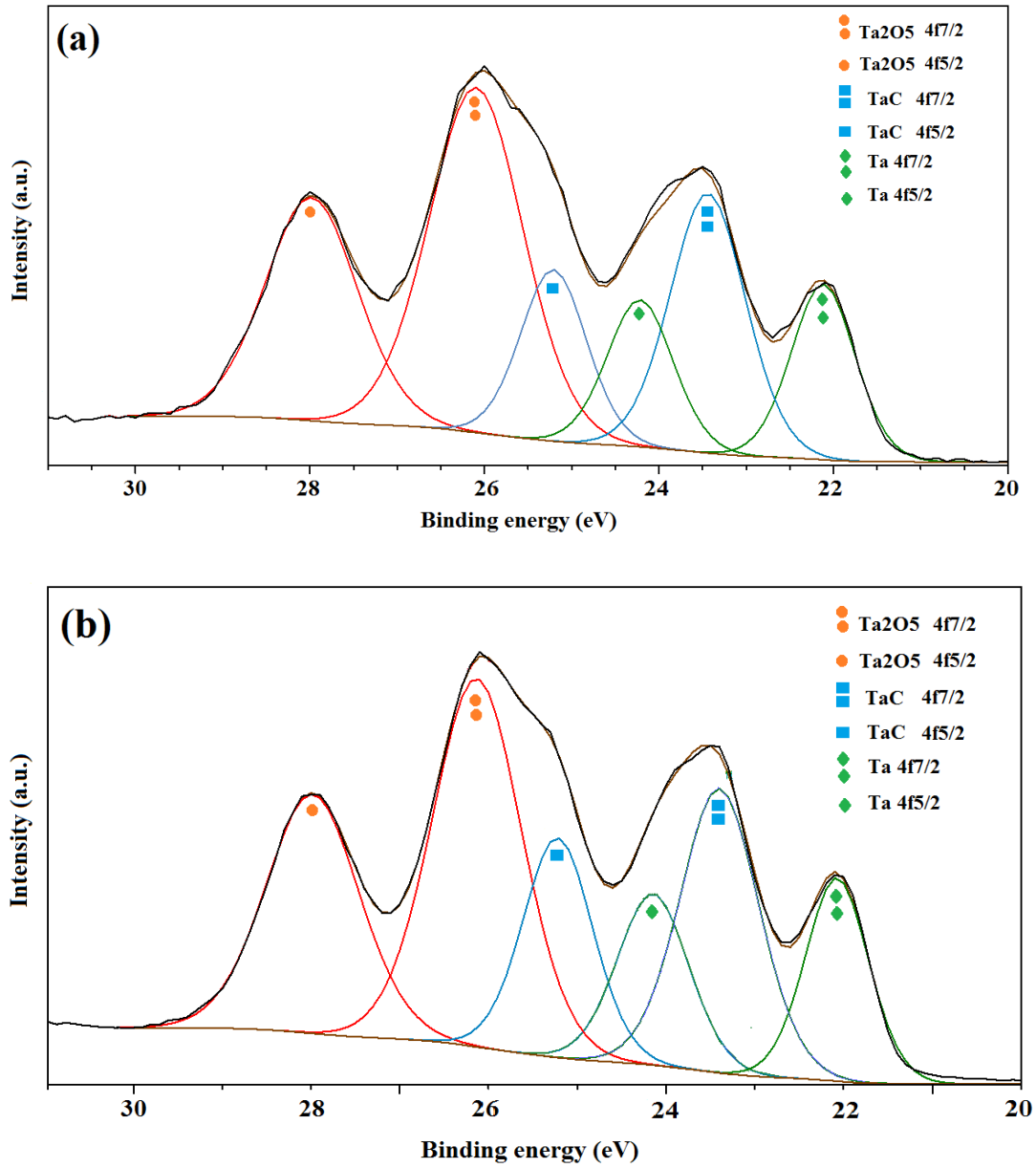
Figure 7.4. Ta 4f XPS spectra of "CoCrMo alloy/α-Ta/DLC (deposited at 80-85 eV ion energy)" sample on the (a) DLC-coated and (b) delaminated area
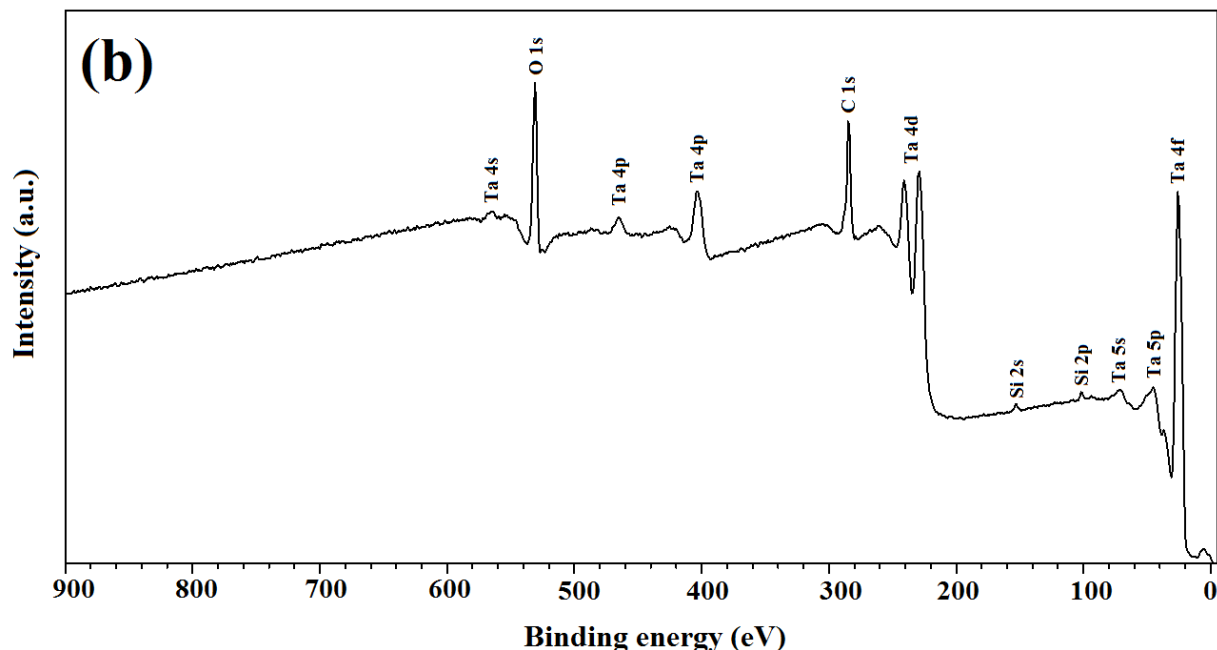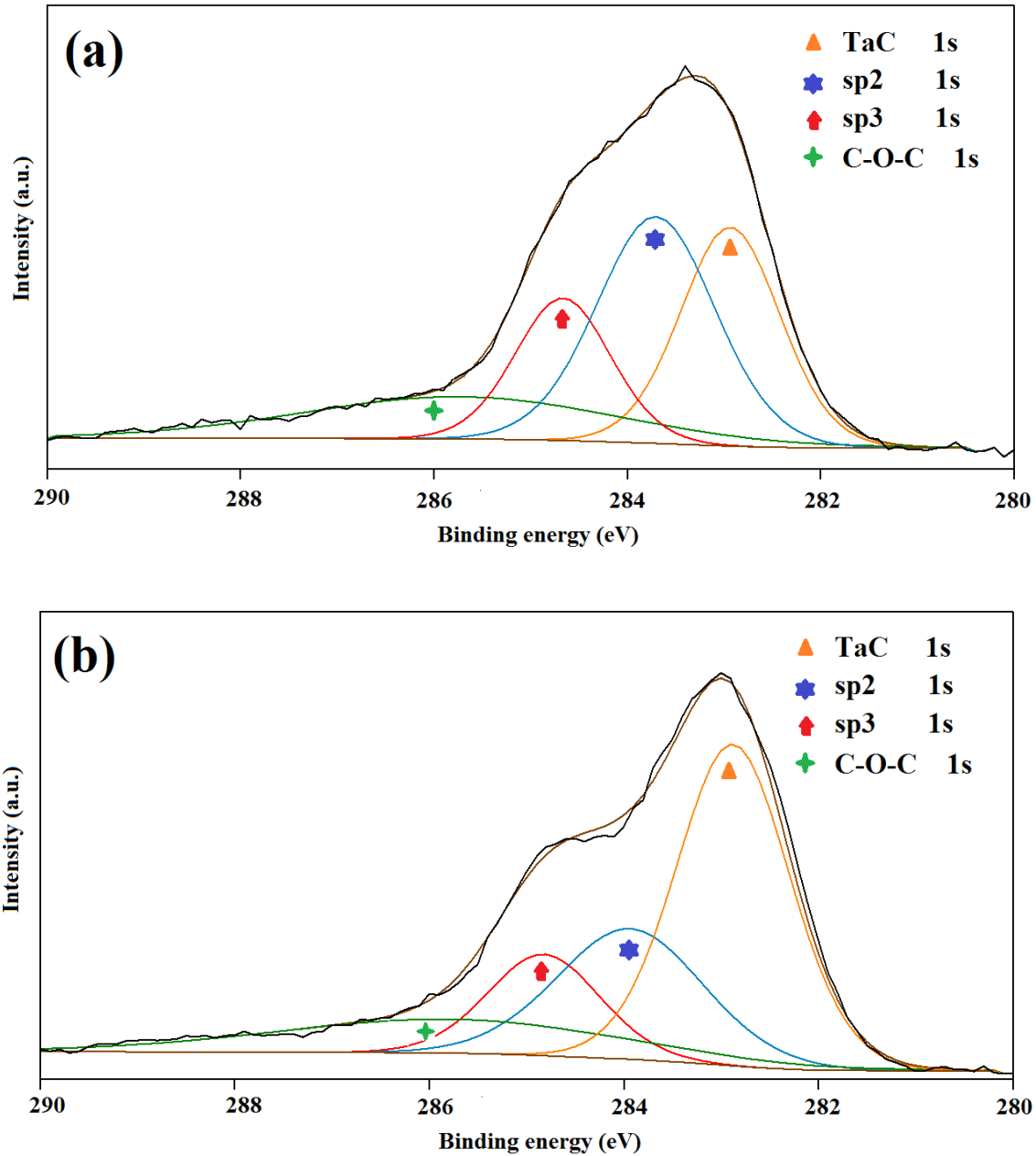
Figure 7.5. C1s XPS spectra of "CoCrMo alloy/α-Ta/DLC (deposited at 80-85 eV ion energy)" sample on the (a) DLC-coated and (b) delaminated area

7.4 Conclusions

Two different types of Ta film, α-Ta and β-Ta, were used as an interlayer in order to improve the adhesion of DLC coatings on CoCrMo alloy sheets. Severe delamination of the DLC coatings was observed on all the samples. A thorough investigation is done to understand the delamination

mechanism. The results show that the delamination is not just related to the amount of ion bombardment energy inducing intrinsic stress into the film during DLC deposition, but related to the interfacial bonding between the DLC and the interlayers. An interface layer is formed at Ta/DLC interface during DLC deposition, this layer is composed of a mixture of Ta carbide and metallic Ta, resulting in weak mechanical bonding with the DLC films.

CHAPTER 8

EVALUATION OF STONEY EQUATION FOR DETERMINING THE INTERNAL STRESS OF DLC THIN FILMS USING AN OPTICAL PROFILER

Excessive internal stresses in DLC films induced by the energetic ion bombardment during the deposition cause poor adhesion even delamination of the thin films from the substrate surfaces as mentioned in Chapter 7. As a result, determination of internal stresses in DLC films is essential for their applications. The present chapter presents a simple non-destructive method for measurement of stress in DLC coatings using an optical profiler. This chapter is published in "Surface & Coatings Technology" as follows:

"Evaluation of Stoney equation for determining the internal stress of DLC thin films using an optical profiler, S. Shiri, P. Ashtijoo, A. Odeshi, Q. Yang, Surface & Coatings Technology 308 (2016) 98–100".

My contributions to this paper are: review of the relevant literature, design and conduct the experiments, analysis of the test results and preparing the manuscripts under the supervision of Professor Qiaoqin Yang and Professor Akindele Odeshi. The manuscript was reviewed and revised by my supervisors, Professor Qiaoqin Yang and Professor Akindele Odeshi, before submission to the journal for publication. The present manuscript is a modified version of the published paper. The copyright permission is obtained and provided in the Appendix section.

Abstract

In this study, DLC thin films are prepared on thin silicon wafers with different shapes and sizes by end hall ion beam deposition. Optical profiler is used to measure the curvature of the samples before and after DLC deposition and then the Stoney equation is used to calculate the residual stress of DLC thin films in order to evaluate the feasibility of this method for measurement of DLC

stress. For this purpose, the curvature radius in different directions of all the samples is measured before and after DLC deposition by the optical profiler. The calculated stress values using Stoney equation for all the samples are the same within reasonable errors. These results show that this simple method is appropriate and reliable for stress measurement of DLC films.

8.1 Introduction

DLC thin films have a wide range of applications because of their unique properties, such as extremely low friction coefficient, chemical and biological inertness, high hardness, and excellent biocompatibility [115]. One of the main problems limiting the applications of DLC is the high intrinsic stress which is induced by high energy ion bombardment during the deposition processes. High stress induces microcracks in the film and causes poor adhesion of the film to the substrate and thus results in premature failure. Therefore, measurement and control of the stress in DLC thin films has been getting increasing attention [115, 120]. Currently, beam deflection, based on the measurement of the radius of curvature of the samples before and after thin films deposition is the main technique for the stress measurement in DLC [121]. The most powerful technique, X-ray diffraction, which is based on the direct measurements of the changes of interplanar spacing in the film [121], cannot be used to measure the stress of DLC thin films because of the amorphous nature of the films. The common stress measurement method for diamond thin films, Raman spectroscopy, based on the peak shift, cannot be used to measure the stress of DLC either because of the broadening and overlapping of the Raman peaks. The only way to measure the stress of DLC is based on curvature measured before and after film deposition using Stoney equation (Equation 8.1)) [122, 123]:

$$\sigma = \frac{Es}{6\,(1-\vartheta s)}\frac{hs^2}{hf}\left(\frac{1}{R}-\frac{1}{R0}\right) \qquad (8.1)$$

Where Es is the Young's modulus, vs is the Poisson's ratio, hs is the thickness of the substrate, hf is the thickness of the thin film, and R0 and R are the curvature radii of the sample before and after deposition.

The Stoney equation for stress calculation is based on the following assumptions [122]:

- Thicknesses of the substrate and coating should be smaller than the lateral dimensions;

- Deformations and rotations should be infinitesimal;

- Thickness of the coating should be smaller than the thickness of the substrate;

- Substrate and the coating should be homogenous, isotropic and linear elastic;

- Radius of curvature should be equal in all directions (spherical deformation);

- Stress and the radius of curvature should be constant on the whole surface of the substrate.

However, some research works show that the shape and size of the substrate has influence on the deformation and curvature radii of the samples [124]. M. Ahmed *et al*. [124] showed that the deformation in all different substrate shapes is not spherical and Stoney equation cannot be applied to measure samples in many shapes. For most of the samples, spherical deformation is hard to be assumed, and deviation of curvature radii value in different directions causes measurement errors. Therefore, careful attention should be given to minimize the dispersion of the curvature radii [125-129].

On the other hand, Schwarzer *et al*. [130] theoretically showed that in thin substrates, the nature of the deformation after coating doesn't depend on the substrate shape and size. The purpose of this study is to experimentally examine the effect of substrate shape and size on the measurement of stress in DLC thin films using optical profiler to measure the curvature radii and to evaluate the appropriateness and reliability of this method for stress measurement of DLC.

8.2 Experimental details

(100) Silicon wafers of 0.5 mm thick was cut into samples with seven different shapes and sizes: squares (1 cm × 1 cm and 1.5 cm × 1.5 cm), rectangles (1 cm × 1.5 cm, 1 cm × 2 cm, and 1 cm× 2.5 cm), and circles (1 cm and 1.5 cm in diameter). The curvature radii of the samples were measured by an optical profiler made by Zygo before DLC deposition. The measurement was in two orthogonal directions along the x and y axes, and three measurements for each direction. The x and y directions are parallel to the sides of square and rectangular samples, in which the x direction is along with the longer side of rectangle and y direction is along with the shorter side of the rectangle. The average value for each direction was used for stress calculation. The radius measured along the x-and y-axis is noted Rx and Ry, respectively.

After the cutting, Si wafers were cleaned in an ultrasonic bath for 10 min, washed with ethanol solution, and dried before putting into the vacuum chamber for DLC film deposition. The DLC film deposition was carried out in a dual ion beam deposition system manufactured by 4Wave Inc.. DLC thin films were prepared using EHI beam deposition by introducing 8 sccm CH_4 and 12 sccm Ar gases into the EHI source. The working pressure was 0.0933 Pa, the ion energy for deposition was about 70 eV, and the deposition time was 4 h. The DLC films were analyzed using Reinshaw Raman spectrometer equipped with 514 nm wavelength of Ar laser. The curvature radii of the samples in x and y axes were then measured after DLC deposition.

The coating thickness was measured by using the same optical profiler. After all the measurements, the internal stress in different directions for all the samples was calculated using the Stoney equation (Eq. (8.1)). This experiment was repeated for two times. The average values and the standard deviation (SD) were presented.

8.3 Results and discussion

A typical Raman spectrum of the DLC film deposited on the Si wafers is shown in Figure 8.1. It shows the typical D and G peaks of DLC at around 1350 cm^{-1} and 1580 cm^{-1}, respectively, confirming its DLC nature. The surface profile of the samples before DLC coating is different for different samples and has no consistent curvature. After the DLC coating, nearly all the samples show spherical convex deformation due to the compressive stress which is created during DLC deposition through high energetic ion bombardment (Figures 8.2, 8.3, and 8.4). The measured values (average and standard deviation) of curvature radii in two directions are listed in Table 8.1. The results show that the average curvature values in different directions for the same sample are the same after DLC deposition, indicating that the deformation caused by coating DLC are spherical and the initial curvature, shape and size of the substrate do not show influence on the deformation of samples after coating. The results are in contradict with the results report by Ahmed *et al*. [124] but verified Schwarzer's theoretical prediction [130].
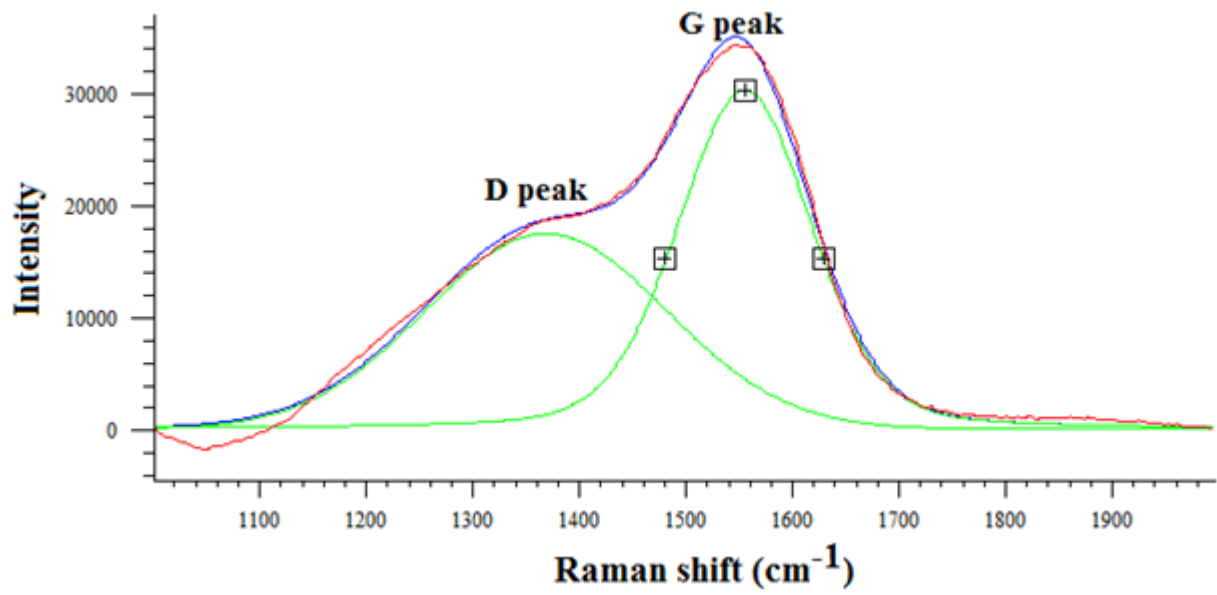
Figure 8.1. Raman spectra of DLC film deposited on the Si wafer
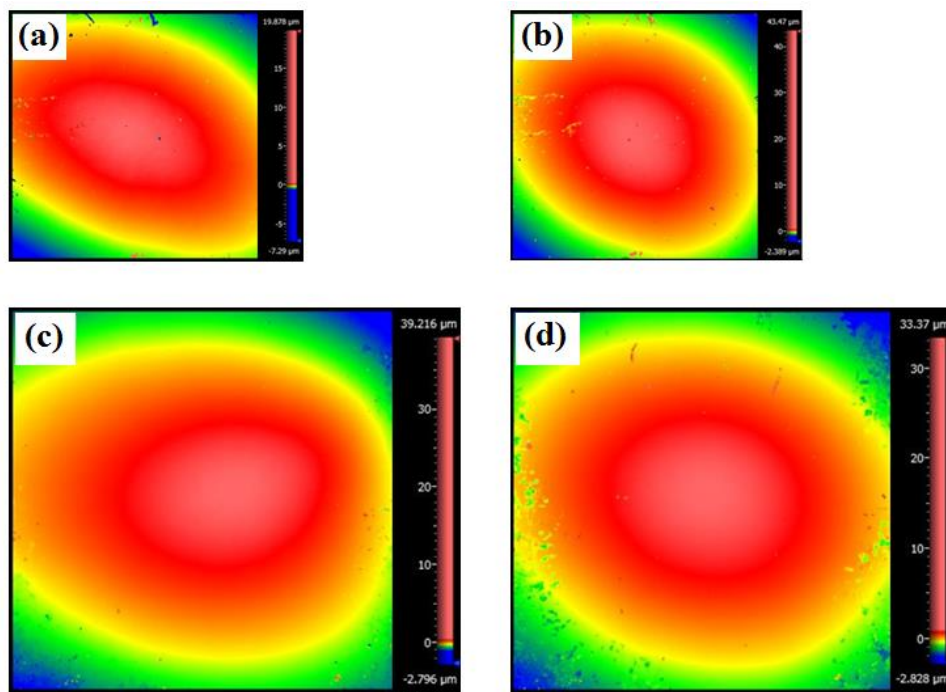
Figure 8.2. Surface profile of the square shape samples (a) 1cm x 1cm square substrate before and (b) after coating, (c) 1.5cm x 1.5cm square substrate before and (d) after coating
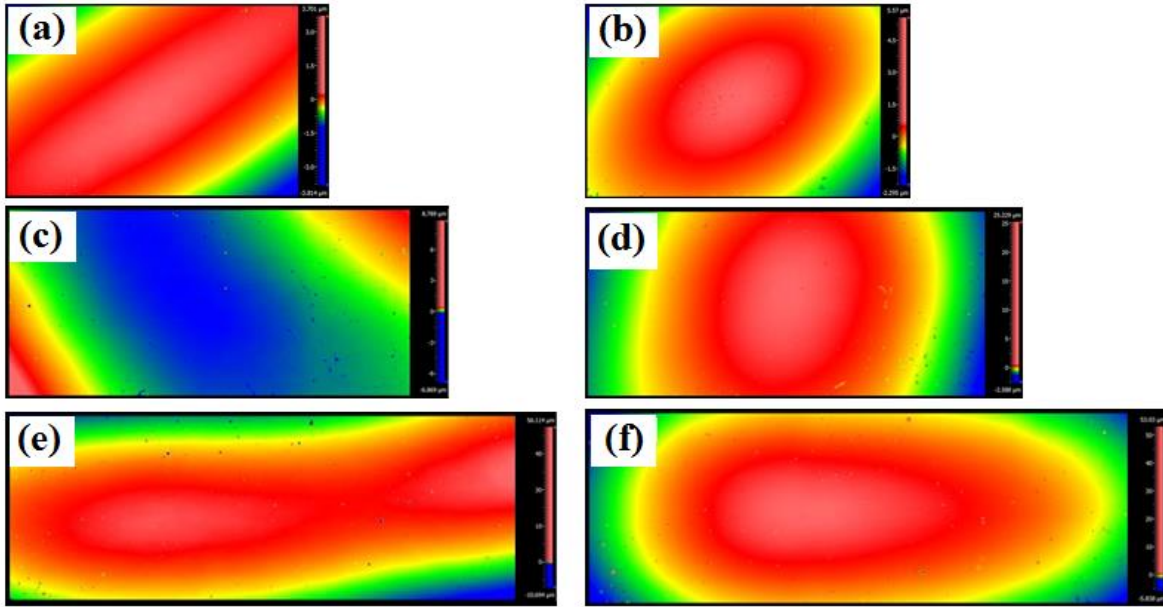
Figure 8.3. Surface profile of the rectangular shape samples (a) 1cm x 1.5cm rectangular substrate before and (b) after coating, (c) 1cm x 2cm rectangular substrate before and (d) after coating, (e) 1cm x 2.5cm rectangular substrate before and (f) after coating

Figure 8.4. Surface profile of the circle shape samples (a) 1cm diameter circle substrate before and (b) after coating, (c) 1.5cm diameter circle before and (d) after coating

Table 8.1. Mean value of curvature radii in X and Y directions of the different shape samples before and after DLC deposition

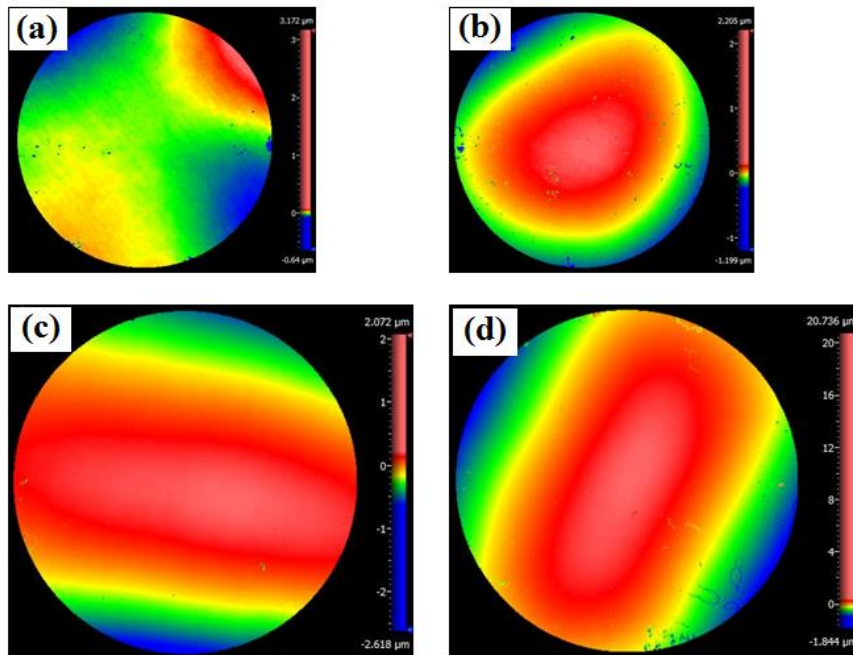| Sample number	Substrate shape	$R_{0X} \pm SD$ (m)	$R_{0Y} \pm SD$ (m)	$R_X \pm SD$ (m)	$R_Y \pm SD$ (m)
1	Small square (1cmx1cm)	46.1±0.3	45.4±0.3	16.3±0.3	16.2±0.3
2	Large square (1.5cmx1.5cm)	45.0±0.3	26.9±0.3	16.0±0.3	12.9±0.3
3	Small rectangular (1cmx1.5cm)	27.3±0.3	38.3±0.3	12.9±0.3	15.1±0.3
4	Medium rectangular (1cmx2cm)	-75.1±0.3	-87.3±0.3	37.2±0.3	33.9±0.3
5	Large rectangular (1cmx2.5cm)	191.9±0.3	3791.1±0.2	21.8±0.3	25.2±0.3
6	Small circle (1cm in diameter)	-1365.0±0.3	1000.4±0.3	25.1±0.3	23.8±0.3
7	Large circle (1.5cm in diameter)	199.8±0.4	700.3±0.2	21.8±0.4	24.0±0.3

Table 8.2 presents the internal stress values of the samples with different shapes and sizes calculated using the Stoney equation, where $E_s = 130$ GPa, $v_s = 0.28$, $h_s = 500 \pm 5$ μm, and $h_f = 0.40 \pm 0.05$ μm (measured value) were used. All the coatings were deposited using similar conditions on the substrate material. It would be reasonable to expect uniform stress in the films for all the samples and all the directions.

The calculated internal stress values along x and y axes for different samples are essentially the same with reasonable errors and follows in the stress range for DLC deposited under similar conditions. These results demonstrate that the deformation of samples after DLC deposition is spherical and this simple method used for DLC stress measurement is reliable and appropriate.

Table 8.2. Internal stress values of samples with different shapes and sizes

Sample number	$\sigma_X \pm$ SD (MPa)	$\sigma_Y \pm$ SD (MPa)
1	766.63±0.02	757.54±0.03
2	757.54±0.02	750.17±0.04
3	750.17±0.04	758.91±0.03
4	759.09±0.01	769.37±0.01
5	756.90±0.01	747.39±0.01
6	766.09±0.01	764.85±0.01
7	760.86±0.01	756.79±0.01

8.4 Conclusions

DLC thin films on Si wafers with different shapes and sizes were synthesized by EHI beam deposition system and the internal stress of the thin films were measured by Zygo optical profiler using the Stoney equation. The measured stress values show that the stress is compressive and essentially the same with reasonable errors for all the samples and all the directions. The results have demonstrated that deformation of samples after DLC deposition is spherical and the simple non-destructive method (Optical profiler) is appropriate and reliable for DLC stress determination, opening a new way to characterize DLC stress simply, non-destructively, and reliably.

CHAPTER 9

CONCLUSIONS AND RECOMMENDATIONS FOR FUTURE WORK

9.1 Conclusions

In this PhD research work, Ta and DLC coatings were synthesized and characterized on CoCrMo alloy sheets to improve the surface functionality of this alloy which has been widely used in biomedical applications. The main findings from experimental investigations are highlighted as follows:

- Ta thin films were deposited on CoCrMo alloy sheets by using RF magnetron sputtering deposition technique. Substrate temperature and bias voltages are determined the most important factors that influence the formation of α- and β-Ta thin films on the CoCrMo alloy sheets. When the deposition temperature is 400 °C or higher, single phase α-Ta thin film forms, whereas a mixture of α- and β-Ta thin film is obtained when the deposition temperature is lower than 400 °C. By applying a substrate bias voltage from 78 V up to 90 V, single phase β-Ta film is obtained at room temperature. Increasing the bias voltage further to 115 V lead to formation of single α-Ta phase.

- The Ta thin films deposited on the CoCrMo alloy sheets consisting of a mixture of α- and β-Ta phases show severe delamination due to the brittleness of β-Ta and the mismatch between its hardness and Young's modulus and those of α-Ta. Adherent single phase β-Ta thin film with a thickness of approximately 0.8 μm was deposited on the CoCrMo alloy sheets at a low negative bias of 78 V. Adherent gradient Ta thin films, β-Ta/β-Ta+α-Ta/α-Ta, with a top layer of α-Ta film was also deposited on CoCrMo alloy sheets with a thickness of approximately 1.1 μm.

- The tribological testing results indicate that the coefficients of friction between the α- and β-Ta coated CoCrMo alloy sheets and UHMWPE balls in phosphate-buffered saline solution are 0.08 ± 0.01 and 0.09 ± 0.01, respectively, and the ball wear rate is determined to be 3.00 ± 0.02 x 10^{-5} mm^{3}N^{-1}m^{-1} and 3.25 ± 0.01 x 10^{-5} mm^{3}N^{-1}m^{-1}, respectively, which are lower than those

$(0.14 \pm 0.01$ and 8.14 ± 0.01 x 10^{-5} mm^{3}N^{-1}m^{-1}) for uncoated CoCrMo alloy sheet sliding with UHMWPE balls. It is probably due to better wettability and lower roughness of the Ta thin films.

- The corrosion testing results indicate that the corrosion current density of the α- and β-Ta coated CoCrMo alloy sheets in phosphate-buffered saline solution are 1.4 x 10^{-8} Acm^{-2} and 9.9 x 10^{-8} Acm^{-2}, respectively, which are significantly lower than that (1.0 x 10^{-5} Acm^{-2}) for uncoated CoCrMo alloy sheet. The superior corrosion resistance of the coatings can be attributed to the formation of a uniform dense Ta$_2$O$_5$ film on the surface, which protected the substrate during the corrosion testing. The α-Ta film shows a higher corrosion resistance due to the formation of a thicker Ta$_2$O$_5$ on the surface.

- fcc Ta thin films with a thickness of approximately 2.0 μm were successfully synthesized using magnetron sputtering at a substrate temperature of 500 °C and 600 °C for the first time. The formation of fcc Ta is dependent on thin film deposition parameters and impurity level. The XRD patterns of the mentioned phase is obtained and reported for the first time, and the lattice parameter is determined to be 4.5065 Å. The crystal structure of the substrate materials has no effect on the formation of fcc Ta, and the fcc Ta keeps its crystal structure up to 700 °C but it transforms to α-Ta after annealing at 750 °C.

- DLC coatings were deposited on CoCrMo alloy sheets using ion beam deposition technique. Two different types of Ta film, α-Ta and β-Ta, were used as an interlayer in order to improve the adhesion of DLC coatings on the alloy. Severe delamination of the DLC coatings was observed on all the samples. The results show that the delamination is not just related to the amount of ion bombardment energy inducing intrinsic stress into the film during DLC deposition, but related to the interfacial bonding between DLC and interlayers. An interface layer is formed at Ta/DLC interface during DLC deposition, this layer is composed of a mixture of Ta carbide and metallic Ta, resulting in weak mechanical bond with DLC film.

- A simple and reliable non-destructive method is introduced for determination of DLC coatings' stress. DLC thin films on Si wafers with different shapes and sizes were synthesized by EHI beam deposition. The internal stress of the thin films were measured with the aid of Zygo optical profiler using the Stoney equation. The measured stress values show that the stress is compressive and essentially the same with reasonable errors for all the samples and all the

directions. The results have demonstrated that deformation of samples after DLC deposition is spherical and this simple method (Optical profiler) is appropriate and reliable for DLC stress determination, thereby opening a new way to characterize DLC coatings' stress.

9.2 Recommendations for future work

Based on the present research, some recommendations for future work are listed below:

- In this research work, Ta thin films were deposited on the CoCrMo alloy sheets. It is suggested to deposit Ta thin films on CoCrMo alloy femoral heads and to investigate their mechanical, tribological, and corrosive properties.

- In this research work, Ta thin films were applied to improve corrosion and wear behavior of the CoCrMo alloy sheets for biomedical implant applications. The tribology testing was done using ball on disk tribometer, in PBS solution, under static load, and in low number of sliding cycles. It is suggested that investigation of the tribological behavior of the samples in a simulated body fluid of osteoarthritis patient, under a range of dynamic load, and in a larger number of sliding cycles be carried out. This suggestion is applicable to corrosion testing condition as well.

- The processing conditions and structural information of fcc Ta are very limited, and the properties of fcc Ta could not be measured so far. In the present research work, the synthesis of fcc Ta thin films and their X-Ray diffraction data is reported for the first time. In this regard, it is very promising to investigate the mechanical and electrical properties of this new phase of Ta. This new finding would open new research and application directions for Ta materials.

- Development of adherent DLC coatings on CoCrMo alloys is very promising for biomedical applications. The present research introduced Ta as an interlayer to improve the adhesion of DLC coatings on the CoCrMo alloy, which was not successful. More investigation is needed to improve the adhesion of DLC coatings on CoCrMo alloys by designing a proper interlayer or changing the composition of the DLC coatings by doping.

LIST OF REFERENCES

[1] Canadian Institute for Health Information, Hip and knee replacements in Canada, 2014-2015, Canadian joint replacement registry annual report, Ottawa, 2017.

[2] H.A. Ching, D. Choudhury, M.J. Nine, N.A. Abu Osman, Effects of surface coating on reducing friction and wear of orthopedic implants: a review, Sci. Technol. Adv. Mater. 15 (2014) 1-21.

[3] http://www.stvincentsboneandjoint.com.au/total-hip-replacement.html

[4] M.J. Nine, D. Choudhury, A.C. Hee, R. Mootanah, N.A. Abu Osman, Wear debris characterization and corresponding biological response: artificial hip and knee joints: a review, Materials (Basel) 7 (2014) 980-1016.

[5] Y.S. Al Jabbari, Physico-mechanical properties and prosthodontic applications of Co-Cr dental alloys: a review of the literature, J. Adv. Prosthodont. 6 (2014) 138-145.

[6] Y. Liao, E. Hoffman, M. Wimmer, A. Fischer, J. Jacobs, L. Marks, CoCrMo Metal-on-Metal Hip Replacements, Phys. Chem. Chem. Phys. 15(3) (2013) 746-756.

[7] S. Kurtz, K. Ong, E. Lau, F. Mowat, M. Halpern, Projections of Primary and revision hip and knee arthroplasty in the United States from 2005 to 2030, J. Bone. Joint. Surg. 89(4) (2007) 780-785.

[8] S. Kurtz, UHMWPE Biomaterials Handbook: Ultra High Molecular Weight Polyethylene in Total Joint Replacement, Elsevier, Amsterdam, 2004.

[9] R.I.M. Asri, W.S.W. Harun, M. Samykano, N.A.C. Lah, S.A.C. Ghani, F. Tarlochan, M.R. Raza, Corrosion and surface modification on biocompatible metals: A review, Mater. Sci. Eng. C 77 (2017) 1261-1274.

[10] M. Tarabolsi, T. Klassen, F. Mantwill, F. Gartner, F. Siegel, A.P. Schulz, Patterned CoCrMo and Al_2O_3 surfaces for reduced free wear debris in artificial joint arthroplasty, J. Biomed. Mater. Res. A 101A (2013) 3447-3456.

[11] H. Ito, K. Kaneda, T. Yuhta, I. Nishimura, K. Yasuda, T. Matsuno, Reduction of polyethylene wear by concave dimples on the frictional surface in artificial hip joints, J. Arthroplasty 15(3) (2000) 332-338.

[12] A. Ekeberg, Of the Properties of the Earth Yttria, compared with those of Glucine; of Fossils, in which the first of these Earths in contained; and of the Discovery of a metallic Nature (Tantalium), J. Nat. Philos. Chem. Art. 3 (1802) 251-255.

[13] L. Hallmann, P. Ulmer, Effect of sputtering parameters and substrate composition on the structure of tantalum thin films, Appl. Surf. Sci. 282 (2013) 1-6.

[14] D.W. Matson, E.D. McClanahan, S.L. Lee, D. Windover, Properties of thick sputtered Ta used for protective gun tube coatings, Surf. Coat. Technol. 146-147 (2001) 344-350.

[15] C.C. Huang, Y.L. Wang, S.C. Chang, G.J. Hwang, J.L. Huang, Phase transformation of tantalum on different dielectric films with plasma treatment, Thin Solid Films 498 (2006) 286-288.

[16] M.H. Read, C. Altman, A new structure in tantalum thin films, Appl. Phys. Lett. 7 (1965) 51-52.

[17] S.L. Lee, M. Doxbeck, J. Mueller, M. Cipollo, P. Cote, Texture, structure and phase transformation in sputter beta tantalum coating, Surf. Coat. Technol. 177-178 (2004) 44-51.

[18] W.D. Westwood, N. Waterhouse, P.S. Wilcox, Tantalum thin films, Academic press, London, New York, 1975.

[19] A. Javed, J.B. Sun, An investigation of structural phase transformation and electrical resistivity in Ta films, Appl. Surf. Sci. 257 (2010) 1211-1215.

[20] M. Zhang, Y.F. Zhang, P.D. Rack, M.K. Miller, T.G. Nieh, Nanocrystalline tetragonal tantalum thin films, Scripta Materialia 57 (2007) 1032-1035.

[21] M. Grosser, U. Schmid, The impact of sputter conditions on the microstructure and on the resistivity of tantalum thin films, Thin Solid Films 517 (2009) 4493-4496.

[22] A.A. Navid, A.M. Hodge, Nanostructured alpha and beta tantalum formation-relationship between plasma parameters and microstructure, Mater. Sci. Eng. A 536 (2012) 49-56.

[23] S. Myers, J. Lin, R. Martins Souza, W.D. Sproul, J.J. Moore, The β to α phase transition of tantalum coatings deposited by modulated pulsed power magnetron sputtering, Surf. Coat. Technol. 214 (2013) 38-45.

[24] Y. M. Wang, A. M. Hodge, P. M. Bythrow, T. W. Barbee, and A. V. Hamza, Negative strain rate sensitivity in ultrahigh-strength nanocrystalline tantalum, Appl. Phys. Lett. 89 (2006) 081903-1-081903-3.

[25] D. Bernoulli, U. Muller, M. Schwarzenberger, R. Hauert, R. Spolenak, Magnetron sputter deposited tantalum and tantalum nitride thin films: an analysis of phase, hardness and composition, Thin Solid Films 548 (2013) 157-161.

[26] L. Gladczuk, A. Patel, C. Paur, M. Sosnowski, Tantalum films for protective coatings of steel, Thin Solid Films 467 (2004) 150-157.

[27] P. N. Denbigh, R. B. Marcus, Structure of very thin tantalum and molybdenum films, J. Appl. Phys. 37 (1966) 4325-4330.

[28] K.L. Chopra, M.R. Randle, R.H. Duff, Face-centered cubic modification in sputtered films of tantalum, molybdenum, tungsten, rhenium, hafnium and zirconium, Philos. Mag. 16 (1967) 261-273.

[29] R.B. Marcus, S. Quigley, Formation of f.c.c., b.c.c. and β-tantalum films by evaporation,

Thin Solid Films 2 (1968) 467-477.

[30] F. Schrey, R.D. Mathis, R.T. Payne, L.E. Murr, Structure and properties of r.f. sputtered superconducting tantalum films, Thin Solid Films 5 (1970) 29-40.

[31] M.T. Janish, W.M. Mookb, C.B.Cartera, Nucleation of fcc Ta when heating thin films, Scr.

Mater. 96 (2015) 21-24.

[32] M.T. Janish, P.G. Kotula, B.L. Boyce, C. Barry Carter, Observations of fcc and hcp tantalum, J. Mater. Sci. 50 (2015) 3706-3715.

[33] C. Balagna, M.G. Faga, S. Spriano, Tantalum-based multilayer coating on cobalt alloys in total hip and knee replacement Mater. Sci. Eng. C 32 (2012) 887-895.

[34] V.K. Balla, S. Banerjee, S. Bose, A. Bandyopadhyay, Direct laser processing of a tantalum coating on titanium for bone replacement structures, Acta Biomater. 6 (2010) 2329-2334.

[35] S. Dittrick, V.K. Balla, S. Bose, A. Bandyopadhyay, Wear performance of laser processed tantalum coatings, Mater. Sci. Eng. C 31 (2011) 1832-1835.

[36] S.L. Lee, M. Cipollo, D. Windover and C. Rickard, Analysis of magnetron sputtered tantalum coatings versus electrochemically deposited tantalum from molted salt, Surf. Coat. Technol. 120-121 (1999) 44-52.

[37] F. Brossa, M. Bardy and G. Piatti, Tantalum protective coatings for fusion reactor application, J. Nucl. Mat. 103-104 (1981) 261-266.

[38] Y.K. Lee, K. Maung Latt, K. Jaetlyung and L. Lee, Study of diffusion barrier properties of ionized metal plasma (IMP) deposited tantalum (Ta) between Cu and SiO_2, Mater. Sci. Eng. B6 8 (1999) 99-103.

[39] D.M. Mattox, Handbook of physical vapor deposition (PVD) processing: film formation, adhesion, surface preparation and contamination control, Westwood, New Jersey, 1998.

[40] C. P. Mulligan, Origins of beta tantalum in sputtered coatings, US army armament research, development and engineering center, close combat armaments center benet laboratories, Watervliet, New York, 2001.

[41] R. A. Roy, P. Catania, K. L. Saenger, J. J. Cuomo, and R. L. Lossy, Role of energetic atoms and ions in Ta films grown by different physical vapor deposition methods, J. Vac. Sci. Technol. B 11(5) (1993) 1921-1927.

[42] J. Alami, P. Eklund, J.M. Andersson, M. Lattemann, E. Wallin, J. Bohlmark, P. Persson, U. Helmersson, Phase tailoring of Ta thin films by highly ionized pulsed magnetron sputtering, Thin Solid Films 515 (2007) 3434-3438.

[43] P. Catania, R.A. Roy, J.J. Cuomo, Phase formation and microstructure changes in tantalum thin films induced by bias sputtering, J. Appl. Phys. 74(2) (1993) 1008-1014.

[44] L.A. Clevenger, A. Mutscheller, J.M.E. Harper, C. Cabral, K. Barmak, The relationship between deposition conditions, the beta to alpha phase transformation, and stress relaxation in tantalum thin films, J. Appl. Phys. 72 (1992) 4918-4924.

[45] M. Nakumura, M. Fujimori, Y. Nishimura, Phase forming processes in tantalum films through sputtering, Jpn. J. Appl. Phys. 9(5) (1970) 557-571.

[46] G. Das, A new structure of sputtered tantalum, Thin Solid Films 12(2) (1972) 305-311.

[47] D. Gerstenberg, C. J. Calbick, Effects of nitrogen, and oxygen on structure and electrical properties of thin tantalum films, J. Appl. Phys. 35(2) (1964) 402-407.

[48] E. Krikorian, R. J. Sneed, Deposition of tantalum, tantalum oxide, and tantalum nitride with controlled electrical characteristics, J. Appl. Phys. 37(10) (1966) 3674-3681.

[49] P.N. Baker, RF sputtered tantalum films deposited in an oxygen doped atmosphere, Thin Solid Films 6(5) (1970) R57-R60.

[50] W.D. Westwood, F.C. Livermore, Phase composition and conductivity of sputtered tantalum, Thin Solid Films 5(5-6) (1970) 407-420.

[51] N. Schwartz, E.D. Feit, Impurity Effects in the Nucleation of Alpha (bcc)-Tantalum or Beta-Tantalum Films, ECS J. Solid State Sci. Technol. 124(1) (1977) 123-131.

[52] N.N. Axelrod, R.B. Marcus, In situ reflection high energy electron diffraction study of the nucleation and growth of tantalum films, Thin Solid Films 15 (1973) 21-23

[53] J. Sosniak, W.J. Polito, G.A. Rozgonyi, Effect of Background-Gas Impurities on the Formation of Sputtered β-Tantalum Films, J. Appl. Phys. 38 (1967) 3041-3044.

[54] L.G. Feinstein, R.D. Huttemann, Factors controlling the structure of sputtered Ta films, Thin Solid Films 16(2) (1973) 129-145.

[55] A. Schauer, W. Peters, W. Juergens, A very pure thin film tantalum phase, Thin Solid Films 8(3) (1971) R9-R12.

[56] A. Schauer, W. Peters, The influence of film thickness on the formation of β-Ta and b.c.c.-Ta, Thin Solid Films 27(1) (1975) 95-99.

[57] N. Arshi, J. Lu, C.G. Lee, B.H. Koo, F. Ahmed, Effect of substrate temperature on the properties of electron beam deposited tantalum films, Thin Solid Films 546 (2013) 22–25.

[58] D. Fischer, O. Meissner, B. Bendjus, J. Schreiber, M. Stavrev, C. Wenzel, AFM Characterization of Ta-based Diffusion Barriers for Use in Future Semiconductor Metallization, Surf. Interface Anal. 25 (1997) 522-528.

[59] Y.M. Zhou, Z. Xie, H.N. Xiao, P.F. Hu, J. He, Effects of deposition parameters on tantalum films deposited by direct current magnetron sputtering, J. Vac. Sci. Technol. A 27 (2009) 109-113.

[60] D.W. Face, D.E. Prober, Nucleation of body-centered-cubic tantalum films with a thin niobium underlayer, J. Vac. Sci. Technol. A 5 (1987) 3408-3411.

[61] S. Morohashi, K. Gotoh, S. Komiya, Fabrication of Josephson junctions using an Al/Ta/Nb structure for x-ray detection, Appl. Phys. Lett. 64 (1994) 785-787.

[62] S.L. Lee, D. Windover, Phase, residual stress, and texture in triode-sputtered tantalum coatings on steel, Surf. Coat. Technol. 108-109 (1998) 65-72.

[63] R. Hoogeveen, M. Moske, H. Geisler, K. Samwer, Texture and phase transformation of sputter-deposited metastable Ta films and Ta/Cu multilayers, Thin Solid Films 275 (1996) 203-206.

[64] G.S. Chen, S.T. Chen, S.C. Huang, H.Y. Lee, Growth mechanism of sputter deposited Ta and Ta-N thin films induced by an underlying titanium layer and varying nitrogen flow rates, Appl. Surf. Sci. 169-170 (2001) 353-357.

[65] S. Spriano, E. Verne, M.G. Faga, S. Bugliosi, G. Maina, Surface treatment on an implant cobalt alloy for high biocompatibility and wear resistance, Wear 259 (2005) 919-925.

[66] C. Balagna, S. Spriano, M.G. Faga, Characterization of Co-Cr-Mo alloys after a thermal treatment for high wear resistance, Mater. Sci. Eng. C 32 (2012) 1868-1877.

[67] C. Balagna, M.G. Faga, S. Spriano, Tribological behavior of a Ta-based coating on a Co-Cr-Mo alloy, Surf. Coat. Technol. 258 (2014) 1159-1170.

[68] U. Dorn, D. Neumann, M. Frank, Corrosion behavior of tantalum-coated cobalt-chromium modular necks compared to titanium modular necks in a simulator test, J. Arthroplast. 29 (2014) 831-835.

[69] C.A. Love, R.B. Cook, T.J. Harvey, P.A. Dearnley, R.J.K. Wood, Diamond like carbon coatings for potential application in biological implants: a review, Tribol. Int. 63 (2013) 141–150.

[70] J. Robertson, Diamond-like amorphous carbon, Mater. Sci. Eng. R 37 (2002) 129-281.

[71] V. Saikko, T. Ahlroos, O. Calonius, J. KeraKnen, Wear simulation of total hip prostheses with polyethylene against CoCr, alumina and diamond-like carbon, Biomaterials 22 (2001) 1507-1514.

[72] D. Sheeja, B.K. Tay, S.P. Lau, L.N. Nung, Tribological characterisation of diamond-like carbon coatings on Co-Cr-Mo alloy for orthopaedic applications, Surf. Coat. Technol. 146-147 (2001) 410-416.

[73] S.J. Huang, W.S. Ju, S.R. Lyu, A Wear Study of Diamond-like Carbon Film for Total Hip Arthroplasty Applications, J. Med. Biol. Eng. 26(4) (2006) 169-175.

[74] H. Koseki, H. Shindo, K. Baba, T. Fujikawa, N. Sakai, Y. Sawae, T. Murakami, Surface-engineered metal-on-metal bearings improve the friction and wear properties of local area contact in total joint arthroplasty, Surf. Coat. Technol. 202 (2008) 4775-4779.

[75] H. Holeczek, C.B. Santos, L. Haubold, M. Metzner, DLC-coated CoCrMo steel for use in medical implants-wear and corrosion resistance influence of different surface finishing techniques, O. Dössel, W.C. Schlegel (eds) World Congress on Medical Physics and Biomedical Engineering, Munich, Germany, Springer, Berlin, Heidelberg, 2009.

[76] C.B. Santos, L. Haubold, H. Holeczek, M. Becker, M. Metzner, Wear-corrosion resistance of DLC/CoCrMo system for medical implants with different surface finishing, Tribol. Lett. 37(2) (2010) 251-259.

[77] U. Muller, C.V. Falub, G. Thorwarth, C. Voisard, R. Hauert, Diamond-like carbon coatings on a CoCrMo implant alloy: A detailed XPS analysis of the chemical states at the interface, Acta Materialia 59 (2011) 1150-1161.

[78] C.V. Falub, U. Muller, G. Thorwarth, M. Parlinska-Wojtan, C. Voisard, R. Hauert, In vitro studies of the adhesion of diamond-like carbon thin films on CoCrMo biomedical implant alloy, Acta Materialia 59 (2011) 4678-4689.

[79] C.V. Falub, G. Thorwarth, C. Affolter, U. Muller, C. Voisard, R. Hauert, A quantitative in vitro method to predict the adhesion lifetime of diamond-like carbon thin films on biomedical implants, Acta Biomaterialia 5 (2009) 3086-3097.

[80] H. Liu, Y. Leng, J. Tang, S. Wang, D. Xie, H. Sun, N. Huang, Tribological performance of ultra-high-molecular-weight polyethylene sliding against DLC-coated and nitrogen ion implanted CoCrMo alloy measured in a hip joint simulator, Surf. Coat. Technol. 206 (2012) 4907-4914.

[81] J. Liu, X. Wang, B.J. Wu, T.F. Zhang, Y.X. Leng, N. Huang, Tribocorrosion behavior of DLC-coated CoCrMo alloy in simulated biological environment, Vacuum 92 (2013) 39-43.

[82] F. Guo, Z. Zhou, M. Hua, G. Dong, Effect of aqueous solution and load on the formation of DLC transfer layer against Co-Cr-Mo for joint prosthesis, J. Mech. Behav. Biomed. Mater. 49 (2015) 12-22.

[83] R. Hauert, G. Thorwarth, U. Muller, M. Stiefel, C.V. Falub, K. Thorwarth, T.J. Joyce, Analysis of the in-vivo failure of the adhesive interlayer for a DLC coated articulating metatarsophalangeal joint, Diam. Relat. Mater. 25 (2012) 34-39.

[84] R. Hauert, C.V. Falub, G. Thorwarth, K. Thorwarth, Ch. Affolter, M. Stiefel, L.E. Podleska, G. Taeger, Retrospective lifetime estimation of failed and explanted diamond-like carbon coated hip joint balls, Acta Biomater. 8 (2012) 3170-3176.

[85] K. Thorwarth, G. Thorwarth, R. Figi, B. Weisse, M. Stiefel, R. Hauert, On interlayer stability and high-cycle simulator performance of diamond-like carbon layers for articulating joint replacements, Int. J. Mol. Sci. 15 (2014) 10527-10540.

[86] http://www.plasmionique.com/products/pvd-deposition-system/sputter-deposition-systems/

[87] https://angstromengineering.com/tech/magnetron-sputtering/

[88] http://www.mtixtl.com/1500CCompactTubeFurnace-GSL-1500X-50-UL.aspx/

[89] https://www.zygo.com/?/met/profilers/

[90] https://www.testingmachines.com/product/68-76-pocketgoniometer-pgx

[91] ME 843.3, Materials characterization techniques course (CRN 24527), University of Saskatchewan, Saskatchewan, 2015.

[92] N. Vidakis, A. Antoniadis, N. Bilalis, The VDI 3198 indentation test evaluation of a reliable qualitative control for layered compounds, J. Mater. Process. Technol. 143-144 (2003) 481-485.

[93] ISO 14577-4, Metallic materials-Instrumented indentation test for hardness and materials parameters-Part 4: Test method for metallic and non-metallic coatings, 2016.

[94] ISO 14242-1, Implants for surgery-Wear of total hip-joint prostheses-Part 1: Loading and displacement parameters for wear-testing machines and corresponding environmental conditions for test, 2014.

[95] ASTM G99-17, Standard test method for wear testing with a pin-on-disk apparatus, 2017.

[96] https://www.gamry.com/cells-and-accessories/electrochemical-cells/

[97] ASTM G61-86, Standard test method for conducting cyclic potentiodynamic polarization measurements for localized corrosion susceptibility of Iron-, Nickel-, or Cobalt-Based alloys, 2018.

[98] A. Jiang, T.A. Tyson, L. Axe, The stability of the β-phase of tantalum: a molecular dynamics study, J. Phys. Condens. Matter. 17 (2005) 1841-1850.

[99] Z. Chen, W. Tian, X. Zhang, Y. Wang, Effect of deposition parameters on surface roughness and consequent electromagnetic performance of capacitive RF MEMS switches: a review, J. Micromech. Microeng. 27 (2017) 1-26.

[100] M. Roy, V.K. Balla, S. Bose, A. Bandyopadhyay, Comparison of tantalum and hydroxyapatite coatings on titanium for applications in load bearing implants, Adv. Eng. Mater. 12 (2010) B637- B641.

[101] F. Meng, Z. Li, X. Liu, Synthesis of tantalum thin films on titanium by plasma immersion ion implantation and deposition, Surf. Coat. Technol. 229 (2013) 205-209.

[102] A.A. Khalili, M.R. Ahmad, A Review of cell adhesion studies for biomedical and biological applications, Int. J. Mol. Sci. 16 (2015) 18149-18184.

[103] K. Kato, Wear in relation to friction-a review, Wear 241 (2000) 151-157.

[104] W. Jin, G. Wang, Z. Lina, H. Feng, W. Li, X. Peng, A.M. Qasim, P.K. Chu, Corrosion resistance and cytocompatibility of tantalum-surface-functionalized biomedical ZK60 Mg alloy, Corros. Sci. 114 (2017) 45-56.

[105] A.C. Hee, Y. Zhao, S.S. Jamali, P.J. Martin, A. Bendavid, H. Peng, X. Cheng, Corrosion behaviour and microstructure of tantalum film on Ti_6Al_4V substrate by filtered cathodic vacuum arc deposition, Thin Solid Films 636 (2017) 54-62.

[106] A.C. Hee, S.S. Jamali, A. Bendavid, P. J. Martin, C. Kong, Y. Zhao, Corrosion behaiour and adhesion properties of sputtered tantalum coating on Ti_6Al_4V substrate, Surf. Coat. Technol. 307 (2016) 666-675.

[107] W. Hu, J. Xu, X. Lu, D. Hu, H. Tao, P. Munroe, Z.H. Xie, Corrosion and wear behaviours of a reactive-sputter-deposited Ta_2O_5 nanoceramic coating, Appl. Surf. Sci. 368 (2016) 177-190.

[108] Y. Zhou, M. Li, Y. Cheng, Y.F. Zheng, T.F. Xi, S.C. Wei, Tantalum coated NiTi alloy by PIIID for biomedical application, Surf. Coat. Technol. 228 (2013) S2-S6.

[109] P.N. Baker, Preparation and properties of tantalum thin films: a review, Thin Solid Films 14 (1972) 3-25.

[110] C. Suryanarayana, M. Grant Norton, X-Ray Diffraction: A Practical Approach, Plenum Press, New York, 1998.

[111] B. Fultz, J. Howe, Transmission Electron Microscopy and Diffractometry of Materials, Springer-Verlag, Berlin, 2013.

[112] R. Simpson, R.G. White, J.F. Wattsa, M.A. Baker, XPS investigation of monatomic and cluster argon ion sputtering of tantalum pentoxide, Appl. Surf. Sci. 405 (2017) 79-87.

[113] T. Tsuchiya, H. Imai, S. Miyoshi, P. A. Glans, J. Guo, S. Yamaguchi, X-Ray absorption, photoemission spectroscopy, and raman scattering analysis of amorphous tantalum oxide with a large extent of oxygen nonstoichiometry, Phys. Chem. Chem. Phys. 13 (2011) 17013-17018.

[114] C. He, J. Tao, Two-dimensional TaC nanosheets on a reduced graphene oxide hybrid as an efficient and stable electrocatalyst for water splitting, Chem. Commun. 52 (2016) 8810-8813.

[115] J. Robertson, Diamond-like amorphous carbon, Mater. Sci. Eng. 37 (2002) 129-281.

[116] https://xpssimplified.com/elements/tantalum.php

[117] W. Rong, H. Hei, Q. Zhong, Y. Shen, X. Liu, X. Wang, B. Zhou, Z. He, S. Yu, Nanostructured TaxC interlayer synthesized via double glow plasma surface alloying process for diamond deposition on cemented carbide, Appl. Surf. Sci. 359 (2015) 41-47.

[118] L.I. Johansson, Electronic and structural properties of transition-metal carbide and nitride surfaces, Surf. Sci. Rep. 21 (1995) 177-250.

[119] https://xpssimplified.com/elements/carbon.php

[120] C. Donnet, A. Erdemir, Tribology of diamond-like carbon films: fundamentals and applications, Springer Science, New York, 2008.

[121] S.G. Malhotra, Z.U. Rek, S.M. Yalisove, J.C. Bilello, Analysis of thin film stress measurement techniques, Thin Solid Films 301 (1997) 45-54.

[122] G.G. Stoney, The tensions of metallic films deposited by electrolysis, Proc. R. Soc. Land. A82 (1909) 172-175.

[123] L.B. Freund, S. Suresh, Thin film materials: Stress, defect formation and surface evolution, Cambridge University Press, United Kingdom, 2003.

[124] M. Ahmed, A. Besnard, M.R. Ardigo, Stoney formula: investigation of curvature measurements by optical profilometer, Adv. Mater. Res. 996 (2014) 361-366.

[125] J.M. Pureza, M.M. Lacerda, A.L. De Oliveira, J.F. Fragalli, R.A.S. Zanon, Enhancing accuracy to Stoney equation, Appl. Surf. Sci. 255 (2009) 6426-6428.

[126] N. Guyot, Y. Harmand, A. Mezin, The role of the sample shape and size on the internal stress induced curvature of thin-film substrate systems, Int. J. Solids Struct. 41 (2004) 5143-5154.

[127] A. Mezin, Coating internal stress measurement through the curvature method: a geometry-based criterion delimiting the relevance of Stoney's formula, Surf. Coat. Technol. 200 (2006) 5259-5267.

[128] D. Ngo, X. Feng, Y. Huang, A.J. Rosakis, M.A. Brown, Thin film/substrate systems featuring arbitrary film thickness and misfit strain distributions. Part I: analysis for obtaining film stress from non-local curvature information, Int. J. Solids Struct. 44 (2007) 1745-1754.

[129] X. Feng, Y. Huang, A.J. Rosakis, On the Stoney formula for a thin film/substrate system with nonuniform substrate thickness, J. Appl. Mech. 74 (6) (2007) 1276-1281.

[130] N. Schwarzer, F. Richter, G. Hecht, Determination of mechanical properties of thin films: a theoretical feasibility study, Surf. Coat. Technol. 60 (1-3) (1993) 396-400.

APPENDIX

COPYRIGHT PERMISSION

Chapter 4 and 8 are published in two Elsevier journals. Chapter 6 is under review in an Elsevier journal. For articles published by Elsevier, the authors retain the right to include their article in a thesis or dissertation without the need to obtain a written permission:

- The permission for including the paper "Growth and characterization of tantalum multilayer thin films on CoCrMo alloy for orthopedic implant applications" in the Chapter 4.

- The permission for including the paper "Evaluation of Stoney equation for determining the internal stress of DLC thin films using an optical profiler" in the Chapter 8.

Copyright Clearance Center

RightsLink®

Home | Account Info | Help

Title:	Evaluation of Stoney equation for determining the internal stress of DLC thin films using an optical profiler
Author:	Sheida Shiri,Parisa Ashtijoo,Akindele Odeshi,Qiaoqin Yang
Publication:	Surface and Coatings Technology
Publisher:	Elsevier
Date:	25 December 2016

© 2016 Elsevier B.V. All rights reserved.

Logged in as:
Sheida Shiri
Account #:
3001289697

LOGOUT

BACK | CLOSE WINDOW